Materials Sciences Corporation

NDE OF CERAMIC MATRIX COMPOSITES FOR RADOMES

PART 1. PROGRAM DESCRIPTION AND ANALYTICAL STUDIES

Technical Final Report
MSC TFR 3710/AB39
July, 1997

Contract No. N00167-95-C-0033
CDRL A003
For the Period: December 31, 1994 to June 30, 1997

Prepared For:

Dr. John M. Liu, Code 684
Naval Surface Warfare Center
Carderock Division
9500 MacArthur Blvd.
West Bethesda, MD 20817-5700

Suite 250, 500 Office Center Drive
Fort Washington, PA 19034
Tel: 215-542-8400 Fax: 215-542-8401

25 Years Advanced Composites Technology

REPORT DOCUMENTATION PAGE	Form Approved OMB No. 0704-0188

1. AGENCY USE ONLY (*Leave blank*)	2. REPORT DATE	3. REPORT TYPE AND DATES COVERED
	July, 1997	Final Report - 12/94 - 6/97

4. TITLE AND SUBTITLE

NDE of Ceramic Matrix Composites for Radomes
Part 1. Program Description and Analytical Studies

5. FUNDING NUMBERS

N00167-95-C-0033

6. AUTHORS(S)

Sailendra N. Chatterjee, Chian-Fong Yen, Dominic Mirto

7. PERFORMING ORGANIZATION NAME(S) AND ADDRESS(ES)

Materials Sciences Corporation
500 Office Center Drive, Suite 250
Fort Washington, PA 19034

8. PERFORMING ORGANIZATION REPORT NUMBER

MSC TFR 3710/AB39

9. SPONSORING/MONITORING AGENCY NAME(S) AND ADDRESS(ES)

Dr. John M. Liu, Code 684
Naval Surface Warfare Center, Carderock Division
9500 MacArthur Blvd.
West Bethesda, MD 20817-5700

10. SPONSORING/MONITORING AGENCY REPORT NUMBER

11. SUPPLEMENTARY NOTES

12a. DISTRIBUTION/AVAILABILITY STATEMENT

Distribution Statement A; Approved for Public Release. Distribution is unlimited

12B. DISTRIBUTION CODE

13. ABSTRACT (*Maximum 200 words*)

Variations in porosity and/or reinforcement content were found to be the major anomalies, which influence the dielectric property as well as stiffness and strength of ceramic matrix composites being considered for next generation radomes as well as other applications. Analyses and experiments conducted showed that such variations can be quantified using ultrasonic as well as microwave NDE. The latter method yields a measure of the changes in the dielectric constant, whereas the first measures the changes in the sound wave velocity (or attenuation) due to the porosity variations. Simple results for two-phase composites as well as those based on experimental data for the material tested were suggested for relating velocity change to porosity and for obtaining analytical estimates of dielectric property variations. The Radome Analysis Computer Program (RACP™) was modified to estimate the changes in boresight errors and monopulse antenna receiving patterns for radomes with porous regions with reduced dielectric constant. The inspection system and suggested assessment methods should be useful for practical applications.

14. SUBJECT TERMS	15. NUMBER OF PAGES
Ceramic Composites, Radomes, Anomalies, Nondestructive Evaluation, Inspection System, Ultrasonic Characterization, Microwave Probes, Boresight Error, Acceptance Criteria	156
	16. PRICE CODE

17. SECURITY CLASSIFICATION OF REPORT	18. SECURITY CLASSIFICATION OF THIS PAGE	19. SECURITY CLASSIFICATION OF ABSTRACT	20. LIMITATION OF ABSTRACT
UNCLASSIFIED	UNCLASSIFIED	UNCLASSIFIED	

NSN 7540-01-280-5500

Standard From 298 (rev. 2-89)
Prescribed by ANSI Std. Z39-18
298-102

PREFACE

This report describes the work performed under Naval Surface Warfare Center (NSWC) Contract No. N00167-95-C-0033, "NDE of Ceramic Matrix Composites for Radomes", SBIR Phase II. Analytical studies reported in Part 1 were performed by Materials Sciences Corporation (MSC) staff; Dr. Sailendra N. Chatterjee (principal investigator), Dr. Chian-Fong Yen and Mr. Dominic Mirto. Experimental studies reported in Part 2 were performed under the supervision of Professor John C. Duke, Jr., Department of Engineering Science and Mechanics, Virginia Polytechnic Institute and State University (VPI&SU). Dr. John M. Liu was the technical coordinator at NSWC.

TABLE OF CONTENTS

PAGE

PART 1. PROGRAM DESCRIPTION AND ANALYTICAL STUDIES

PART 2. EXPERIMENTAL STUDIES

INTRODUCTION

The goal of this effort was to choose one or more nondestructive techniques, which are simple and yet can provide quick evaluation of next generation radomes for quality verification during process development or for product acceptance purposes. Reasonable quantitative predictions of physical property variations over the entire part should also be possible from test data or generated images. It may be noted that currently used inspection techniques using transmitted light are not suitable for reinforced ceramics which do not allow such transmission. Phase I studies, summarized in the next section, indicate that optical, infrared, dielectric or ultrasonic (thru-transmission) imaging can be useful for determining changes in void or reinforcement content commonly encountered in reinforced ceramics. Large variations of void and/or inclusion content appear to be the dominant type of anomaly in unreinforced as well as reinforced ceramics and can significantly influence the electromagnetic performance of radomes. X-ray radiography may be useful for identifying other kinds of defects.

Studies were conducted in this phase to test the usefulness of various inspection techniques for particle reinforced ceramics being considered for next generation radomes. Works performed include development of measurement techniques, procedures, scanning devices and softwares for nondestructive imaging of dome shaped radomes using ultrasound and/or microwaves. Such inspections can be employed at critical steps of manufacturing for quality assurance and particularly prior to system assembly and performance testing as specified by the Navy CDRL and other acceptance documents. Various analyses were also performed to evaluate the performance of electromagnetic sensors used for nondestructive imaging and to estimate the effects of patch defects on radome performance.

BACKGROUND

Radome materials proposed for future generations of tactical missiles will require stability at high temperatures (to 1400°C), low dielectric constants and low loss tangents. Also, they will need dimensional stability (low-thermal expansion coefficients), moderately good strength and toughness (to withstand handling, aerodynamic and thermal stresses) as well as thermal shock and erosion resistance (Ref. 1, 2). Moisture absorption should be minimal. Finally the density should be as low as possible to reduce weight and increase payloads. Continuous fiber (in laminated or woven forms) as well as particle or whisker reinforced ceramics (Ref. 3, 4) are being considered for such applications, since these composites can be tailored to provide desired dielectric and thermo-mechanical properties. Since fabrication processes for ceramic matrix composites are new and complicated, it is possible that distribution of reinforcements and other microstructural details in a fabricated part or product may not be the same as desired. In addition, such components may also contain flaws like surface cracks, voids, breaks in continuous fibers, reinforcement/matrix separations, etc. Nondestructive evaluations are useful for locating and quantifying these features as well as their effects on performance and the expected life of a product. They can also serve a role in the development of improved processes and fabrication techniques.

Phase I studies were aimed at classifying possible types of flaws and anomalies in whisker reinforced ceramics being considered for radome applications, obtaining some analytical or semi-empirical estimates of the effects as well as critical sizes and locations of such defects and developing some nondestructive testing techniques which may be employed for their characterization. Although it is advantageous to determine as many properties (or anomalies) as possible using the same technique, it is known from NDE studies on ceramics (Ref. 5-7) that sometimes multiple techniques may be needed to quantify certain types of anomalies. Various NDT methods were employed for examination of whisker reinforced ceramic samples. A brief description of the results of Phase I studies (Ref. 8) follows.

Void content and changes in amount of whiskers were found to be the most important anomalies in whisker reinforced ceramics. Crack like flaws can also occur in such materials. Following remarks can be made about their influence on material properties and characterization by NDE.

1. Analytical results indicate that 26% porosity can cause about 42% reduction in Young's and shear moduli of whisker reinforced ceramics (Figure 1). Such reductions are possibly acceptable. Also, 11% porosity can cause greater than 17% reduction in modulus, which should be detectable by ultrasonics with reasonable accuracy. In addition, analytical results also indicate that a 10% increase in fiber content causes 8% increase in moduli, which should be detectable. However, change in moduli due to void or fiber content may offset each other, which may pose a problem for NDT.

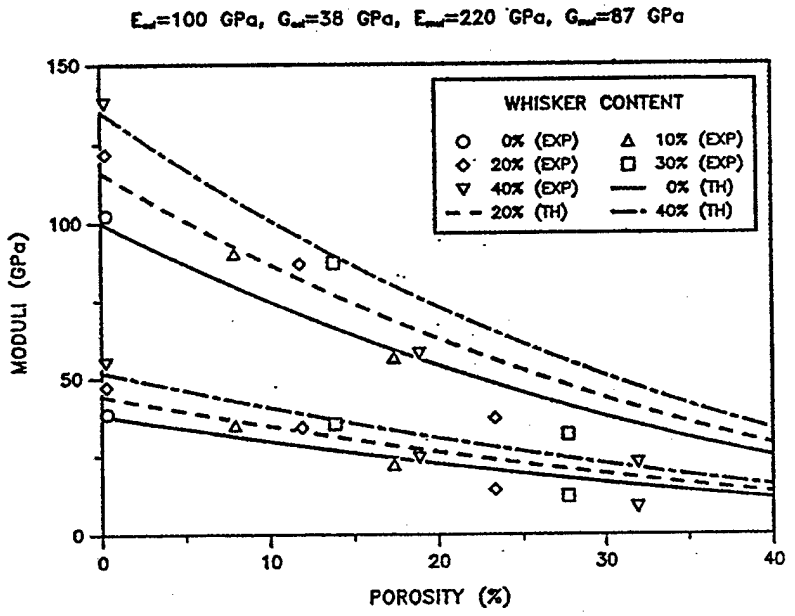

Figure 1. Elastic Moduli of Mullite/Celsian With Voids Th.: Plane Isotropic Through the Thickness Properties

2. Thermal conductivity and loss tangent are affected by fiber and void content and those changes may not be of concern. Changes in conductivity due to porosity can be quite significant (Figure 2) and hence infrared scanning may be an effective NDT tool.
3. Dielectric constant increases slightly with fiber content, but it is more strongly affected by porosity (Figure 3). About 12% reduction occurs due to 10% increase in void content. It is not known whether such a change is acceptable from the point of view of radome performance (effects on signals due to variation in void content). However, NDE techniques like eddy current scanning with a ferromagnetic backing material which employ changes in dielectric properties of the ceramic composite as the key parameter, may be able to detect this change with reasonable accuracy.

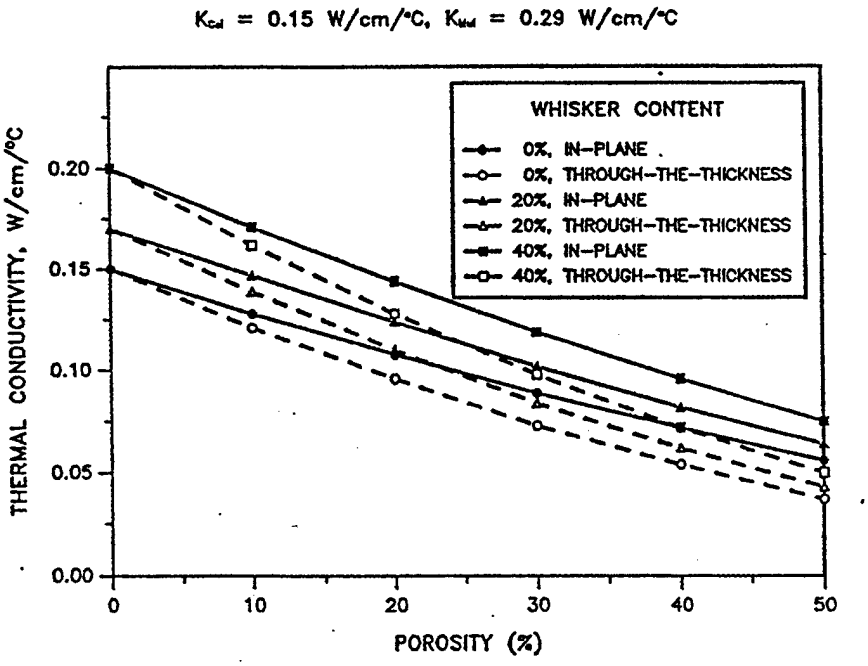

Figure 2. Thermal Conductivity of Mullite/Celsian With Voids: Plane Isotropic Properties

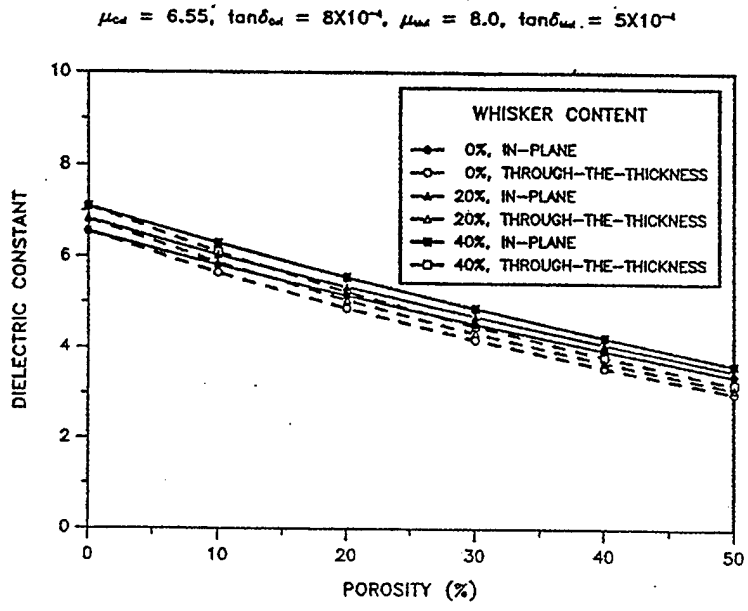

Figure 3. Dielectric Constant of Mullite/Celsian With Voids

4. Strength is strongly influenced by void content (Figure 4), but may not be sensitive to fiber content. Isolated crack like defects can cause additional reduction in strength (Table 1). However, sizes of such defects to cause strength reduction are comparatively large. For example, in a material with 11% void content, crack sizes have to be greater than 0.15 mm to reduce the strength below the level of about 80 MPa. Nondestructive techniques, such as radiography should be able to detect such flaws with reasonable accuracy.

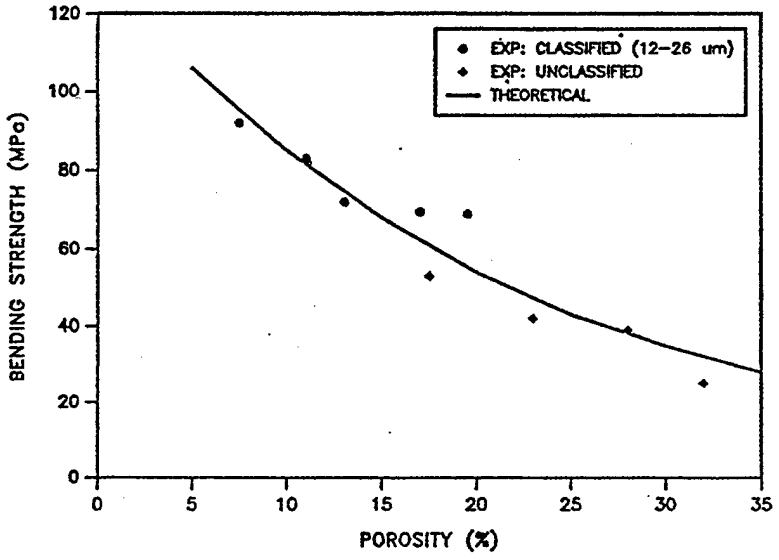

Figure 4. Effect of Porosity on Bending Strength of Celsian Containing Classified and Unclassified Mullite Whiskers

Table 1. Flaw Characteristics to be Detected in Mullite/Celsian

Allowable Strength, MPa	Maximum Void Content Percent	a, Crack of Depth * Greater than, mm
80	11.3	0.15 - 0.3 mm
60	17.7	0.25 - 0.5 mm
40	26.7	0.6 - 1.2 mm

* In materials of thickness greater than 5 time this depth

5. Infrared scanning and optical transmission appear to have good potential for development of practical methods for efficient nondestructive evaluation of samples as well as dome shaped products. However, quantitative data for full or subscale components are required before they can be considered for practical application.
6. Eddy current scanning with ferro-magnetic backing plates may also be useful.
7. X-ray radiography should be useful for quantifying crack like defects, although no tests were conducted in Phase I for this purpose. Use of radiography as attempted in Phase I appears to offer limited potential due to difficulties either with practical implementation or data interpretation.
8. Ultrasonic thru-transmission scans indicate changes in wave velocities caused by fiber and void content differences (Figure 5). Use of ultrasonic or other types of scanning should be useful for dome shaped parts (Figure 6).

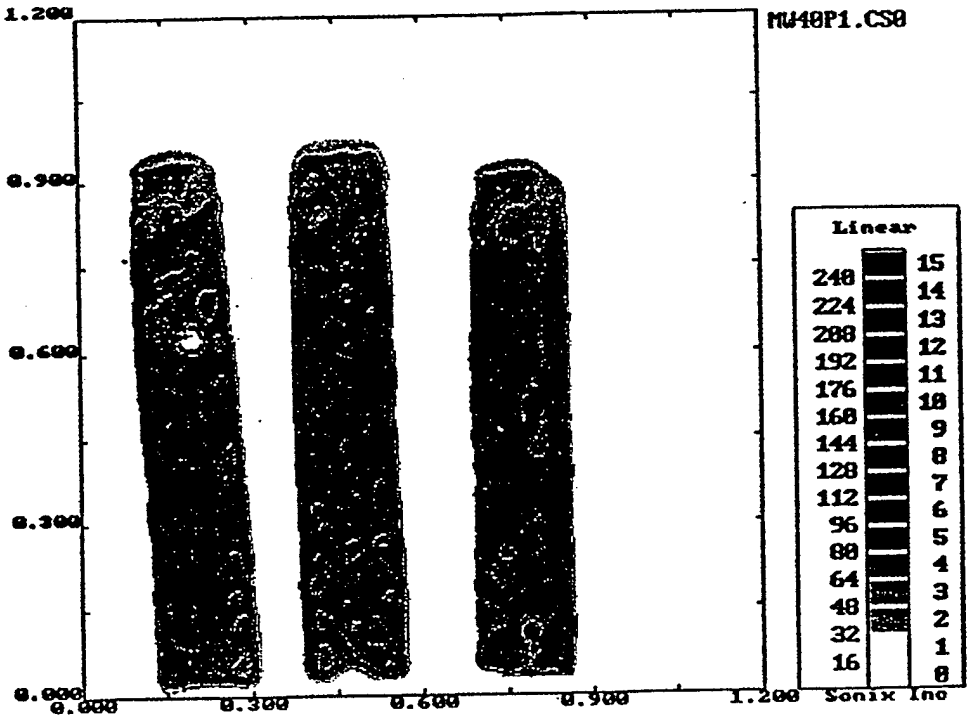

Figure 5. Thru-Transmission Ultrasonic Scan of 40% Mullite Whiskers

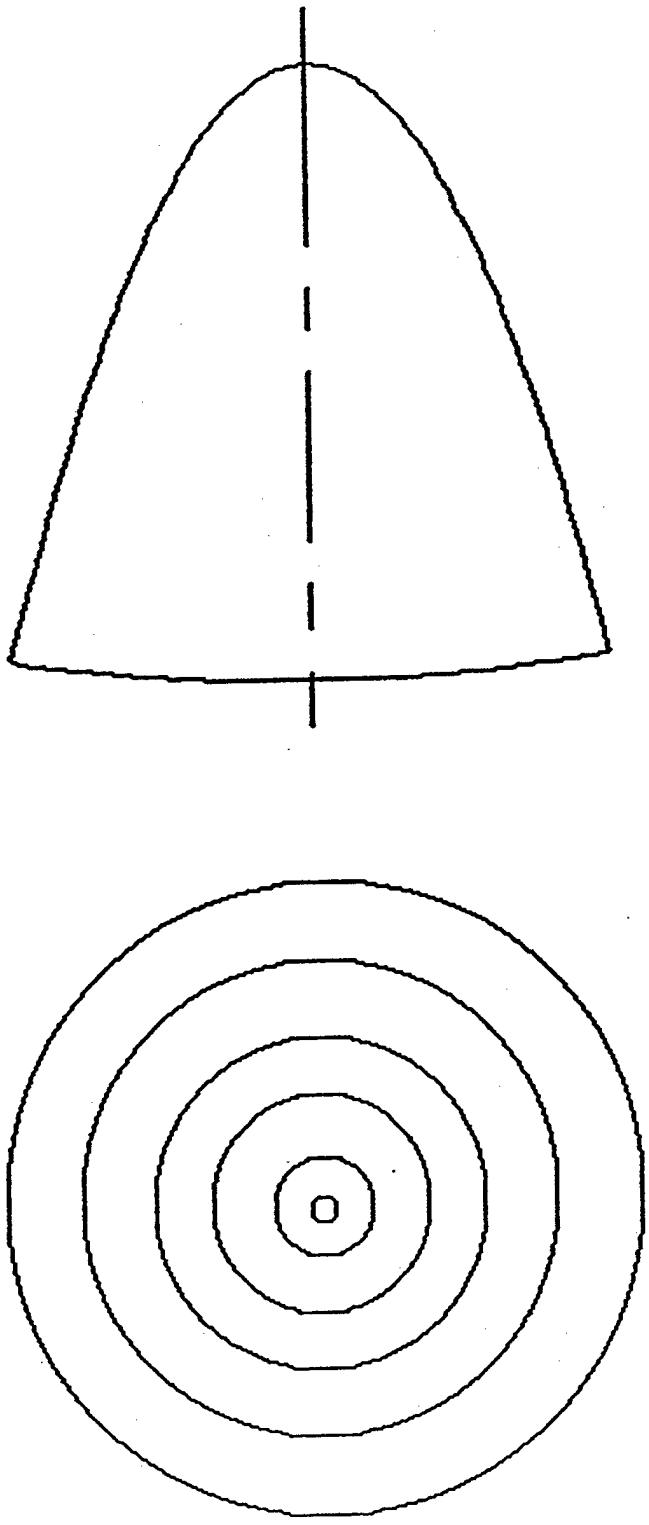

Figure 6. Top Indicates the Generic Axially Symmetric Nature of the Radome While The Bottom Suggests the Display of Concentric Scans

From the results summarized above, it is clear that significant changes occur in sound wave velocities, thermal conductivities as well as dielectric constants due to variations in void content. Also, nondestructive examinations conducted in Phase I show that ultrasonic, infrared and dielectric as well as optical imaging can provide quick quantitative evaluation of reinforced ceramic samples for determining variations in related material properties due to voids. Crack like flaws or large voids can have significant influence on strength and other NDT techniques, such as radiography, are needed for characterizing such flaws. Further development of one or more promising methods, especially for quantitative mapping of property variations over an entire component was the goal of the Phase II work described in the following sections and in Part 2.

PHASE II TECHNICAL OBJECTIVES

Results of Phase I studies (Ref. 8) summarized in the previous section indicate that optical, infrared, dielectric or ultrasonic (thru-transmission) imaging can be useful for determining changes in void or reinforcement content commonly encountered in reinforced ceramics. Presence of voids appears to be the dominant type of anomaly in unreinforced as well as reinforced ceramics (Figure 7). X-ray radiography may also be useful for identifying different kinds of anomalies. However, usefulness of such techniques have to be demonstrated before they can be used for routine application for inspection of reinforced ceramics being considered by the Navy. The specific objectives of the Phase II effort as described in the original proposal are outlined below.

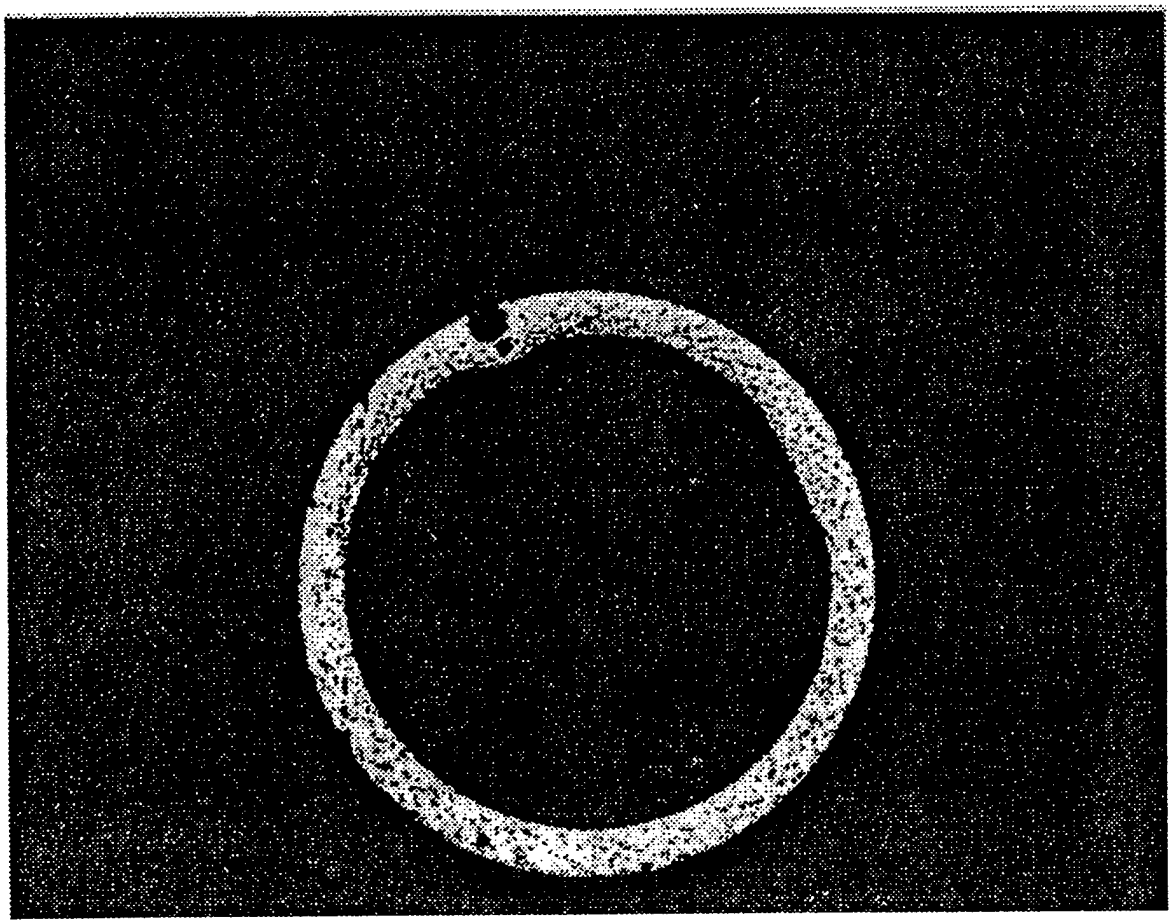

Figure 7. Voids and Porosities in Subscale Celsian radomes (X-Ray Tomogram)

(i) To procure reinforced ceramic samples and components which are being considered for Navy applications.

(ii) To obtain analytical estimates of effects of particle reinforcements, voids and cracks on various material properties such as stiffness, strength and dielectric properties and critical flaw characteristics as well as the influence of dielectric property changes on radome performance.

(iii) To conduct analytical studies of some NDE methods such as dielectric imaging for use and interpretation of NDE data.

(iv) To perform NDE of samples using optical, infrared, dielectric and ultrasonic techniques and/or other methods as needed.

(v) To conduct NDE of components using the most promising methods for detailed imaging over the entire component with appropriately selected data acquisition techniques.

(vi) To perform some destructive tests to generate material property data.

(vii) To correlate data from nondestructive and destructive tests with analyses.

(viii) To deliver representative hardware and software for the most promising NDE methods and to suggest a plan of inspection.

(ix) To suggest procedures for the development of accept/reject criteria.

PHASE II TASKS

The following is a list of tasks originally proposed for the Phase II effort.

1. Selection of materials and procurement of samples/components.
2. Obtain estimates of reinforcements, voids, cracks or other flaws/anomalies, their effects on changes in material properties as well as radome performance.
3. Analytical studies in support of NDE.
4. NDE of samples.
5. Data acquisition during NDE of components.
6. Limited destructive tests.
7. Correlation of destructive tests and NDE data.
8. Inspection plan and representative hardware.
9. Suggestions for accept/reject criteria.

Tasks 6 and 7 were originally proposed for a whisker reinforced ceramic (Mullite-Celsian) for which test material was readily available. By the time the program was started new materials under development (Zr-PSBN) were selected for investigation. Some samples were manufactured for NDE studies, but the number was not enough to generate a reasonable data base. This part of the report (Part 1) summarizes the works performed in the program and the details of work and relevant results from Tasks 1, 2, 3, and 9. Details of sample preparation, experimental studies, inspection plan and hardware (Tasks 1, 4, 5, and 8, performed under the supervision of Professor John C. Drake of VPI&SU) are described in Part 2 of the report.

DESCRIPTION OF WORK

TASK 1. MATERIALS AND REINFORCEMENTS

One material which is being considered for next generation radomes is a Phosphate Bonded Silicon Nitride developed by the ceramics group at NSWC, White Oak. Ease in processing, good water stability, low and thermally stable dielectric constant and loss tangent are some of its attractive properties. Raw materials required are Zirconia powder (30%) and Silicon Nitride particles (70%). Phosphoric acid is used as a bonding agent which reacts with Zirconia to yield some Zirconium Phosphate. It may be noted that the final material may be viewed as Silicon Nitride Particles bonded by Zirconium Phosphate, Residual Zirconia and voids. Residual Zirconia has a very high dielectric constant, but the resulting material has a large percentage of voids which makes the effective dielectric constant of the material quite low. Some samples (with and without flaws) and small components (domes, shown in Figure 8) were manufactured by Jonathan Medding (VPI&SU) at NSWC facilities and were interrogated at VPI laboratories (see Part 2 for details). Scale up is being attempted by Lockheed-Martin Corporation (Dallas, TX) under a contract awarded by NSWC.

Other materials, such as Pyroceram and slip cast fused silica are also being considered for next generation radomes.

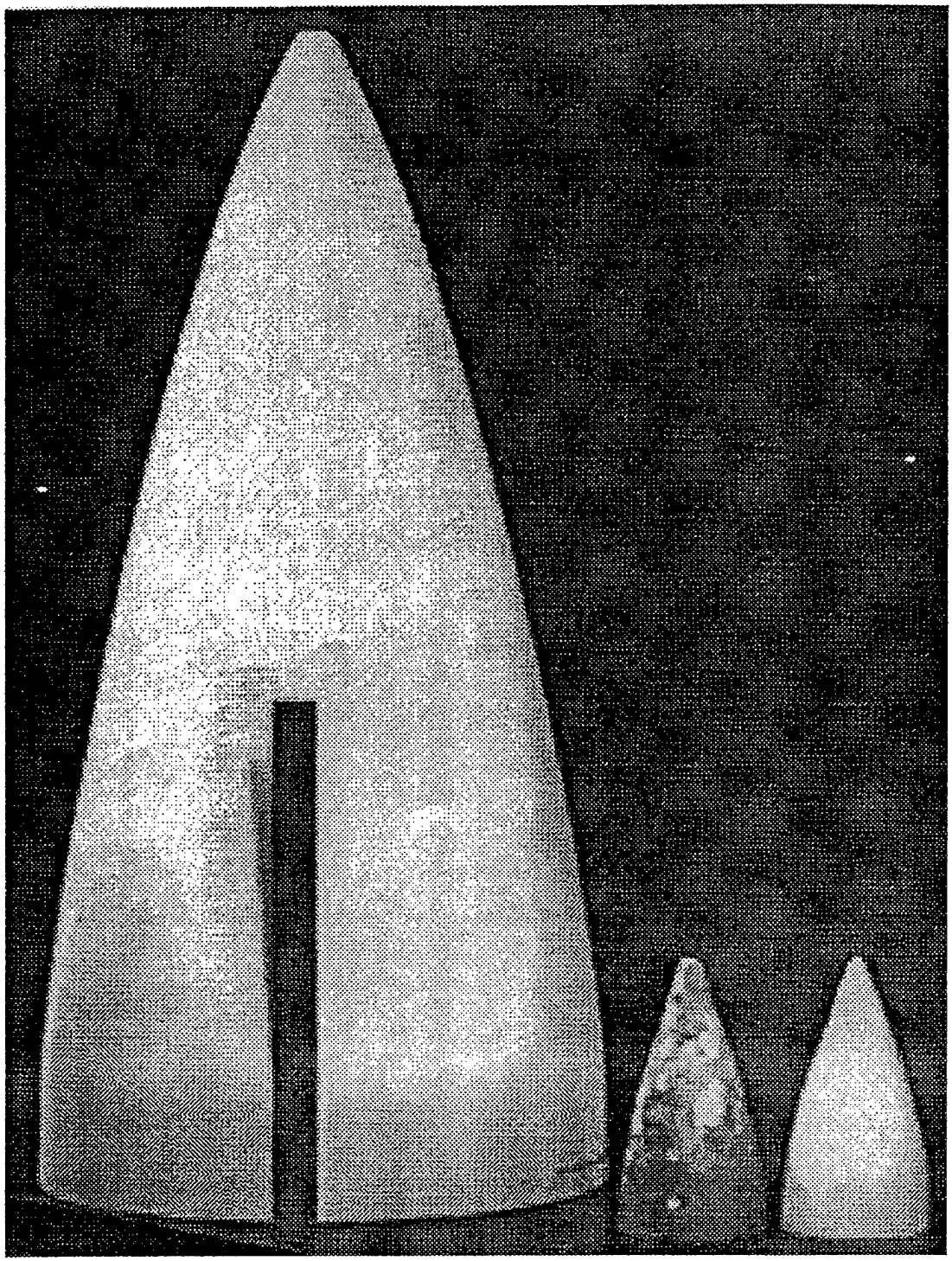

Figure 8. Small Domes Manufactured Compared with a Full Size Dome of a Different Material

TASK 2. ESTIMATES OF PROPERTY VARIATIONS AND EFFECTS ON RADOME PERFORMANCE

Subtask 2.1 Effects of Voids and Inclusions on Material Properties

The base material (Phosphate Bonded Silicon Nitride) investigated also contains about 20% voids and 5% residual Zirconia. Presence of voids is desirable, since it reduces the dielectric constant. On the other hand, residual Zirconia has a very high dielectric constant and any increase in its volume percentage will increase the dielectric constant of the final material. In addition, changes in void and/or Zirconia content over the entire radome may influence its performance. For these reasons, some estimates of the influence of void and Zirconia contents are of interest. Such estimates can be obtained using closed form analytical results for a two phase medium (Ref. 9), where the medium is treated as a composite sphere assemblage. For the purpose of evaluation of the changes caused by voids, it is assumed that the voids are spherical and are distributed over the volume of a parent material. Since the dielectric constant of Phosphate Bonded Silicon Nitride with residual Zirconia is not known, it was estimated assuming that a typical material has a dielectric constant of 5.0 (measured on actual samples by the researchers of the Ceramic Group at NSWC, Ref. 10). Also, because there may be some uncertainty in the actual void content, the dielectric constant of the parent material was estimated for three values of void volume (20, 25 and 30 percent) and these estimates were employed to find expected changes in the dielectric constant with void volume. The results are shown in Figure 9.

Using the same approach, effects of Zirconia content on the dielectric constant were estimated for three values of the base material (with voids) property and the results are shown in Figure 10.

Based on the results shown in Figure 10, the dielectric constant of Phosphate Bonded Silicon Nitride can be estimated and the result is given in Table 2.

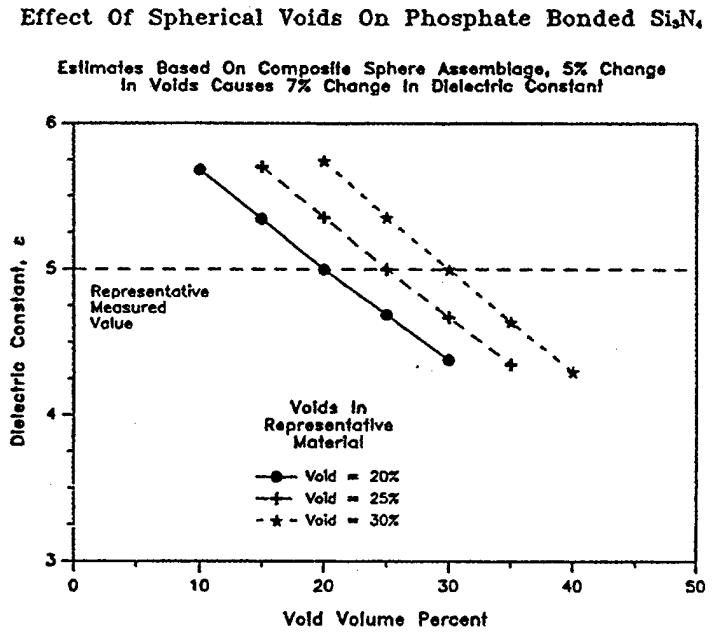

Figure 9. Changes in Dielectric Constant with Void Volume for Three Assumed Values of Void Content in a Typical Phosphate Bonded Silicon Nitride

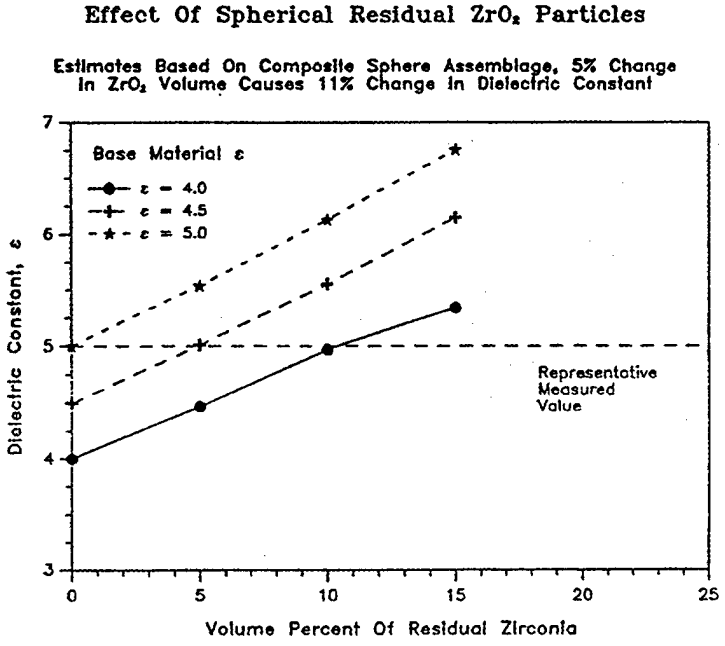

Figure 10. Changes in Dielectric Constant with Residual Zirconia Content for Three Values of Base Material (With Voids) Property

Table 2. Dielectric Constants of Constituents

Material	Dielectric Constants
Silicon Nitride/Zirconium Phosphate	5.8
Voids (Air)	1.0
Zirconia	40.0

Typical zirconium phosphate bonded silicon nitride contains about 20% voids and 5% residual Zirconia. Such a material has a dielectric constant of about 5.0.

Variations of dielectric constant as well as other properties, such as modulus of elasticity, are also useful for judging whether NDE techniques can be used effectively for determining variations in void and/or Zirconia content. Modulus of elasticity of a two phase solid can be evaluated using the methods employed in Phase I studies. Table 3 summarizes the results of changes in material property for a 5% change in void or Zirconia content. The strength variation reported in Table 3 is based on an empirical relation obtained in Phase I for a Mullite reinforced Celsian material. The same relation was used to find the effect of varying void content on strength reported in Table 4. Table 4 also lists the sizes of surface cracks, which must be exceeded, to cause additional strength reduction based on an assumed value of fracture toughness (k_{IC} = 1.8 MPa $\sqrt{m}$). Based on these results, it is possible to identify variation in void content and minimum surface crack depths which should be detected by NDE. These values are underlined in Table 4.

The results of NDE of discs with defects performed in the program (see the summary of works performed in Task 4 in a later section and in Part 2 of the report) show that variations of porosity can indeed be quantified by ultrasonic imaging. Using the results discussed earlier, the changes in the dielectric constant in the porous region can be estimated. Microwave NDE, using a flanged co-axial line or a rectangular wave guide can also yield an estimate of the changes in the dielectric constant. Such changes can have a significant influence on the electromagnetic performance of the radome, such as boresight errors or receiving patterns of the antenna. The next subtask describes the works performed in an attempt to estimate these influences.

Table 3. Summary of Results for a Typical Phosphate Bonded Silicon Nitride

5% Increase in Void Volume Fraction	7% Decrease in Dielectric Constant 10% Decrease in Young's Modulus 5% Decrease in Density 20% Decrease in Tensile Strength
5% Increase in Residual Zirconia Volume Fraction	11% Increase in Dielectric Constant May also influence modulus, density, and sonic velocity

- Some changes in thermal conductivity and thermal expansion are also expected

Table 4. Some Variations and Flaws to be Detected

Void Content	Change in Void Volume	Strength (MPa)	Minimum Surface Depth in mm to Cause Additional Strength Reduction*
20%+	0	88	0.16 - 0.37
22.1%	2.1	80	0.20 - 0.45
25.1%	5.1	70	0.25 - 0.58
28.5%	8.5	60	0.35 - 0.80

* Based on assumed fracture toughness 1.8 MPa $\sqrt{m}$ for all cases.
\+ Assumed as representative material
Underlined variations/flaws should be detectable by NDE

Subtask 2.2 Effects of Patch Defects on Radome Performance

The primary function of the radome is to provide an enclosure for the antenna. It would be ideal to have a radome with sufficient strength to withstand environmental effects and

aerodynamic loads, but with a low dielectric constant to allow electromagnetic waves to pass through it with very little changes in direction and attenuation. However, since the dielectric constant of the radome materials is always greater than that of air (unity), the apparent direction of arrival of a target return can be different from the true direction. The bias of the apparent direction towards azimuth (x_A) (or elevation (y_A)) axes of the antenna is called the azimuth (or elevation) boresight error, which is usually measured in milliradians (MRAD). Boresight error varies with the orientation of the direction of target return (z_A axis of the antenna) with respect to the radome. Estimates of boresight error variation and its slope (with respect to the change in the direction or gimbal angle) based on calculations and/or experimental measurements are often used to determine the correct direction of the target return. As discussed earlier variations of dielectric properties are expected in ceramic or ceramic composite radomes over a finite sized region (a patch) due to changes in porosity or reinforcement content. Such variations will obviously influence the boresight error and it is of interest to obtain an estimate of these variations due to such a patch type defect (Figure 11). Experimental measurements with patches of different sizes and different dielectric properties would involve an elaborate program and were, therefore, beyond the scope of this effort. Therefore, in this subtask an attempt was made to estimate the influences of patch type defects using the computer code RACP™ (Radome Analysis Computer Program, Ref. 11) obtained from scientific Software, Maitland, Florida.

The RACP™ code is quite versatile and allows evaluation of boresight errors for different types of radomes with variable thickness and properties as well as monopulse antenna near fields (receiving patterns) for various polarizations of the incident plane wave and the antenna. However, in its present form the code does not allow for consideration of a patch type defect in the radome. The code was, therefore, modified to consider such property variations over a region bounded by two prescribed axial coordinates (z) and circumferential coordinates (ϕ) as shown in Figure 12. Since it is expected that the property change will be maximum at the center of the patch and will reduce to zero at its boundaries, it is assumed that the property change (real and imaginary part of the dielectric constant or thickness) is of the following form

$$\Delta = \Delta_o \cos\frac{\pi(z - z_1)}{\ell}\cos\frac{\pi(\phi - \phi_1)}{\theta} \qquad (1)$$

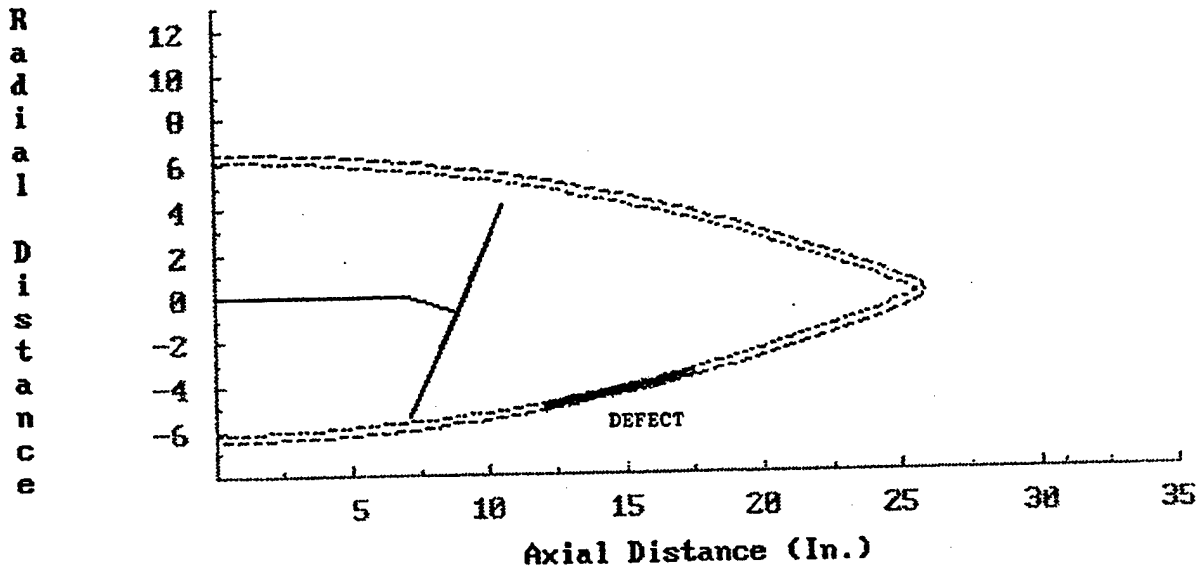

Figure 11. Radome with a Patch Defect, p. 8x

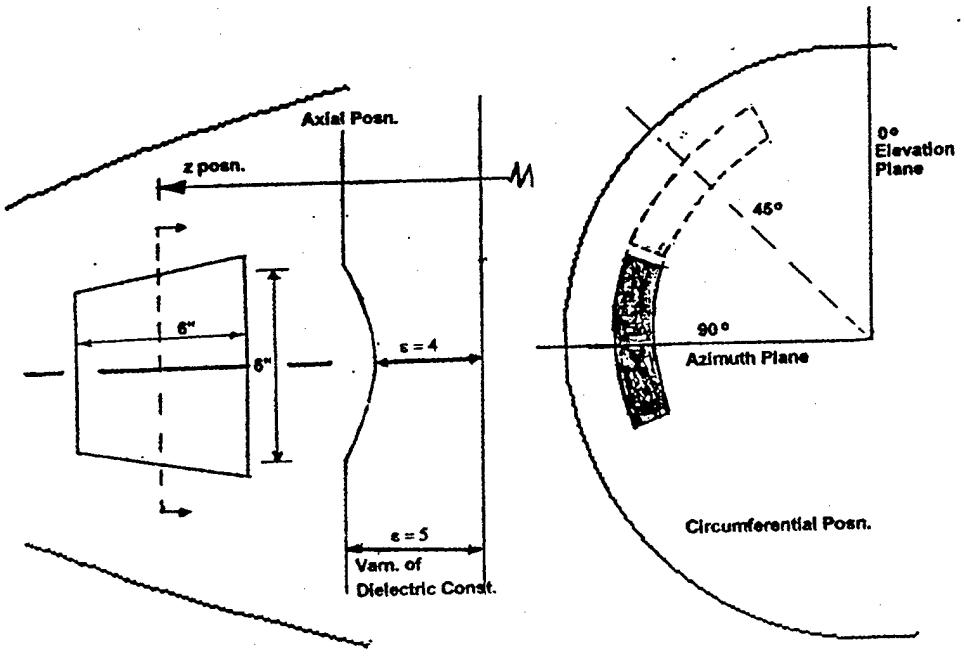

Figure 12. Dielectric Property Validation and Position of the Patch p. 8y

where z_l and ϕ_l are the coordinates of the center of the patch and ℓ and θ quantify its dimension in axial and circumferential direction. It may be noted that ϕ_l defines the relative angular position of the patch with respect to the antenna. $\phi_l = 90°$ when an axial plane (through radome z-axis) passing through the center of the patch coincides with the azimuth plane ($x_A z_A$) of the antenna (Figure 12). For $\phi_l = 0°$, the axial plane coincides with $y_A z_A$ or elevation plane of the antenna (Figure 12).

A typical tangent ogive radome shown in Figure 11 was considered for demonstration purposes. The following geometric and material properties were used (Figure 13).

Radome base diameter, D_{OS} = 12.88 inch
Radome length, L_{OS} = 26.43 inch
Bulkhead z coordinate, z_{BOT} = 0.0 inch
Antenna Aperture Radius, R_{ap} = 5.0 inch
Gimbal point from radome base, R_R = 7.057 inch
Antenna aperture offset from gimbal, R_A = 1.908 inch
Frequency, F = 11.803 GHZ
Radome wall thickness, DIN = 0.351 inch
Dielectric constant ε_r, ER = 5.0
Loss tangent, TD = 0.03

For estimation of changes in boresight errors due to the patch, the dielectric constant, ε_r, at center was assumed to be 4.0 (Figure 12). For estimation of changes in receiving patterns one more value of ε_r at the center of the patch (ε_r = 2.0) was also selected.

Patches of trapezoidal, but nearly square, shapes (dimensions in the z direction equal to that in circumferential direction at $\phi = \phi_l$) were considered. Figure 12 illustrates such a patch of dimension 6" in both directions. In the results presented here and in Appendix A, where additional results are given, a defect of size 6" (or 4") implies such a nearly square shaped patch.

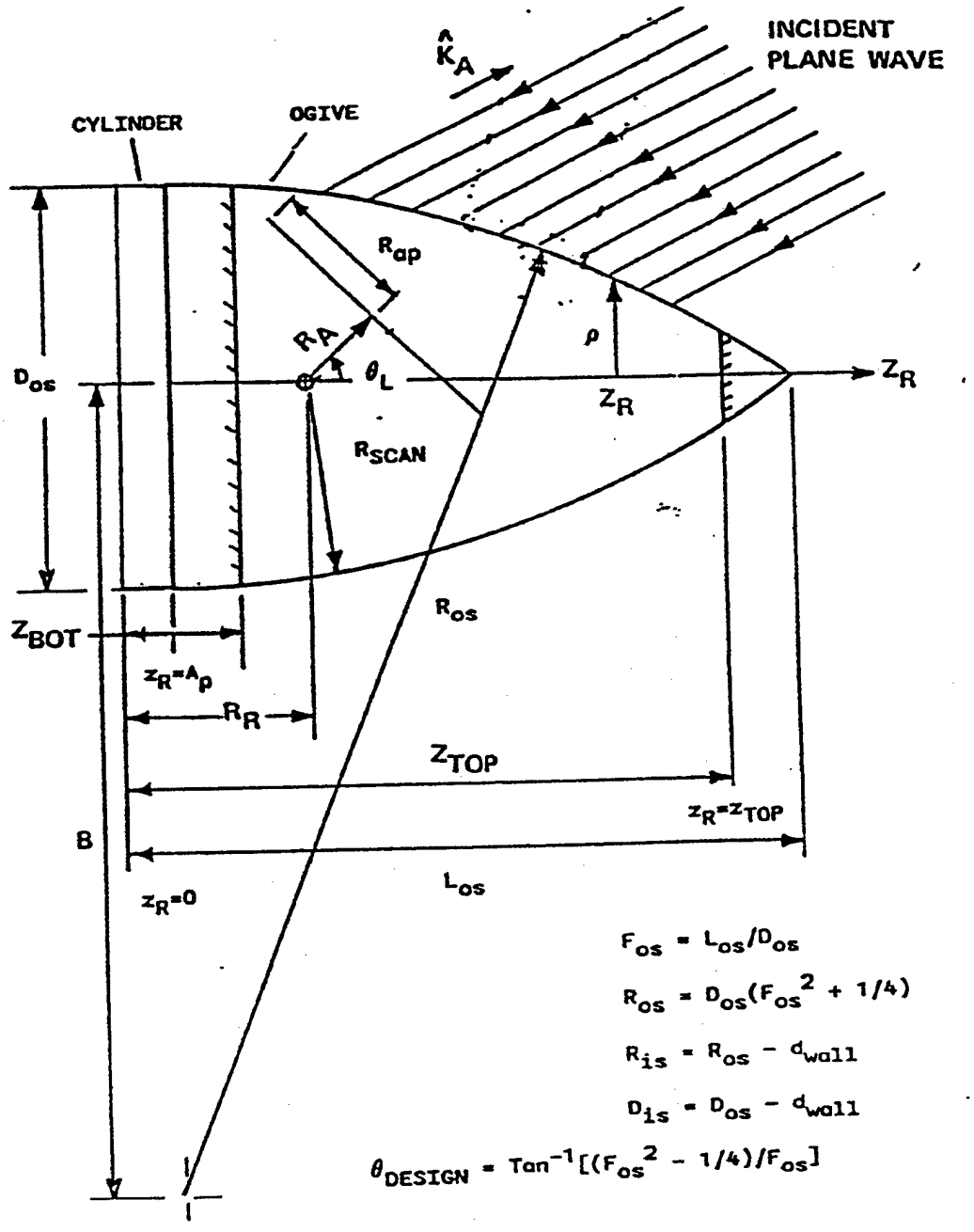

Figure 13. Geometry of Dimensions of Radome and Antenna

Figure 14 shows the variation of the azimuth boresight error for a vertically polarized antenna and incident wave with yaw gimbal angle θ_L (the $x_A z_A$ plane of the antenna lies in the plane of the paper in Figure 13) and the patch size. It may be seen that, as expected, for positive values of θ_L (normal to antenna plane z_A moving towards the defect) the azimuth boresight error increases with the patch size. A patch size higher than 6" causes the boresight error to increase tenfold (for $\theta_L \approx 8°$), but below 6" it increases about three times and may be acceptable if appropriate corrections are made to account for the presence of the defect. On the other hand, Figure 14 shows that, for obvious reasons, the boresight errors are less influenced for negative values of θ_L.

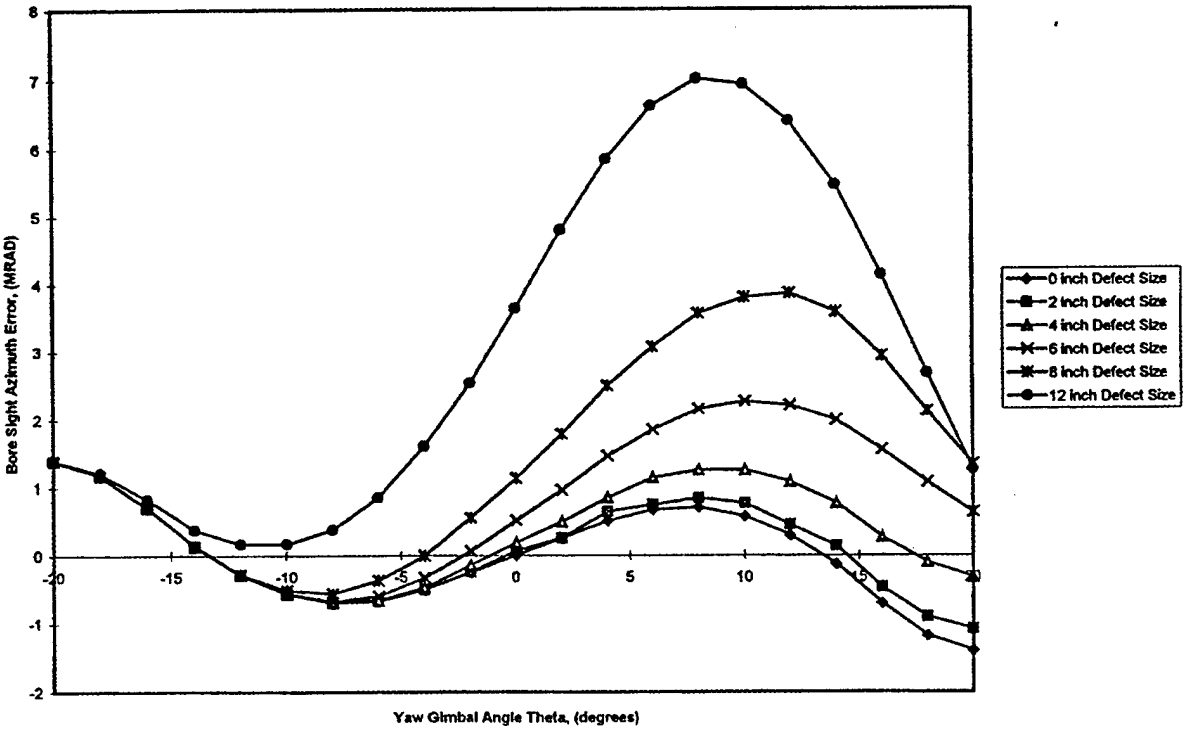

Figure 14. Effect of Defect Size at 90 Degree Position and z = 15 in. on Bore Sight Azimuth Error for Vertically Polarized Antenna and Incident Wave

Figure 15 shows the variation of the azimuth boresight error for a right hand circularly polarized antenna and a vertically polarized incident wave for a fixed patch of size 6" (and for no defect) with yaw gimbal angle θ_L and different angular position of the defect (ϕ_1 = 90° to 0°). Although the boresight errors change quite a bit for all values ϕ_1, but they

may still be acceptable. However, the final decision regarding acceptability can only be made after some tests are performed with some patches of different sites and locations and the data are correlated with the analytical results.

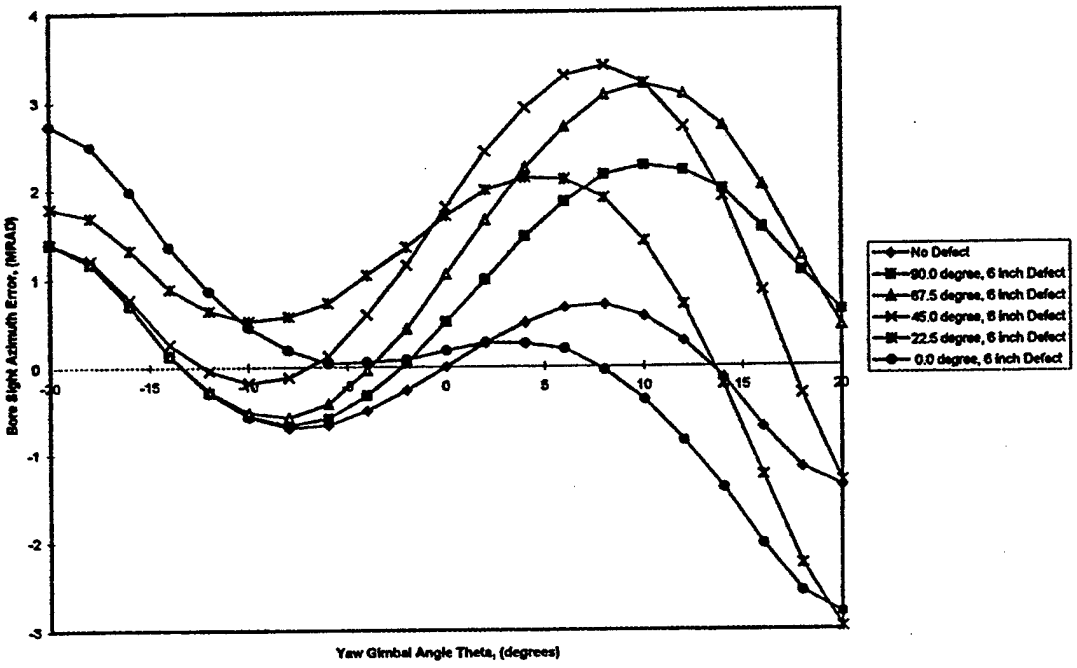

Figure 15. Effect of Angular Position of 6 in. Defect at z=15 in. on Bore Sight Azimuth Error for RHC Polarized Antenna and Vertically Polarized Incident Wave

Effects of a 6" size patch with ε_r = 4.0 and 2.0 on the receiving pattern of the antenna (sum channel amplitude and phase at azimuth cut) are shown in Figures 16 and 17. Some changes are noticeable, but the differences from no defect case for ε_r = 4.0 are less than that for ε_r = 2.0.

Additional results and the details of changes in the input data required to consider the effects of patch defects are described in Appendix A.

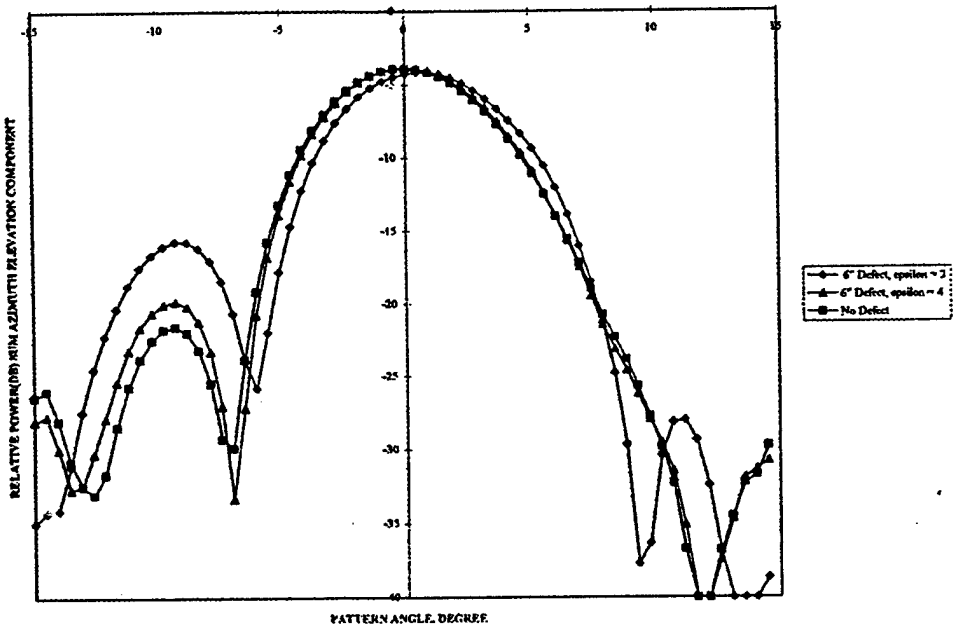

Figure 16. Effect of Defect on Receiving Pattern - Sum Channel Amplitude Azimuth Cut

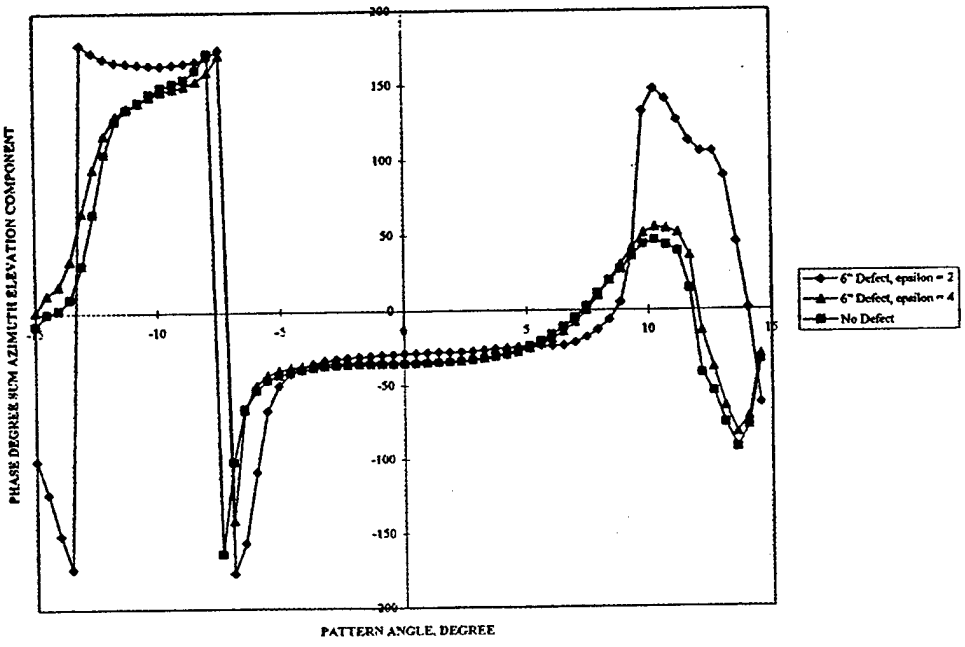

Figure 17. Effect of Defect on Receiving Pattern - Sum Channel Phase Azimuth Cut

TASK 3. ANALYTICAL STUDIES OF NDE METHODS

Since the primary interest is in the electromagnetic properties of the material, it should be useful to determine variation of the dielectric constant (or other related responses) of the material over an entire part using NDE techniques. Open-ended wave guide type sensors are attractive devices suggested by various investigators. In this technique, the material (a ceramic plate or shell) is interrogated using a flanged open-ended rectangular wave guide or a co-axial line and the changes in the actual or normalized admittance of the wave guide (or voltage standing wave ratio, VSWR and phase of the reflection coefficient) are measured. These changes can be related to those in the dielectric constant of the material due to voids (and/or delaminations). There are many other factors which affect the admittances, such as backing material (on the other side of the wave guide) and any gap between the flange and the material. Analytical studies and results are useful to determine the effects of such parameters, such that suitable care can be taken during measurement. In addition, the results can be used for analysis and interpretation of data. Therefore, a computer code has been written to perform such analytical calculations. Mathematical procedures and numerical methods employed are presented in Appendix B of the report.

Appendix B also describes the input data required for approximate evaluation of the admittance of the rectangular wave guide or the co-axial probe used for interrogation of a layered dielectric medium. A listing of the computer code is also included. Figures 18 and 19 show the changes in the normalized conductance and susceptance of rectangular wave guide sensor (of dimensions 0.9" x 0.4") due to the expected variations in the dielectric constant of a typical Phosphate Bonded Silcon Nitride plate of thickness 0.2" backed by air. Results are given for two cases (no air gap and an air gap of 0.02" between the sensor and the plate) and three frequencies. The results show that the charges in susceptance are very sensitive to the dielectric constant at a frequency of 8 GHz (Figure 18) and are also strongly influenced by the presence of the air gap. Therefore, a frequency in the neighborhood of 8 GHz may be suitable for interrogating the material and careful consideration should be given to the presence of unavoidable air gap during measurements. The effect of the air gap on measurements using a co-axial probe and correlation of such test data with analytical results are discussed later.

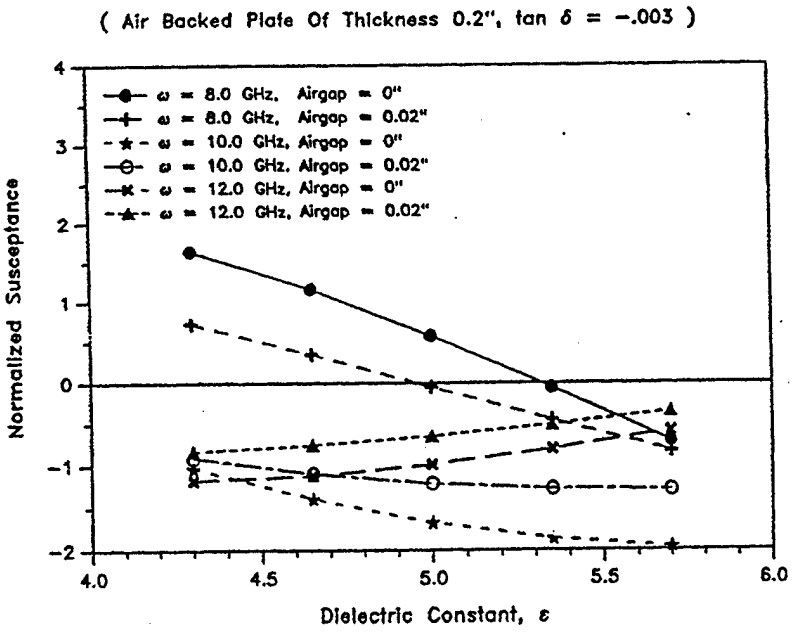

Figure 18. Normalized Susceptance vs. Dielectric Constant of Phosphate Bonded Silicon Nitride

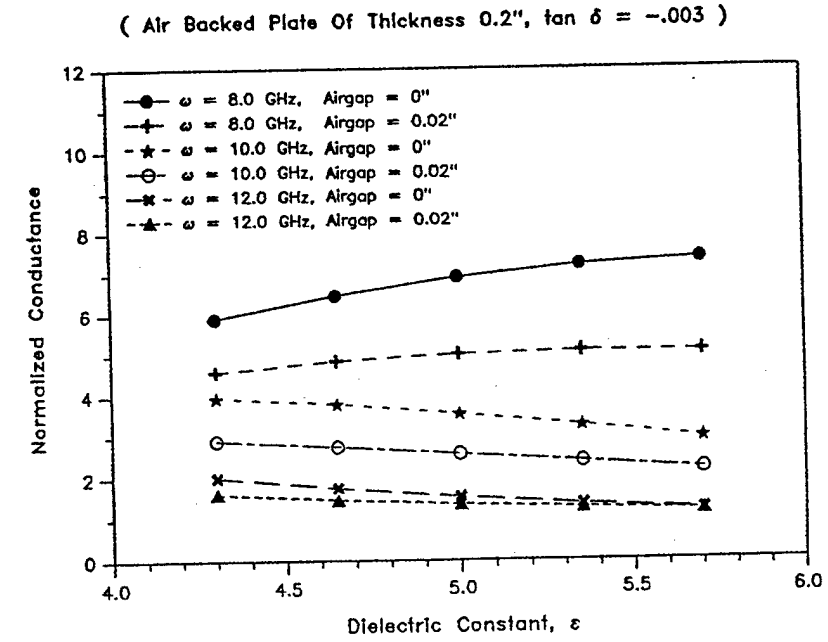

Figure 19. Normalized Conductance vs. Dielectric Constant of Phosphate Bonded Silicon Nitride

As discussed in Appendix B, a series solution can also be obtained (instead of that in terms of a double integral) by employing the calculation of residues. However, determination of the poles of the integrand (in the integral) is a complicated process, when several layers are involved. The poles can be determined easily for the case of a conductor backed slab of one material. Some results of computation for a rectangular wave guide are given in Appendix C. It may be noted that with an accurate integration scheme (some times up to 12,000 integration points are required for one integral), the results from the two approaches (integral and series) are identical and they compare reasonably well with some of the results reported by Bakhtiari (Ref. 12). However, some of Bakhtiari's results (Ref. 13) do not agree with those obtained using the series and the integral. It is likely that these solutions of Bakhtiari are either not reported correctly or the error may be the result of inaccurate evaluation of the integrals.

Results of a detailed parametric study on the effects of air gaps (0 to 0.5") and frequency (8 to 12 GHz) on the actual conductance and susceptance due to a dielectric material ($\varepsilon_r = 2.8$, $\tan\delta = 0.05$) of various thicknesses (0.075", 0.125", 0.235", 0.38" and a half space) are presented in Appendix D. The results show that for slabs of small thicknesses (0.075" and 0.125"), small air gaps (up to 0.1") have a small influence on the conductance for a frequency of 8GHz, but the susceptances tend to decrease rapidly with air gap thickness.

Dielectric properties of layered materials are often influenced by air gaps or delaminations, which may be present between the layers. Use of microwave NDE for detecting the air gap at such delaminations has been suggested by some investigators. In this approach the sensor (a rectangular wave guide) is placed in front of a coupling dielectric sheet, which is backed by the specimen being interrogated. An unintentional air gap is usually present between the coupling material and the specimen surface. This is called the lift-off effect and one first attempts to find the direction of the change in the tip of the vector (complex reflection coefficient) due to small lift-off (air gap). This direction (that of the change) is called the lift-off direction. For the purpose of detecting the presence or absence of a delamination type air gap inside the specimen, the change in the component of the complex reflection coefficient vector, which is orthogonal to the lift-off direction, is normally used, so as to minimize the lift-off effects produced by wobbling of the wave guide and the coupling sheet over the specimen during scanning. At certain frequencies the lift-off is a minimum

and the orthogonal component is a maximum. Appendix E describes the results of a parametric study to find the frequency ranges which should be used so as to minimize the lift-off effect.

Appendix F gives some comparison of results obtained using the computer code ADMIT for the co-axial line with the results presented by Bakhtiari et al (Ref. 14) and Li et al (Ref. 15) The results show that the computer code is free from any bugs and the results can be used with confidence for selecting frequencies and other parameters for interrogating specimens.

In Appendix G, an attempt is made to correlate experimental observation of Liu (Ref. 16) on air gap and other effects on measurement of dielectric properties of glass fiber reinforced composites using the commercially available Hewlett Packard 85070a co-axial probe (Ref. 17). The probe appears to be a useful tool for interrogating specimens for detecting variations in dielectric properties.

TASK 4. NDE OF SAMPLES

Details of works performed at VPI&SU are given in Part 2 of the report. Phosphate Bonded Silicon Nitride (PBSN) disc samples prepared for the program (see Task 1 described earlier and Part 2 of the report) were examined using ultrasonic, infrared (thermal), optical reflection/transmission and microwave imaging. Transmitted light was not found to be a viable technique for inspection. Internal flaws (such as voids) could be detected using infrared technique when a temperature gradient was introduced across the thickness. Ultrasonic inspection was found to be a useful tool for characterizing flaws due to porosity, delamination, crack and metal powder inclusions in the disc samples. Since the pores reduce the effective modulus of the material, they reduced the velocity of sound in PBSN (Figure 20). On the other hand, when immersed in water for about four hours, the pores absorbed water and the compressive wave speed of PBSN increased due to the incompressibility of the water trapped in the pores (Figure 21). Water immersion is also useful since water acts as a good coupling agent for transmission of ultrasonic waves. Microwave images of the discs obtained using a rectangular wave guide (with dimensions 0.9" x 0.4" and a frequency range of 8.2 GHz to 12.4 GHz) are shown in Figure 22. It may be noted that since the wave guide dimensions are not small, there is distinct edge effect near the free edges of the

discs, but these effects should not be of importance for inspection of larger samples or dome shaped radomes.

C-SCAN PLOT COLLECTED ON: Wed Jan 24 17:24:34 1996

PART I.D. Number:	disc 4	PART TYPE:	disc
Operator:	Jon	Transducer Type:	25 MHz
Transducer S/N:		Transducer Mfr:	Panametrics
Nominal Cntr Freq:	25 MHz	Attenuation:	14
Energy:	4	Damping:	0
Gain:	60 dB	HP Filter:	.03
Commentl:	1/24/95	Comment2:	
Comment3:		Comment4:	

Disc was constructed to have a porosity gradient. The center of the porosity "well" appears to be slightly off from the disc's center.

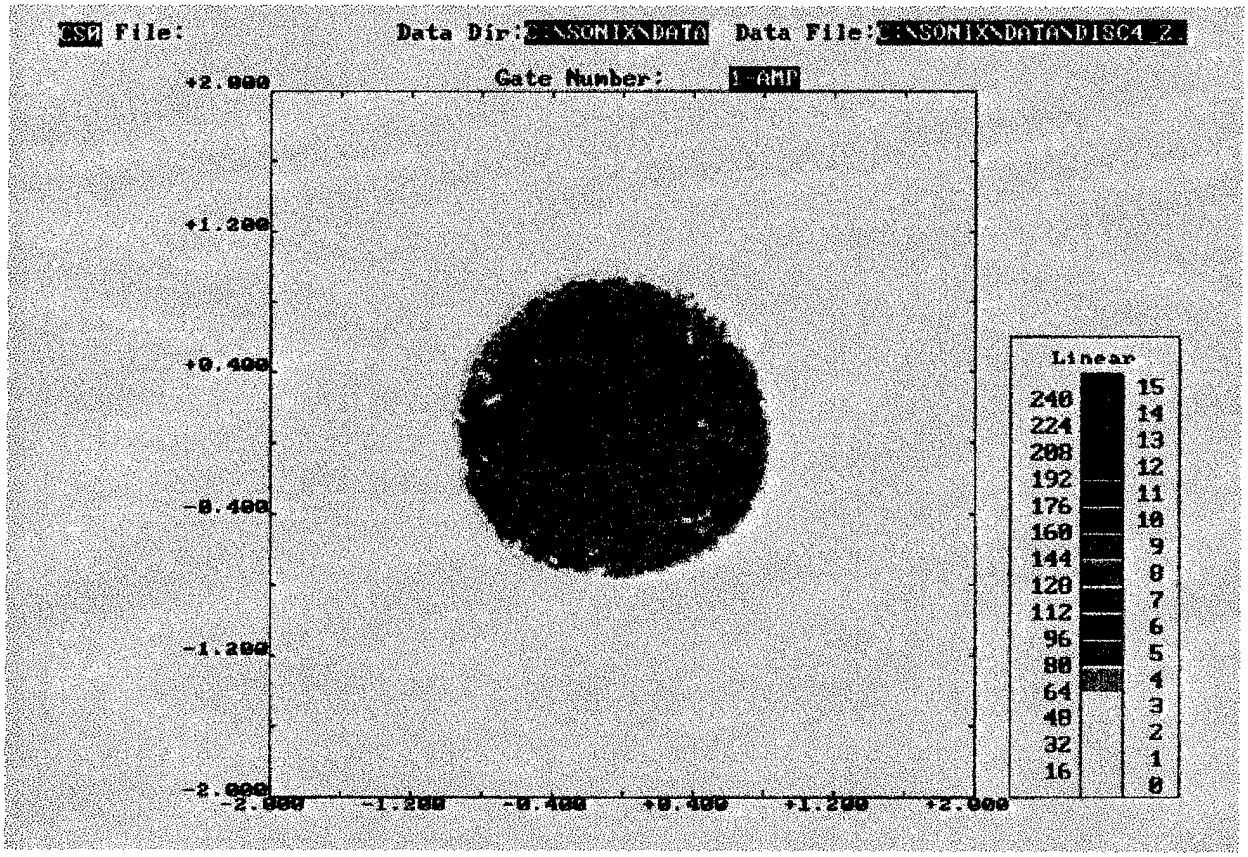

Figure 20. Ultrasonic Image of a Disk #4 with a Porosity Gradient

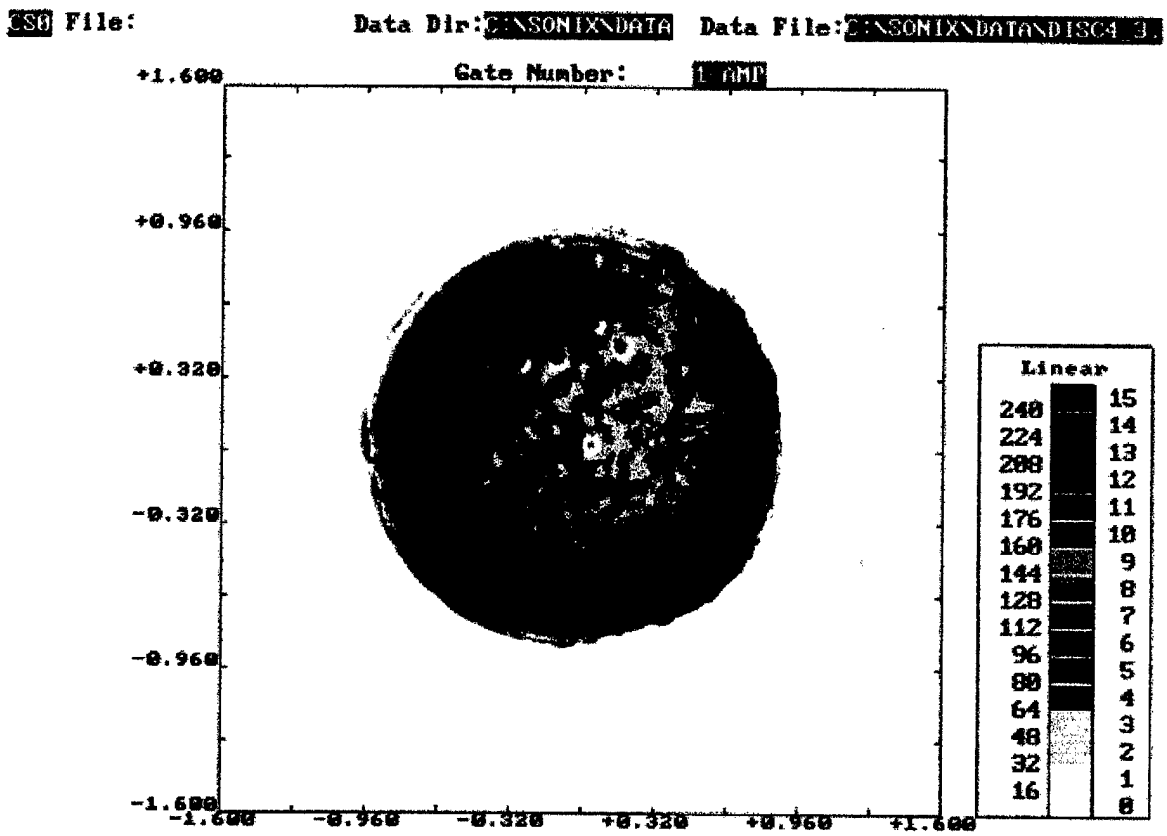

Figure 21. Ultrasonic C-Scan of Disk #4 after more than four hour of immersion

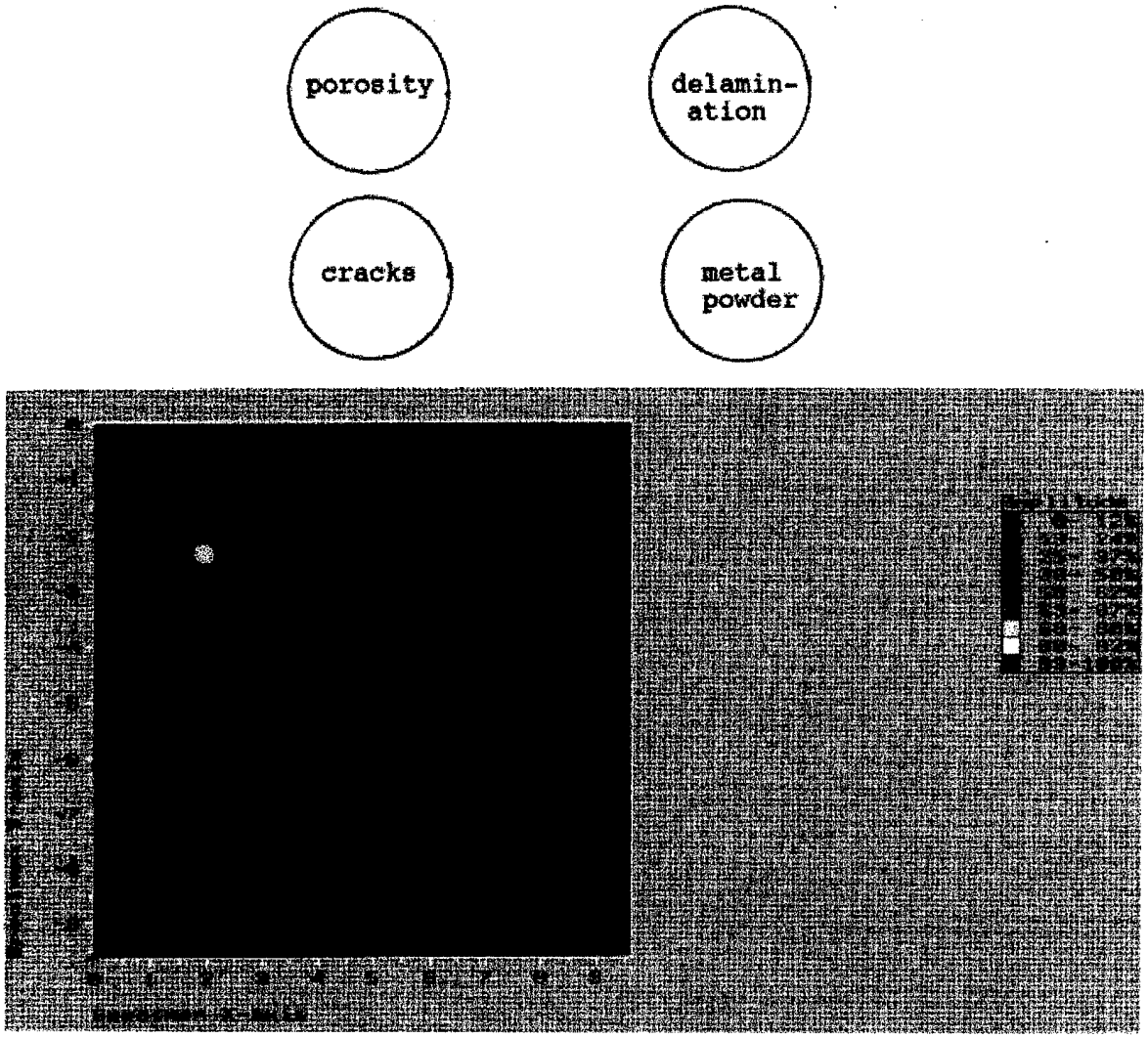

Figure 22. Microwave Images of Discs using the Rectangular Wave Guide Probe

TASK 5. DATA ACQUISITION FROM NDE INSPECTION

Based on the evaluation of NDE methods, it was determined that a reliable assessment of ceramic composite radomes made of materials similar to PBSN would require ultrasonic pulse echo scanning and/or microwave NDE. A commercially available scanning package (hardware and software from Sonix) capable of collecting data (ultrasonic wave form) at digitization rates as high as 800 MHz, using a variety of scan procedures while tracking the amplitude and time of flight signals within eight separate gates, was selected. The hardware was adopted to a custom design developed at VPI&SU for rotationally symmetric bullet (radome) shaped hollow objects. Another software package capable of displaying NDE data at a moderate level of resolution (for scans at moderately high speeds) and also at a higher resolution (for more careful scanning in selected areas) was utilized. A detailed description of data collection and data display procedures is given in Sections IV and V of Part 2 of the report.

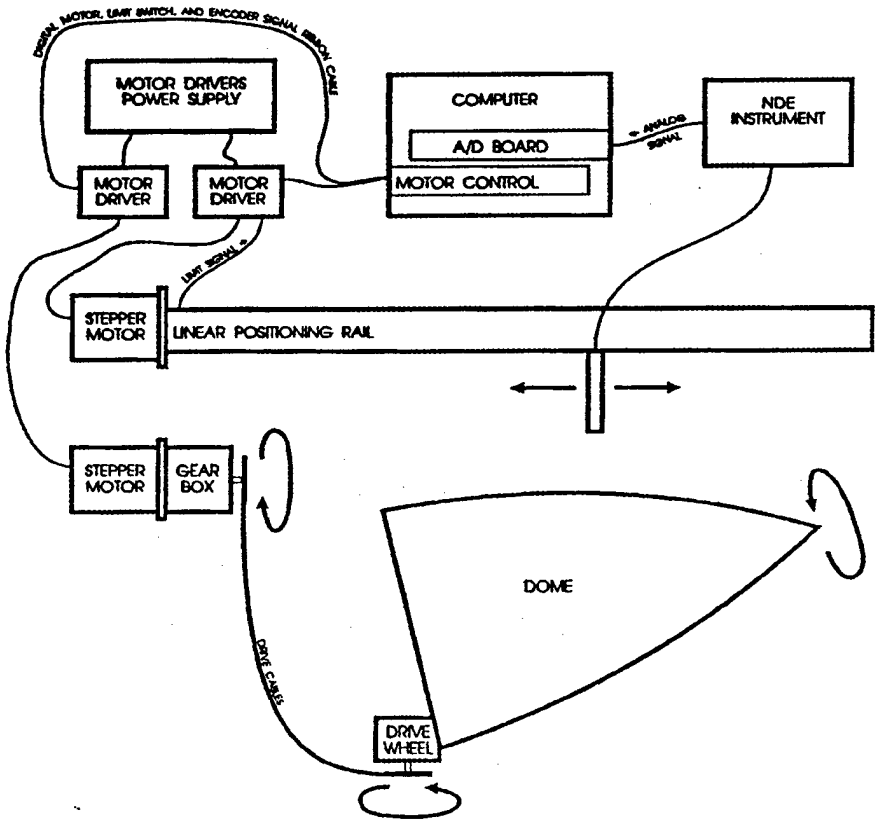

Figure 23. A Schematic Drawing of the Inspection System

TASK 8. INSPECTION PLAN

Considerable effort was directed in selecting an inspection plan that would combine economy, flexibility, and reliable application of ultrasonic and/or microwave NDE to radomes of different sizes. A combination of commercially available computer hardware and software, fixtures and circuitry units designed and fabricated at VPI&SU, as well as various components such as the stainless steel holding tank available from NSWC, were utilized. Figure 23 gives a schematic diagram of the system. The NDE unit can be either a microwave network analyzer or an ultrasonic pulser/receiver. For ultrasonic scanning, the dome supported by a cradle has to be immersed in water in a holding tank. A full description of the holding tank, the dome cradle and rotation system, the probe holder and the translation system, the motion control and data acquisition system, various computing hardwares and softwares, as well as a description of the scanning procedure is given in Part 2 of the report. Some images which were also obtained for a full scale radome supplied by NSWC. The material for the radome was, however, not PBSN. Some examples of these images (peak and TOF) with inherent impressions and seams, etc., are shown in Figures 24-27. Images of introduced defects (dents and cracks) at different resolutions are illustrated in Figures 28-31.

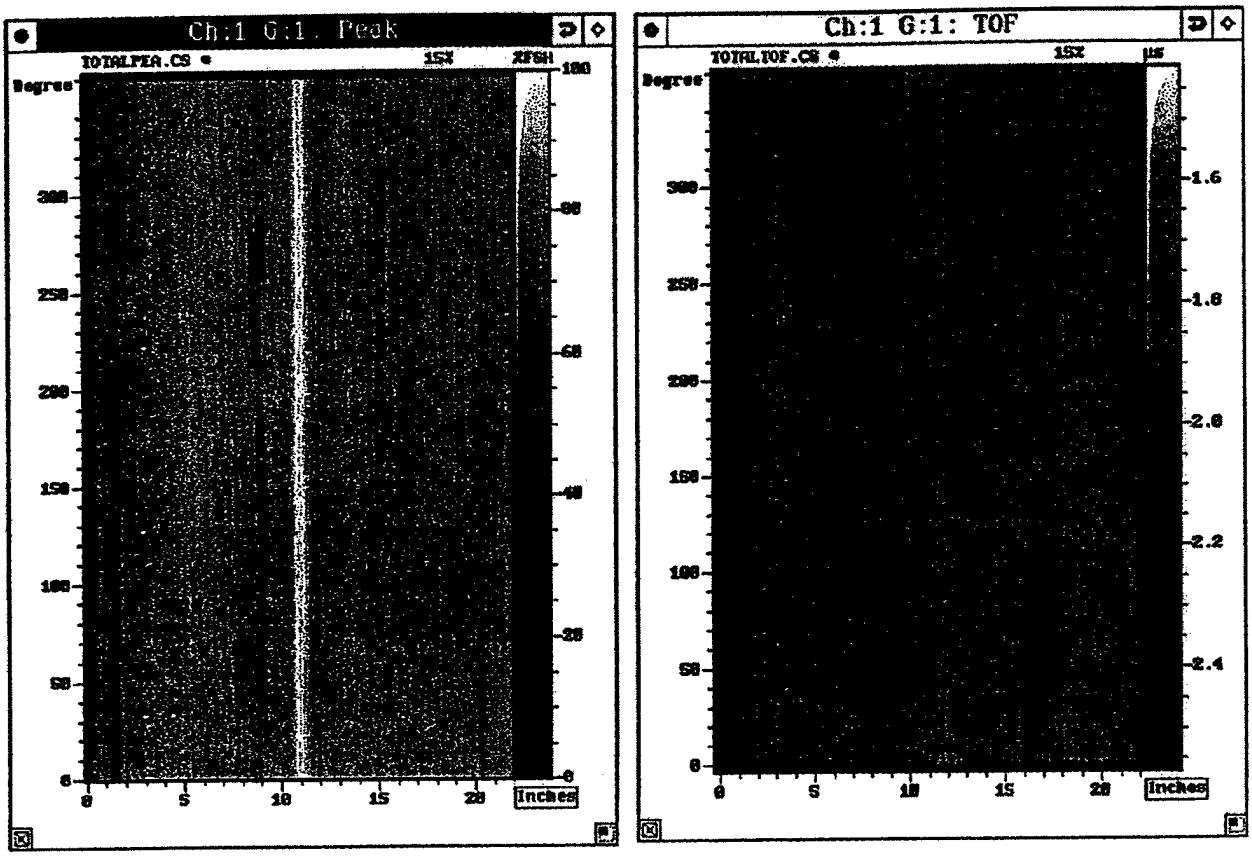

Figure 24. Inherent Impressions and Seams (Complete Image)

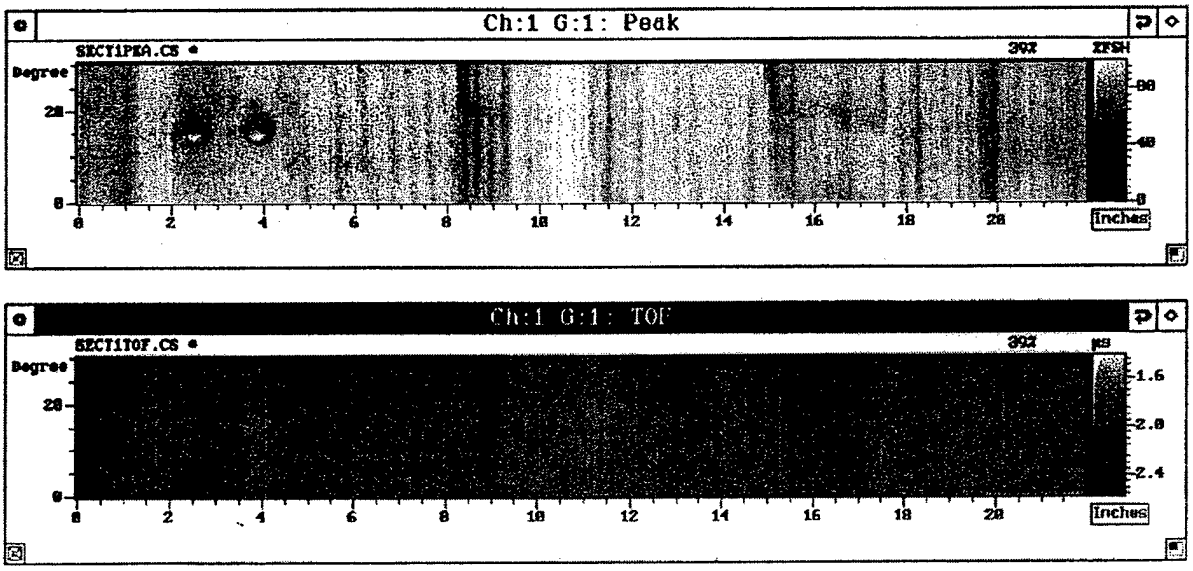

Figure 25. Impression and Seams (Smaller Area)

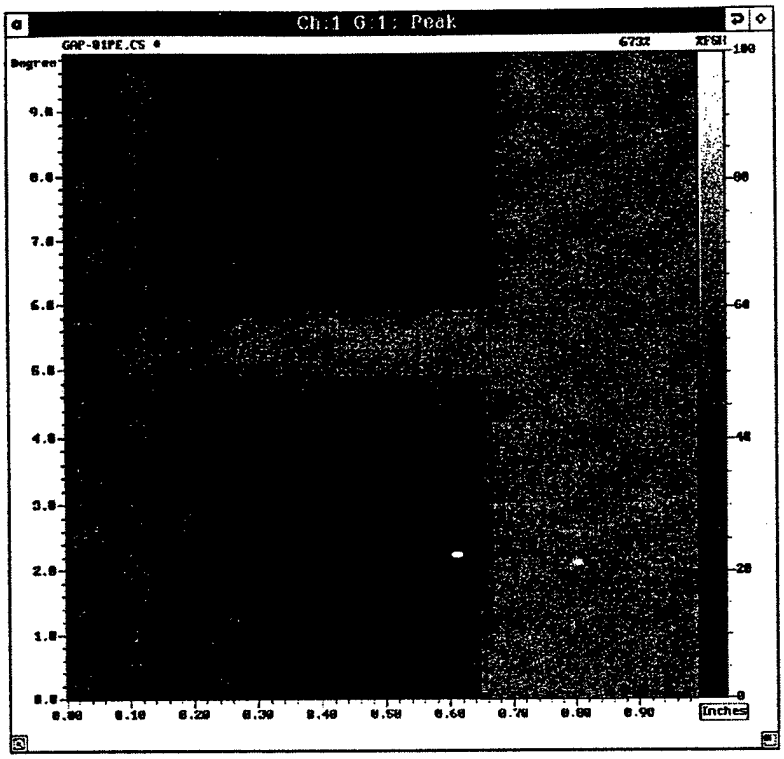

Figure 26. Inherent Impressions (Peak)

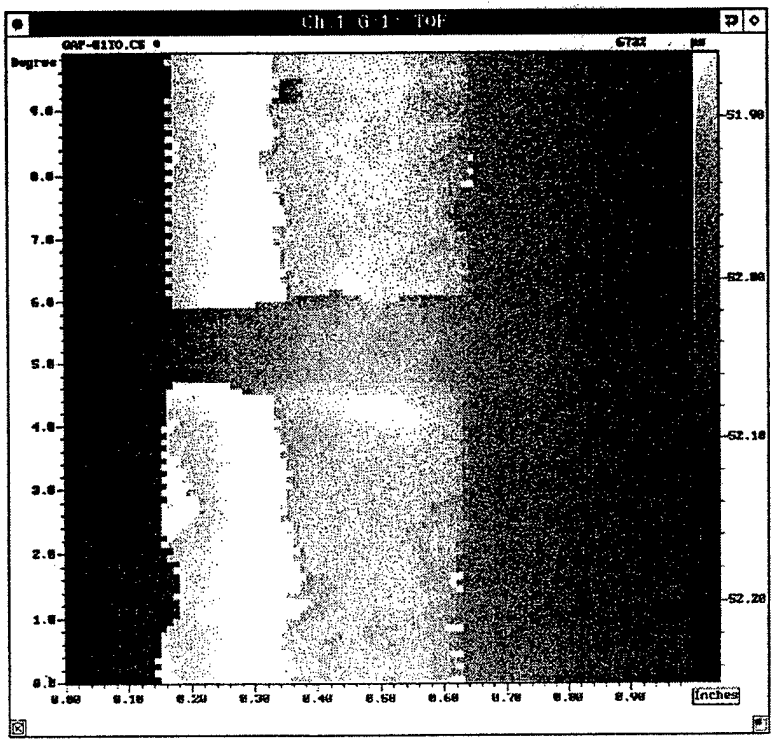

Figure 27. Inherent Impression (TOF)

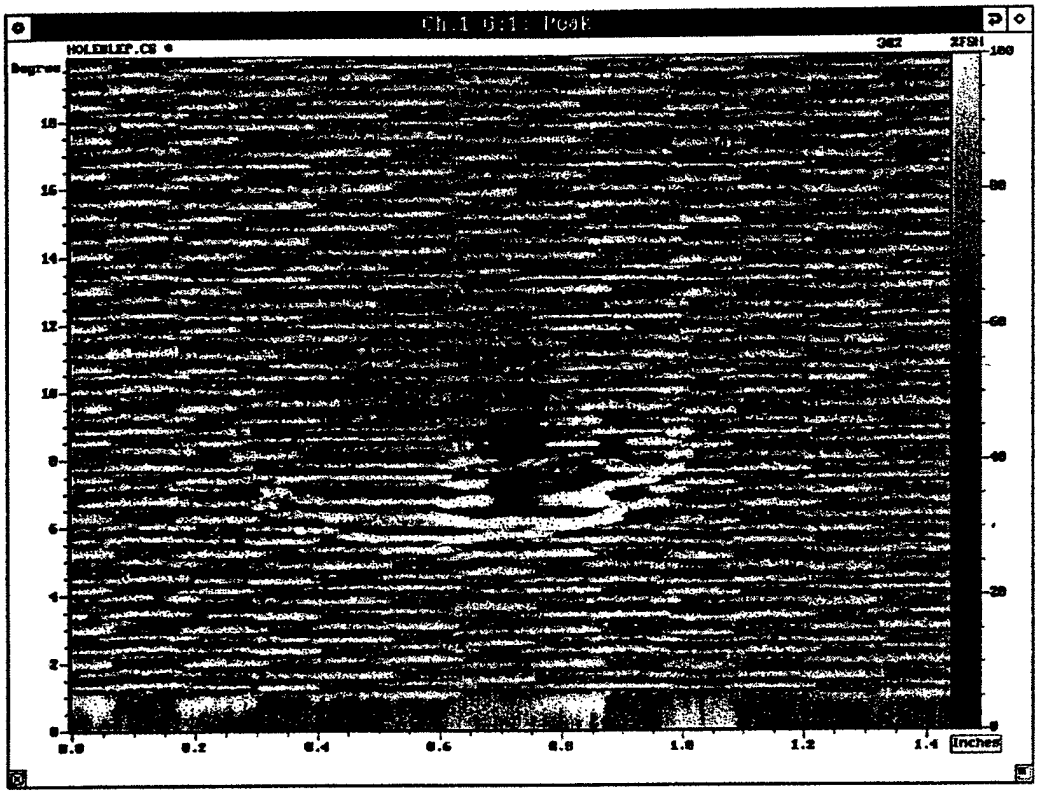

Figure 28. Dent (Peak)

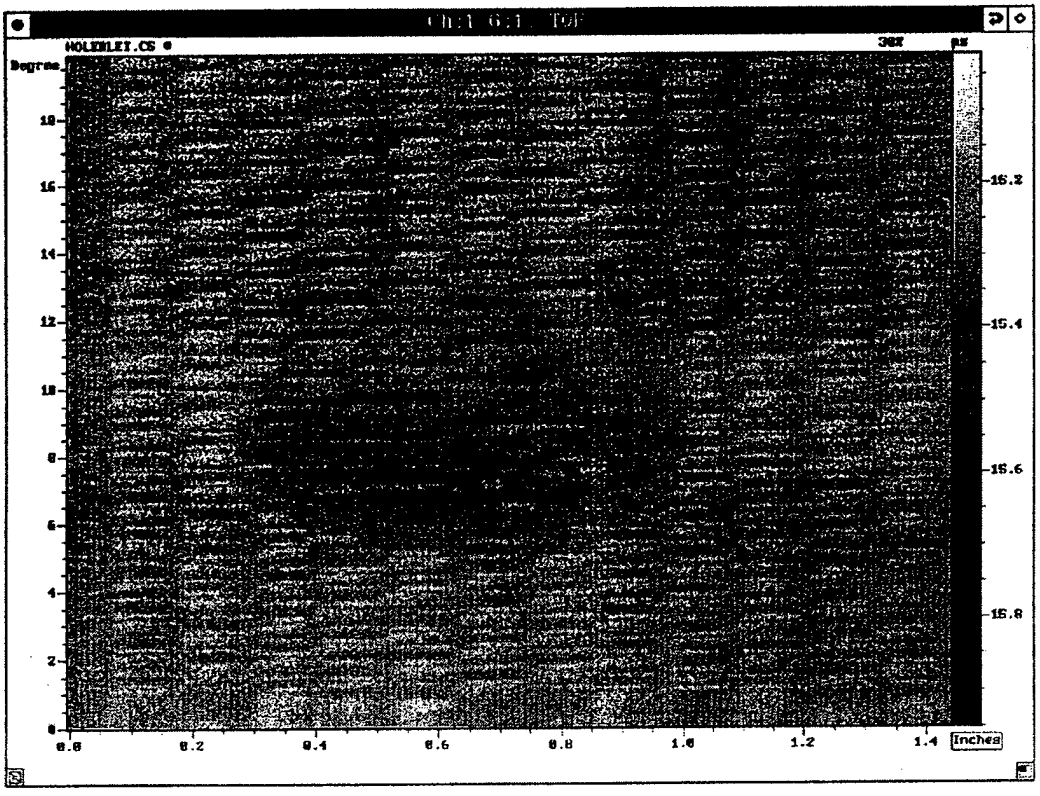

Figure 29. Dent (TOF)

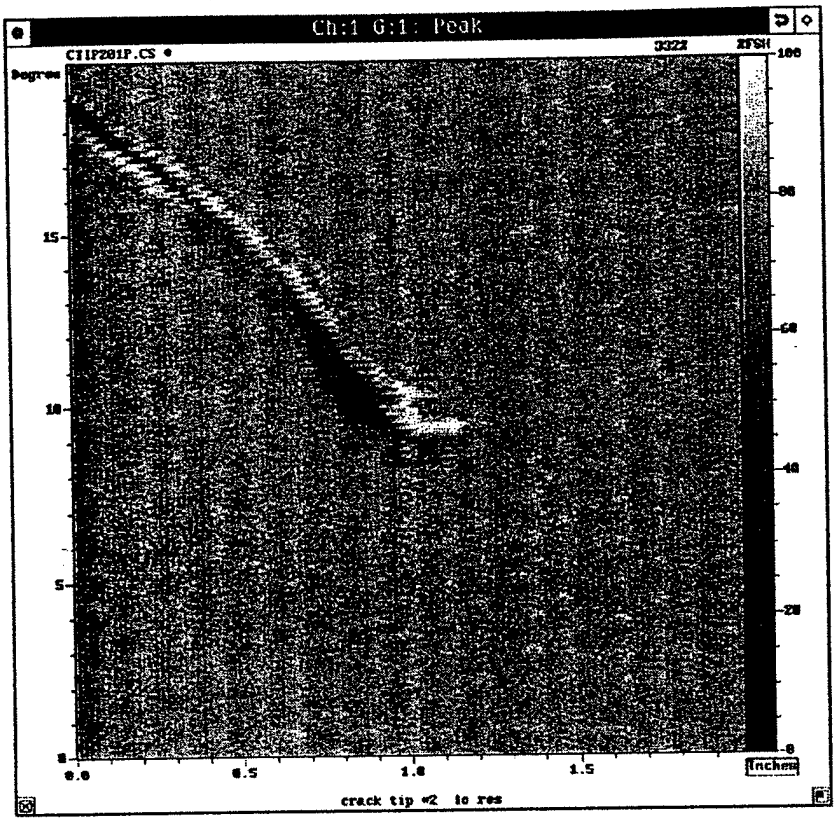

Figure 30. Crack Tip (Peak)

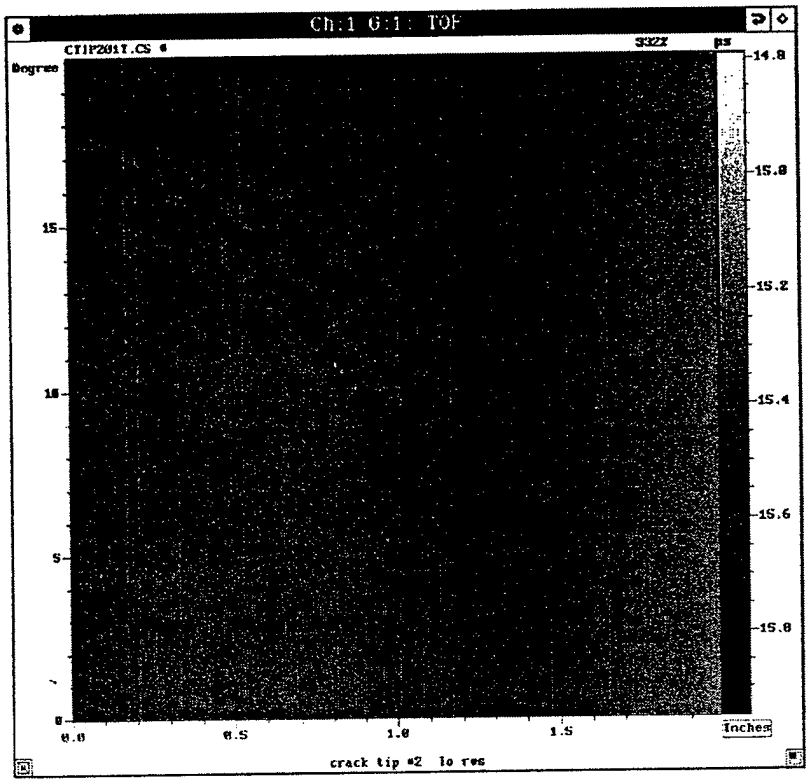

Figure 31. Crack Tip (TOF)

TASK 9. SUGGESTIONS FOR ACCEPT/REJECT CRITERIA

The results in Task 8, summarized earlier and described in detail in Part 2, indicate that the inspection system is capable of detecting different types flaws in ceramic composite radomes. In particular, a map of the radome surface showing porosity induced variations in the ultrasonic characteristics (variations in sound wave velocity or time of flight) can be generated using the inspection system. A procedure, described in Appendix D of Part 2 of the report, allows quantitative assessment of the level of porosity for the Phosphate Bonded Silicon Nitride material used in this study. By the use of results described in Task 2.1, the variation of the dielectric constant over the radome, particularly in areas or patches where it is maximum, can be estimated. Microwave NDE using commercially available rectangular wave guide or co-axial cable type sensors discussed in Task 3 should also be performed for direct quantification of the dielectric constant variation. An accept/reject criterion can be chosen based on some acceptable variation (maximum deviation and the size of patch defect) of porosity and/or dielectric constant. From the results presented in Task 2.2, it appears that a dielectric constant variation of 20% over a single patch of size 4" x 4" in a typical radome (base diameter = 12.88", height = 26.13") may be acceptable provided appropriate corrections are made to account for expected changes in boresight errors and antenna receiving patterns. Alternatively, detailed analytical evaluation of the effect of the patch on radome performance may be performed, if desired, using RACP type codes used in Task 2.2. It should be noted that correlations of analysis results with some experimental measurements of antenna receiving patterns using radomes containing patch type defects are needed before such results are used in practice.

Since materials other than Phosphate Bonded Silicon Nitride are also being considered for next generation radomes and no experimental data are available to establish a quantitative relationship relating the porosity to the ultrasonic characteristics and also the dielectric constant, some relations for dilute concentration of porosity (or its change in a material with constant porosity) given below may be used for decision making purposes. These relations are based on well known results for determining the effective elastic and dielectric constants (Refs. 18, 9) of a composite made of an isotropic material and a dilute concentration of spherical voids (or inclusions). Volume fraction of voids is denoted by V and effective properties are denoted with an asterisk.

Shear Modulus $$\mu^* = \mu\left[1 - V \cdot \frac{15(1-\nu)}{7-5\nu}\right] \quad (2)$$

ν being the Poisson's ratio.

Bulk Modulus (with pores) $$k^* = k\left[1 - V \cdot \frac{3(1-\nu)}{2(1-2\nu)}\right] \quad (3)$$

Bulk Modulus (with pores filled with water treated as rigid inclusions) $$k^* = k\left[1 + V \cdot \frac{3(1-\nu)}{(1+\nu)}\right] \quad (4)$$

Density with pores $$\rho^* = \rho(1-V) \quad (5)$$

Density with pores filled with water $$\rho^* = \rho\left[1 - V\left(1 - \frac{\rho_w}{\rho}\right)\right] \quad (6)$$

ρ_w is the density of water.

The wave velocity of interest, the longitudinal wave velocity in the composite, is given by

$$C_L^* = \left\{\left(k^* + 4\mu^*/3\right)/\rho\right\}^{1/2} \quad (7)$$

Using equations (2) - (7) and neglecting terms with higher powers of V, one obtains the following expressions for changes in the wave velocity due dilute concentration of pores. For pores not filled with water

$$C_L^* = C_L\left[1 - V\left\{\frac{1+\nu}{4(1-2\nu)} + \frac{5(1-2\nu)}{7-5\nu} - \frac{1}{2}\right\}\right] \quad (8)$$

with $\nu = 0.3$

$$C_L^* = C_L[1 - 0.676V] \quad (9)$$

For pores saturated with water after long immersion

$$C_L^* = C_L\left[1 + V\left\{1 - \frac{5(1-2\nu)}{7-5\nu} - \frac{1}{2}\frac{\rho_w}{\rho}\right\}\right] \quad (10)$$

with $\nu = 0.3$ and $\rho_w/\rho = 0.4$

$$C_L^* = C_L[1 - 0.436V] \quad (11)$$

Equations (9) and (11) indicate that for materials with Poisson's ratio and density comparable to those listed before these equations, the wave velocity decreases by 3.4% due to 5% void content, whereas when saturated with water it increases by 2.2%.

It may be noted that the test data for unsaturated PBSN samples with voids, given in Appendix D of Part 2, do not correlate with equation (9), i.e., the change in velocity appears to be much higher than that given by (9). There are two possible reasons for this discrepancy, namely, (i) the pores may not be spherical (it is known (Ref. 19) that for oblate spheroidal pores which are crack like, the effective moduli decrease at a faster rate with V) and (ii) the measured porosity change is that of connected porosity, which may be lower than the total change. Moreover, the pores may contain some solids, which may also reduce the change in the effective densities given by equations (5) and (6). It appears, therefore, that a better estimate may be obtained by neglecting the density change and multiplying the change in the velocity by a factor α, which yield the following estimates. For pores not filled with water

$$C_L^* = C_L\left[1-\alpha V\left\{\frac{1+\nu}{4(1-2\nu)}+\frac{5(1-2\nu)}{7-5\nu}\right\}\right] \tag{8a}$$

For $\nu = 0.3$

$$C_L^* = C_L[1-1.18\alpha v] \tag{9a}$$

For pores saturated with water

$$C_L^* = C_L\left[1-\alpha V\left\{0.5-\frac{5(1-2\nu)}{7-5\nu}\right\}\right] \tag{10a}$$

For $\nu = 0.3$

$$C_L^* = C_L[1+0.14\alpha V] \tag{11a}$$

From the test data given in Part 2, it appears that α in (9a) must be of the order of 4 for PBSN. It may be noted that for oblate (flat) spheroidal pores with aspect ratio of the order of 0.1, the decrease in effective moduli may be three to four times that for spherical pores (Ref. 19).

Equations (8a) and (10a) with $\alpha \approx 4$ can be used to estimate the small variations of porosity (much larger variations will possibly be not acceptable) from ultrasonic characterization, although it may be useful to perform some tests for new material systems (with known porosities) under development, in order to obtain a correct estimate of α.

The changes in the dielectric constant due to small variation of porosity can be estimated from the following equations

$$\varepsilon^* = \varepsilon\left[1 - \frac{V \cdot 3(\varepsilon - \varepsilon_a)}{2\varepsilon + \varepsilon_a}\right] \tag{12}$$

where ε_a = 1.0, the dielectric constant of air. However, since the dielectric solid is sometimes designed to have a constant porosity which may be high (as in PBSN) and the dielectric constant for the solid itself may be quite high, a more accurate expression (Ref. 9) is given by

$$\varepsilon^* = \varepsilon_s\left[1 - \frac{V_t \cdot 3(\varepsilon_s - \varepsilon_a)}{\varepsilon_a + 2\varepsilon_s + V_t(\varepsilon_s - \varepsilon_a)}\right] \tag{13}$$

where

ε_s = the dielectric constant for the solid without any voids

V_t = total void content inclusive of desired one

Equation (13) is an upperbound result for nondilute concentration of spherical voids and has been used in Task 2.1 to estimate the effects of porosity on the dielectric constant. Effects of variations in porosity on the change in the loss tangent of the material can be neglected since the loss is usually small. No estimates are currently available for the effect of the aspect ratio of oblate spheroidal voids on the effective dielectric constant. It is expected, however, if ε (or ε_s) in (12) (or (13)) are not too large these relations should yield a good estimate of the change in ε^*.

Once the variations in the dielectric constant over a radome of next generation material are estimated from ultrasonic characterization, it would be worthwhile to use microwave NDE for obtaining a direct quantification and correlation. No detailed microwave evaluations of the PBSN material were performed in this program, but commercially available probes, such as the Hewlett Packard 85070A and the 8722C vector network analyzer may be utilized, as discussed in Task 3 and Ref. 16. Based on the estimated changes in the dielectric constant, a decision regarding the acceptance of a radome can be made, if some limits are chosen in the dielectric property variation as described earlier. Analytical evaluation of the electromagnetic performance of radome can also be made to determine the acceptability of a radome.

Effects of porosity and/or surface crack type defects on stiffness, strength and thermal expansion characteristics can be estimated using the methods and results given in Task 2.1. However, dilute concentration of additional porosity over the desired value and small crack like defects (sizes less than those described in Task 2.1) are not expected to have any significant influence on thermomechanical properties of the material.

CONCLUDING REMARKS

Optical reflection/transmission measurements used for nondestructive evaluation of currently used radomes are not suitable for use with next generation ceramic composite radomes, since these materials do not allow light transmission. Ultrasonic characterization has been found to be a useful tool for quantification of porosity variations and other defects, such as crack like defects. Variation in porosity and/or reinforcements is the dominant anomaly in ceramic matrix radomes and it influences the dielectric property of the material, which in turn changes the electromagnetic performance of the radome. An inspection system for interrogation of radome shaped shells has been developed. The system can accommodate radomes of various sizes and has been shown to generate a map of property variations (especially the change in porosity) using ultrasonic probes. Methods of estimating porosity variation from ultrasonic characteristics and the changes in the dielectric constant from those in porosity, which can be used for next generation ceramic composites, are described. Approaches for selecting accept/reject criteria based on the results of inspection are suggested, which should be examined in conjunction with some trial experiments and correlation of test results with analytical evaluation of the electromagnetic performance of radomes made with intentional porosity variations over a patch. The RACP code has been modified for analytical evaluation.

The inspection system can also make use of microwave probes, although a demonstration of such imaging could not be performed on full scale radomes. Microwave probes can yield a direct measure of dielectric property changes and was used for some small samples. However, edge effects influence the image for small samples since the probes are usually of moderate sizes. Such edge effects are not expected in imaging of full scale radomes. Therefore, microwave imaging of radomes using the inspection system should be attempted in the future. However, microwave probes need a conducting flange and a customized design of the flange may be required for the curvature in radomes. Attempts were made for analytical evaluation of unavoidable air gaps between the flange and the sample being interrogated (due to surface roughness and/or curvature) as well as other parameters (such as interrogation frequency) on expected signals and the results are discussed.

Attempts are being made to contact some manufacturers of next generation radomes and to determine their interest in the inspection system developed in the program.

REFERENCES

1. Proceedings of the First DOD Electromagnetic Windows Symposium, Vol. I, NSWC, October, 1985
2. Talmy, I.G., and Haught, D.A., "Celsian-Based Ceramics as Candidates for Radomes", in Proceedings of the Fourteenth Conference Metal Matrix, Carbon, and Ceramic Matrix Composites", Cocoa Beach, FL, January 17-19, 1990.
3. Ho, W., "High Temperature Dielectric Property Testing of Sensor Window Materials", Rockwell Report for SURFMAT Program, NSWC, May, 1986.
4. Zaykoski, J., and Talmy, I.G., "Toughening of Celsian Ceramics", in Proceedings of the Fourteenth Conference Metal Matrix, Carbon, and Ceramic Matrix Composites", Cocoa Beach, FL, January 17-19, 1990.
5. Sheppard, L.M., "Evolution of NDE Continues for Ceramics", Ceramic Bulletin, Vol. 70, p. 1265, 1991.
6. Anon., 1991 Annual Report, Center for Nondestructive Evaluation, Johns Hopkins University, Baltimore, MD, 1991.
7. Proceedings of the 1991 ASNT Spring Conference, Nondestructive Characterization for Advanced Technologies, Oakland, CA, 1991.
8. Yen, C.F., Chatterjee, S.N., Duke, J.C., Jr., and Horne, M.R., "Nondestructive Evaluation of Reinforced Ceramics for Radomes, Parts 1 and 2, MSC TFR 3301/1436, NSWC Contract No. N60921-92-C-0126, January, 1993.
9. Hashin, Z., and Shtrikman, S., "Journal of Applied Physics, Vol. 33, p. 3125, 1962.
10. Talmy, I.G., Martin, C.A., Haught, D.A., Le, A.H., and Janorsky, A.E., "Development of Phosphate-Bonded Silicon Nitride Ceramics and Ceramic Matrix Composites", Technical Digest, p. 16, September, 1993.
11. User's Manual for RACP™, Radome Analysis Computer Program, Scientific Software, Maitland, FL.
12. Bakhtiari, S., "Open-Ended Sensors for Microwave Nondestructive Evaluation of Layered Composite Media", Ph.D. Dissertation, Department of Electrical Engineering, Colorado State University, Fort Collins, CO, 1992.

13. Bakhtiari, S., Ganchev, S.I., and Zoughi, R., "Microwave Swept-Frequency Optimization for Accurate Thickness on Dielectric Property Monitoring of Conductor-Backed Composites", Materials Evaluation, p. 740, June, 1993.
14. Bakhtiari, S., Ganchev, S.I., and Zoughi, R., "Analysis of Radiation from an Open Ended Co-Axial Line into Stratified Dielectrics", IEEE Transactions on Microwave Theory and Techniques, Vol. 42, No. 7, p. 126, July 1994.
15. Li, C., and Chen, K.M., "Determination of Electromagnetic Properties of Materials Using Flanged - Open Ended Co-Axial Probe - Full Wave Analysis", IEEE Transaction on Instrumentation and Measurement, Vol. 44, No. 1, p. 19, February, 1995.
16. Liu, J.M., "Electrical Characterization of Fiber Reinforced Composites for Mast and radome Applications", CARDIVNSWC-TR-95/028, October 1, 1995.
17. User's Manual 85070A, Dielectric Probe Kit, Hewlett Packard Corp., 1991.
18. Christensen, R.M., Mechanics of Composite Materials, John Wiley & Sons, New York, 1979.
19. Norris, A.N., "Effects of Pore Shapes on Low Frequency Wave Speeds in Porous Media", in Review of Progress in QNDE, Vol. 5B, Plenum Press, New York, 1986.
20. Reference Library for RACP™, Radome Analysis Computer Program, Scientific Software, Maitland, FL.

APPENDIX A

EFFECTS OF PATCH DEFECTS ON RADOME PERFORMANCE

Suite 250, 500 Office Center Drive
Fort Washington, PA 19034
Tel: 215-542-8400 Fax: 215-542-8401

INTRODUCTION

The RACP™ code is quite versatile and allows evaluation of boresight errors for different types of radomes with variable thickness and properties as well as monopulse antenna near fields (receiving patterns) for various polarizations of the incident plane wave and the antenna. However, in its present form the code does not allow consideration of a patch type defect in the radome (Figure A1). The code was, therefore, modified to consider such property variations over a region bounded by two prescribed axial coordinates (z) and circumferential coordinates (ϕ) as shown in Figure A2. Since it is expected that the property change will be maximum at the center of the patch and will reduce to zero at its boundaries, it is assumed that the property change (real and imaginary part of the dielectric constant or thickness) is of the following form

$$\Delta = \Delta_o \cos\frac{\pi(z - z_1)}{\ell}\cos\frac{\pi(\phi - \phi_1)}{\theta} \qquad \text{(A-1)}$$

where z_1 and ϕ_1 are the coordinates of the center of the patch and ℓ and θ quantify its dimension in axial and circumferential direction. It may be noted that ϕ_1 defines the relative angular position of the patch with respect to the antenna. $\phi_1 = 90°$ when an axial plane (through radome z-axis) passing through the center of the patch coincides with the azimuth plane ($x_A z_A$) of the antenna (Figure A2). For $\phi_1 = 0°$, the axial plane coincides with $y_A z_A$ or elevation plane of the antenna (Figure A2).

An illustrative example and some results are given in pages A3-A18.

The changes in input data for RACP™ required to analyze the effects of patch defects are described in pages A19-A24.

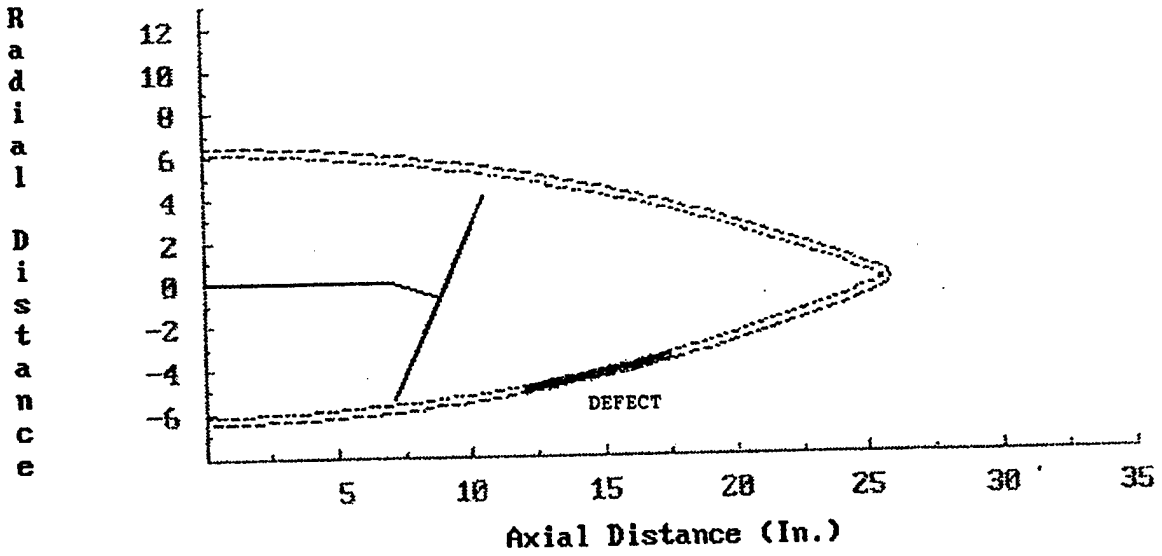

Figure A1. Radome with a Patch Defect, p. 8x

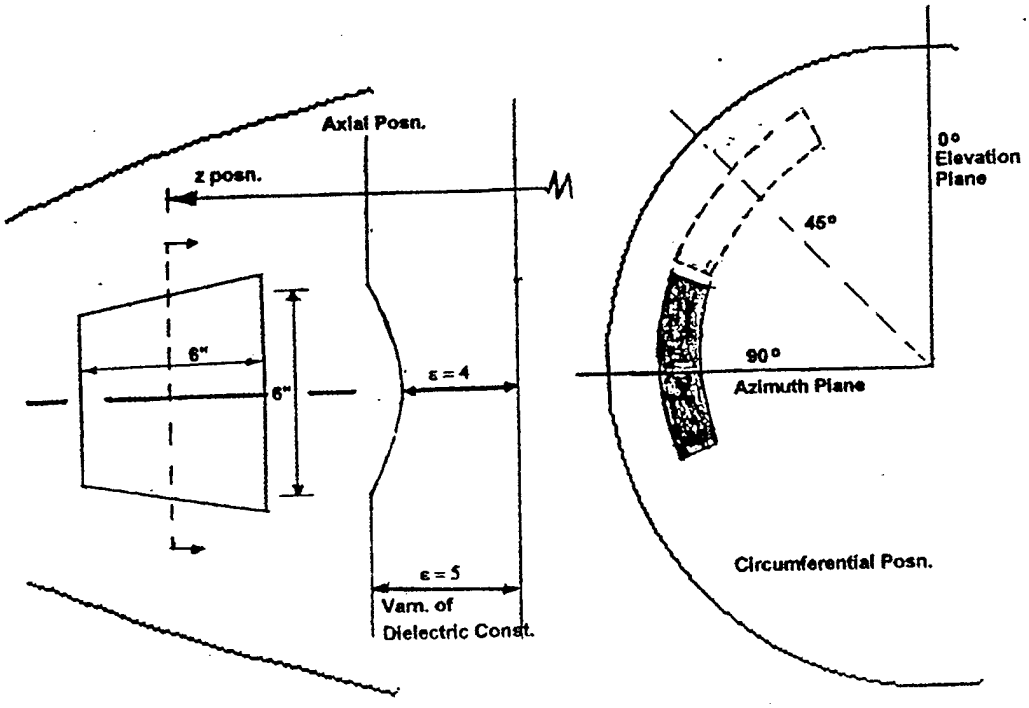

Figure A2. Dielectric Property Validation and Position of the Patch, p.8y

AN ILLUSTRATIVE EXAMPLE

A typical tangent ogive radome shown with the antenna in Figure A1 was considered for demonstration purposes. The following geometric and material properties were used (Figure A3).

Radome base diameter, D_{OS} = 12.88 inch
Radome length, L_{OS} = 26.43 inch
Bulkhead z coordinate, z_{BOT} = 0.0 inch
Antenna Aperture Radius, R_{ap} = 5.0 inch
Gimbal point from radome base, R_R = 7.057 inch
Antenna aperture offset from gimbal, R_A = 1.908 inch
Frequency, F = 11.803 GHZ
Radome wall thickness, DIN = 0.351 inch
Dielectric constant ε_r, ER = 5.0
Loss tangent, TD = 0.03

For estimation of changes in boresight errors due to the patch, the dielectric constant, ε_r, at center was assumed to be 4.0 (Figure A2). For estimation of changes in receiving patterns one more value of ε_r at the center of the patch (ε_r = 2.0) was also selected.

Variations of boresight errors, error slopes and relative antenna gain with yaw gimbal angle for different patch sizes (at an axial position z_1 = 15" and circumferential position ϕ_1 = 90°), when the antenna and the incident wave are both vertically polarized, are shown in Figures A4 - A8. Variations of the same quantities with pitch gimbal angle are plotted in Figures A9 - A13. It may be noted that the elevation errors (and slopes) are zero (Figures A4 and A6) for this case. Also, the azimuth error increases with increasing patch size for positive yaw gimbal angles (z_A of antenna moves towards the patch).

Effects of angular position (ϕ =0 to 90°) for a 6" patch, when the antenna is right hand circularly polarized and the incident wave is vertically polarized, are shown in Figures A14 - A23. Boresight elevation errors (and slopes) are not zero (Figures A14 and A16) in this case.

Computed amplitude and phase of the antenna receiving patterns at elevation and azimuth cuts for a 6" patch defect (with ε_r = 4.0 and 2.0 at the center) located at axial position z_1 = 15" and circumferential position ϕ_1 = 90° for one value of the yaw gimbal angle (= 10°) are shown in Figures A24 - A31.

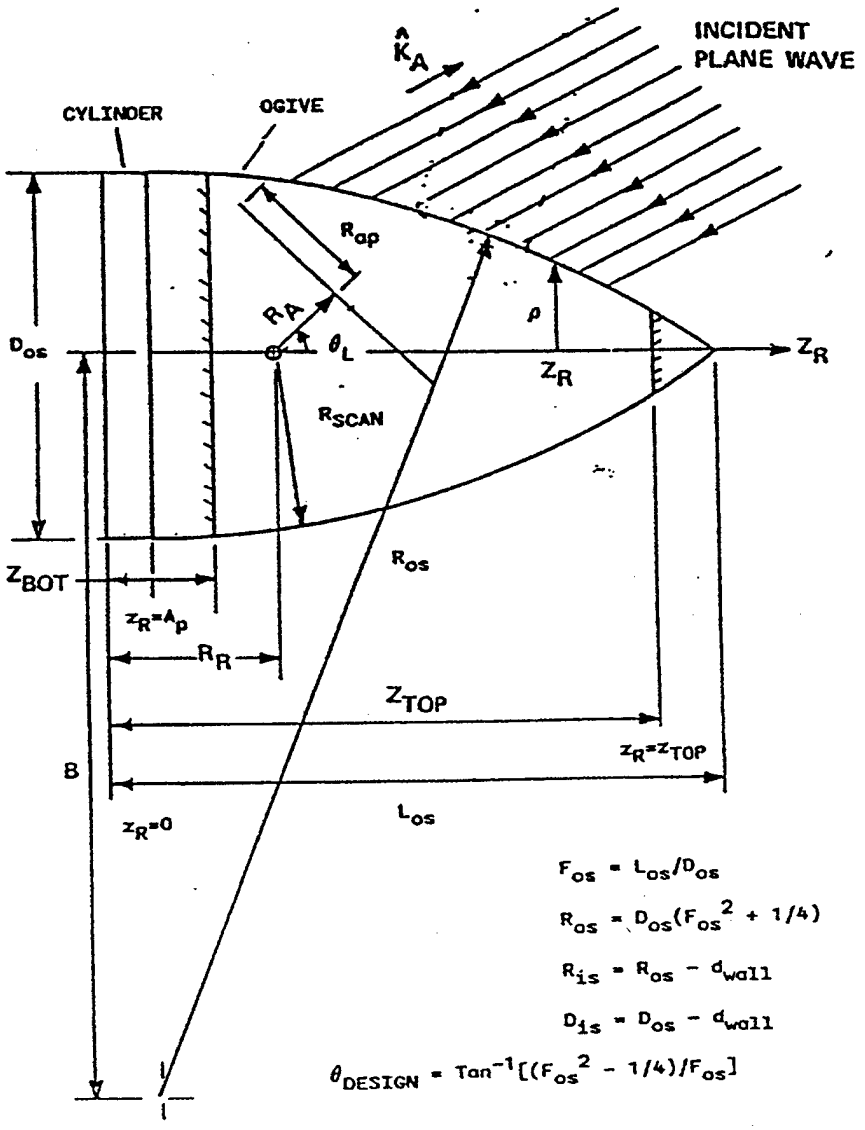

Figure A3. Geometry and Dimensions of Radome and Antenna

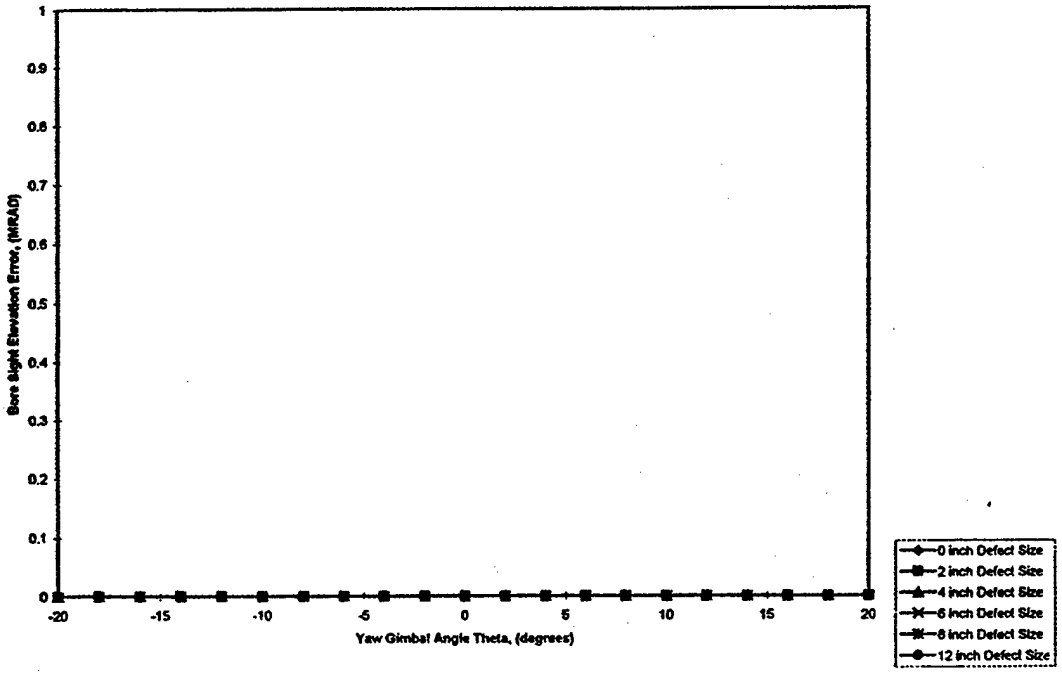

Figure A4. Effect of Defect Size at 90 Degree Position and z=15 in. on Bore Sight Elevation Error for Vertically Polarized Antenna and Incident Wave

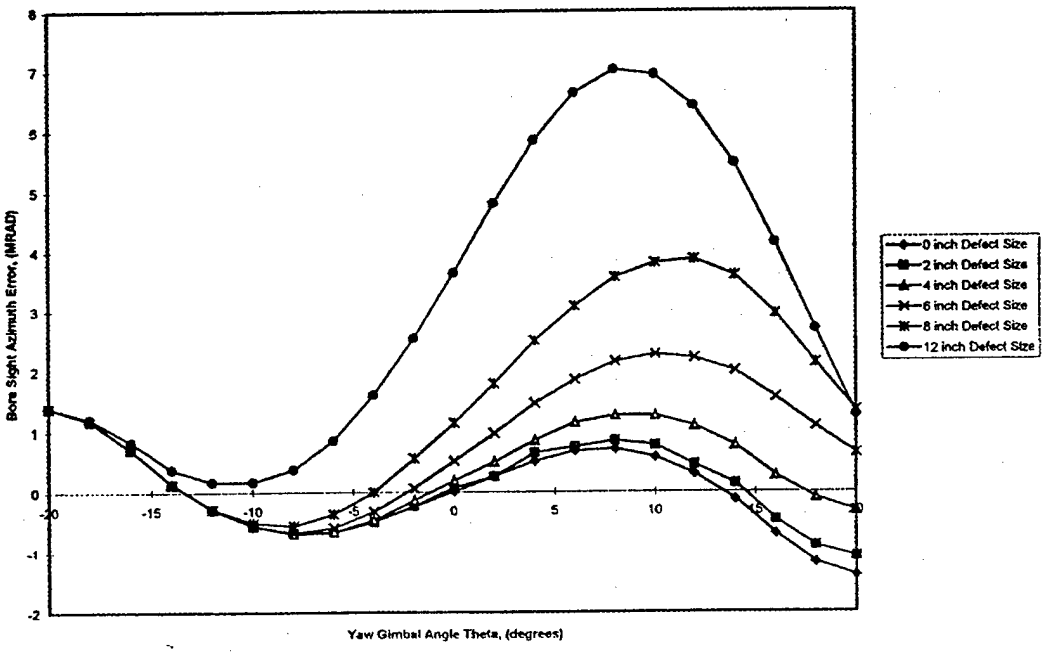

Figure A5. Effect of Defect Size at 90 Degree Position and z=15 in. on Bore Sight Azimuth Error for Vertically Polarized Antenna and Incident Wave

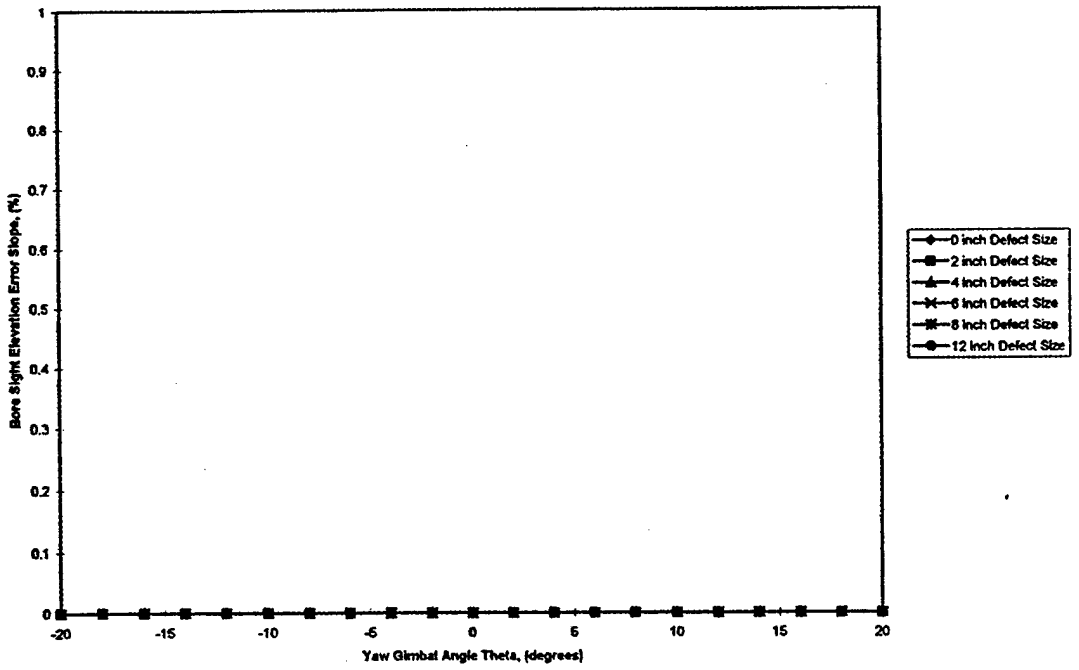

Figure A6. Effect of Defect Size at 90 Degree Position and z=15 in. on Bore Sight Elevation Error Slope for Vertically Polarized Antenna and Incident Wave

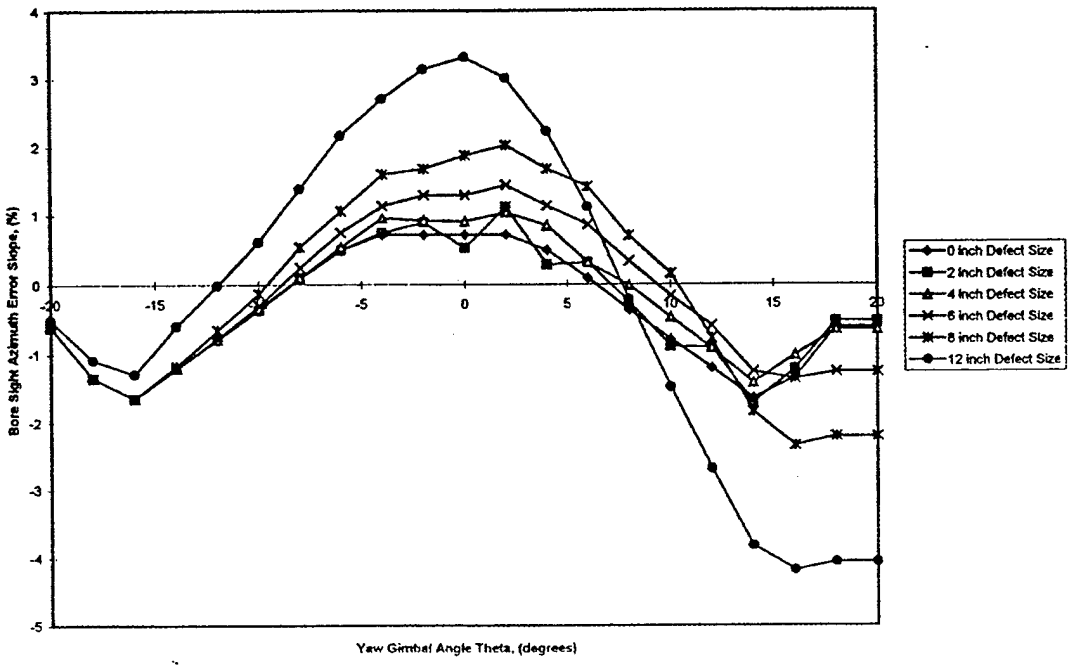

Figure A7. Effect of Defect Size at 90 Degree Position and z=15 in. on Bore Sight Azimuth Error Slope for Vertically Polarized Antenna and Incident Wave

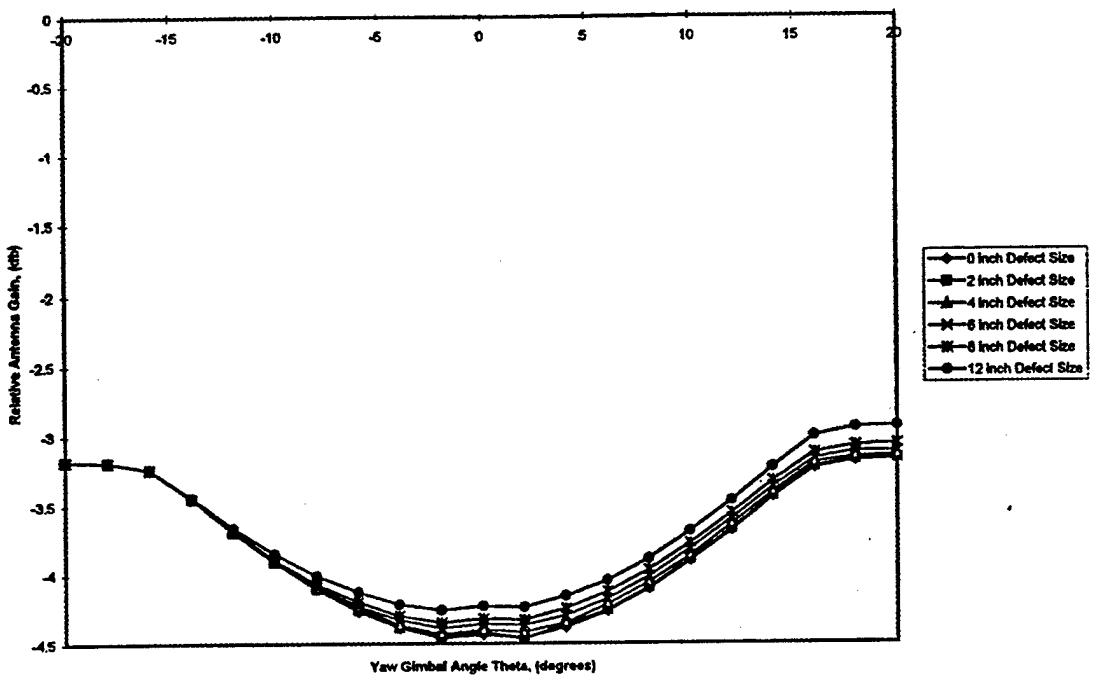

Figure A8. Effect of Defect Size at 90 Degree Position and z = 15 in. on Relative Antenna Gain for Vertically Polarized Antenna and Incident Wave

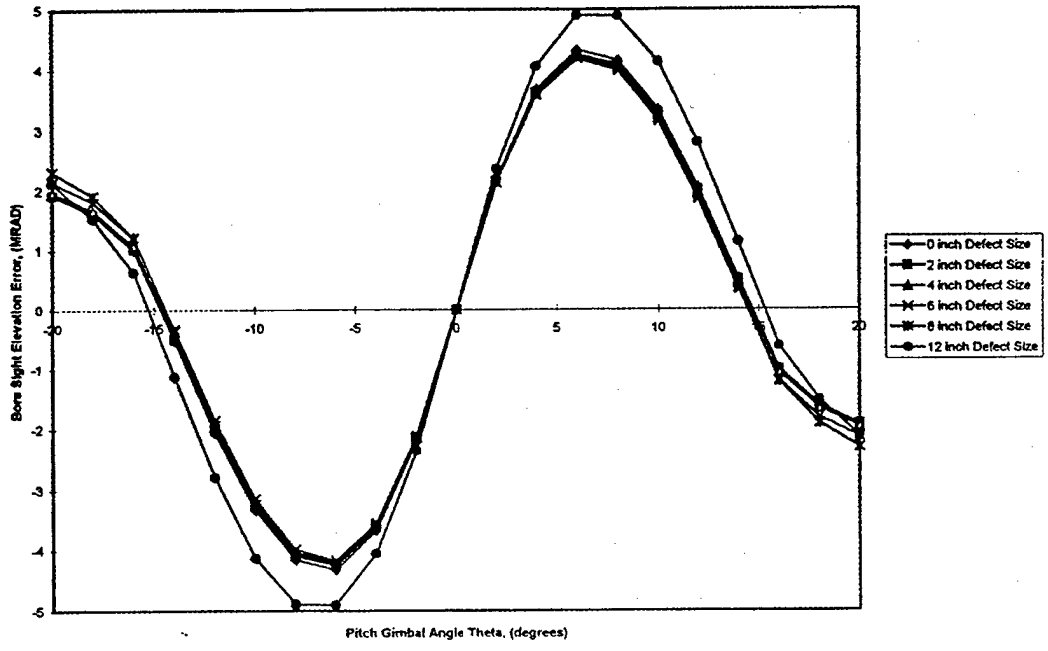

Figure A9. Effect of Defect Size at 90 Degree Position and z = 15 in. on Bore Sight Elevation Error for Vertically Polarized Antenna and Incident Wave

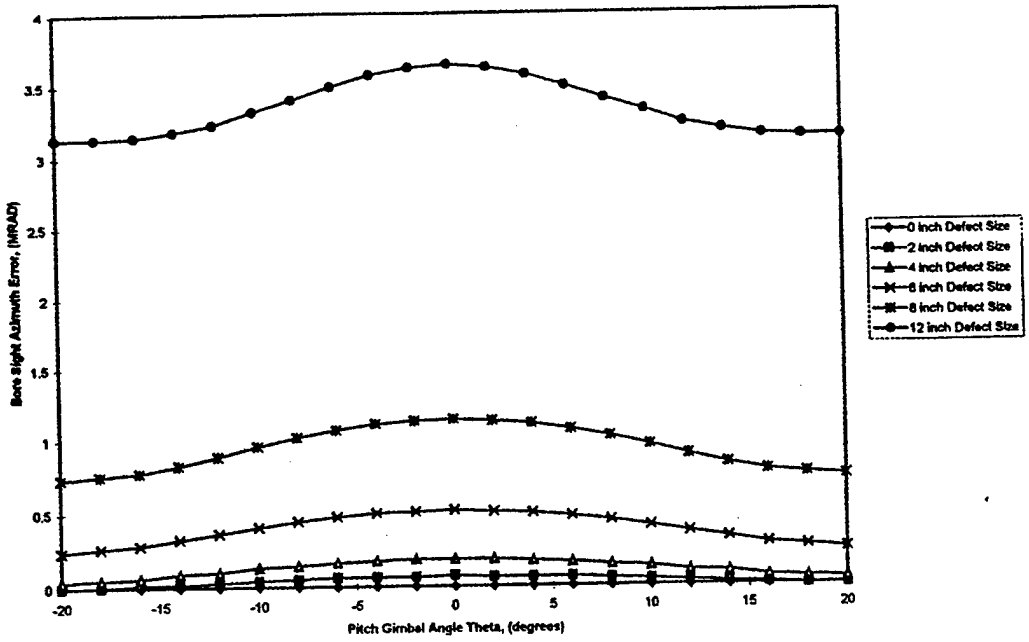

Figure A10. Effect of Defect Size at 90 Degree Position and z = 15 in. on Bore Sight Azimuth Error for Vertically Polarized Antenna and Incident Wave

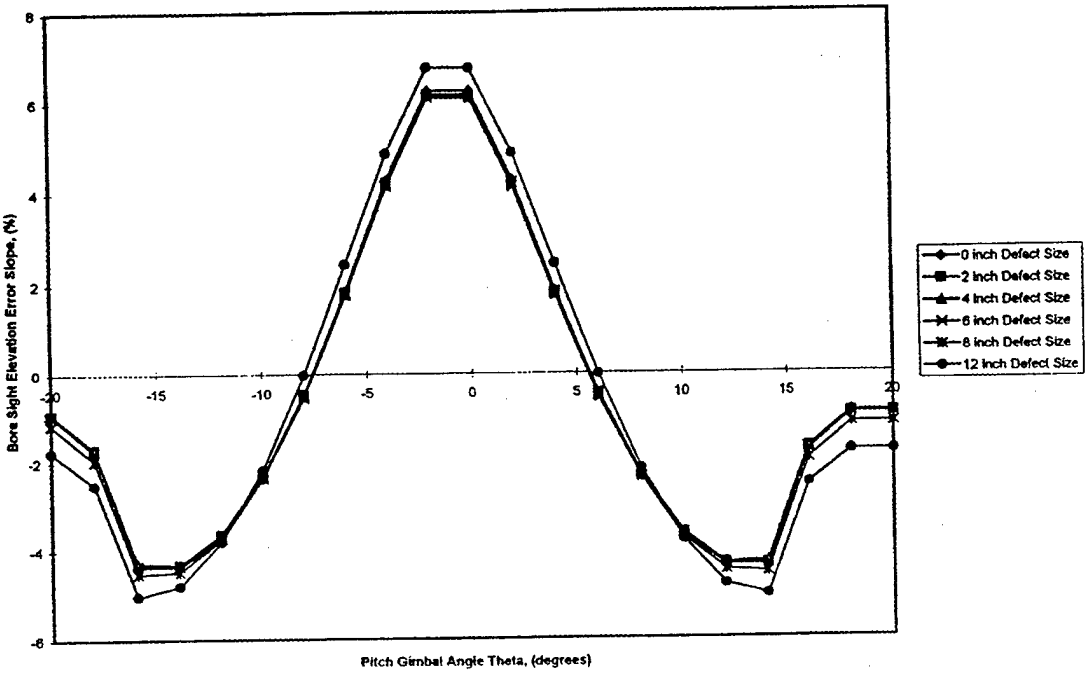

Figure A11. Effect of Defect Size at 90 Degree Position and z = 15 in. on Bore Sight Elevation Error Slope for Vertically Polarized Antenna and Incident Wave

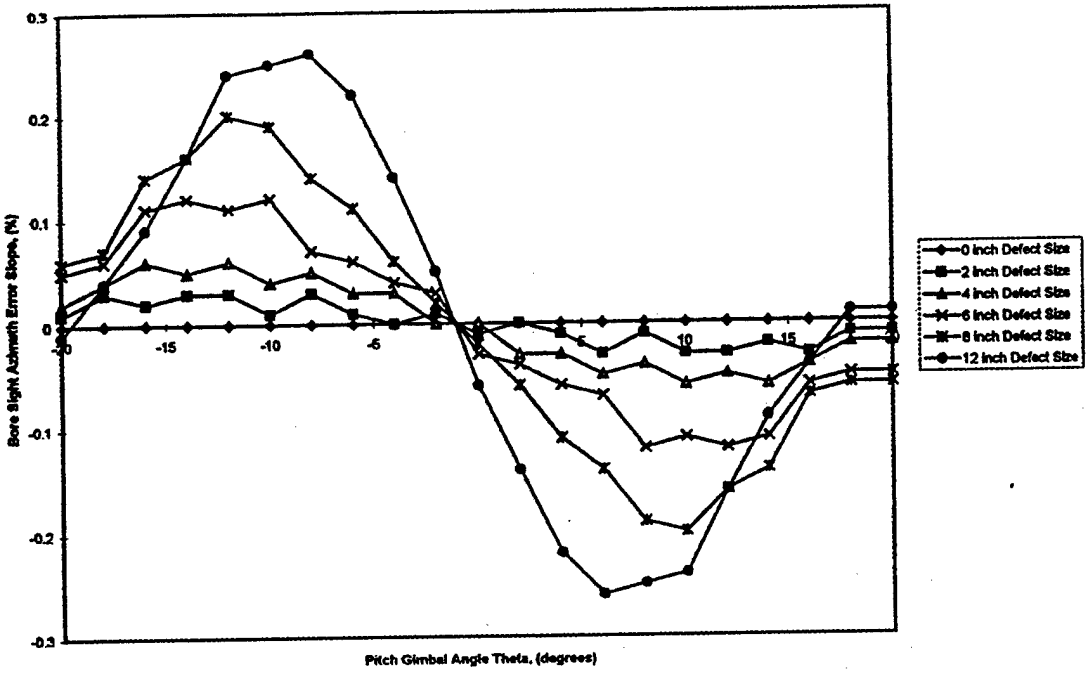

Figure A12. Effect of Defect Size at 90 Degree Position and z=15 in. on Bore Sight Azimuth Error Slope for Vertically Polarized Antenna and Incident Wave

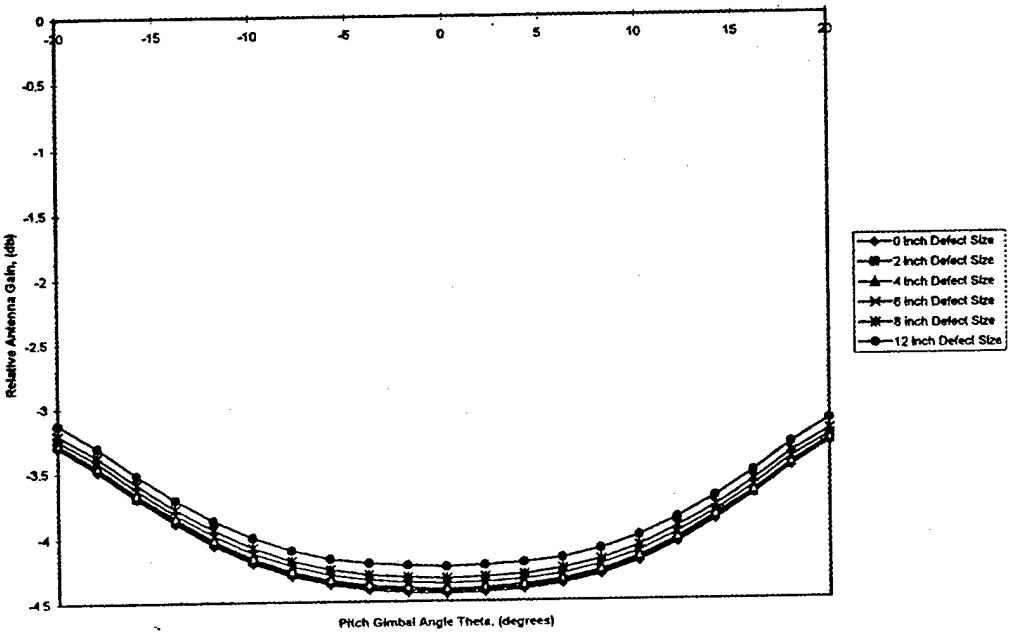

Figure A13. Effect of Defect Size at 90 Degree Position and z=15 in. on Relative Antenna Gain for Vertically Polarized Antenna and Incident Wave

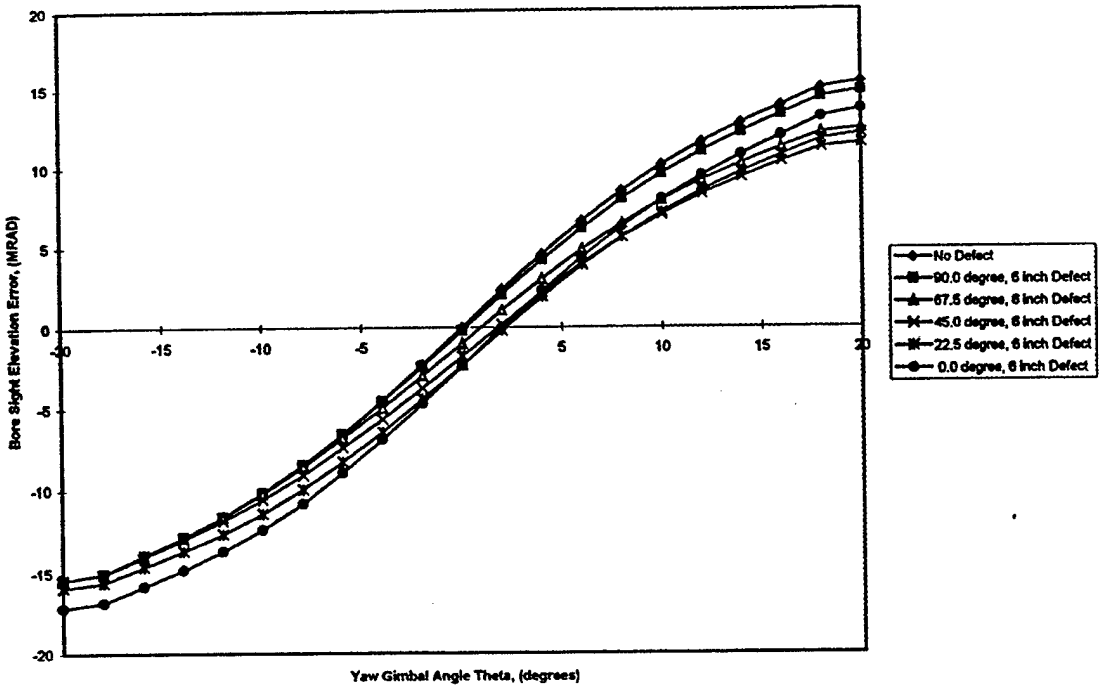

Figure A14. Effect of Angular Position of 6 in. Defect at z = 15 in. on Bore Sight Elevation Error for RHC Polarized Antenna and Vertically Polarized Incident Wave

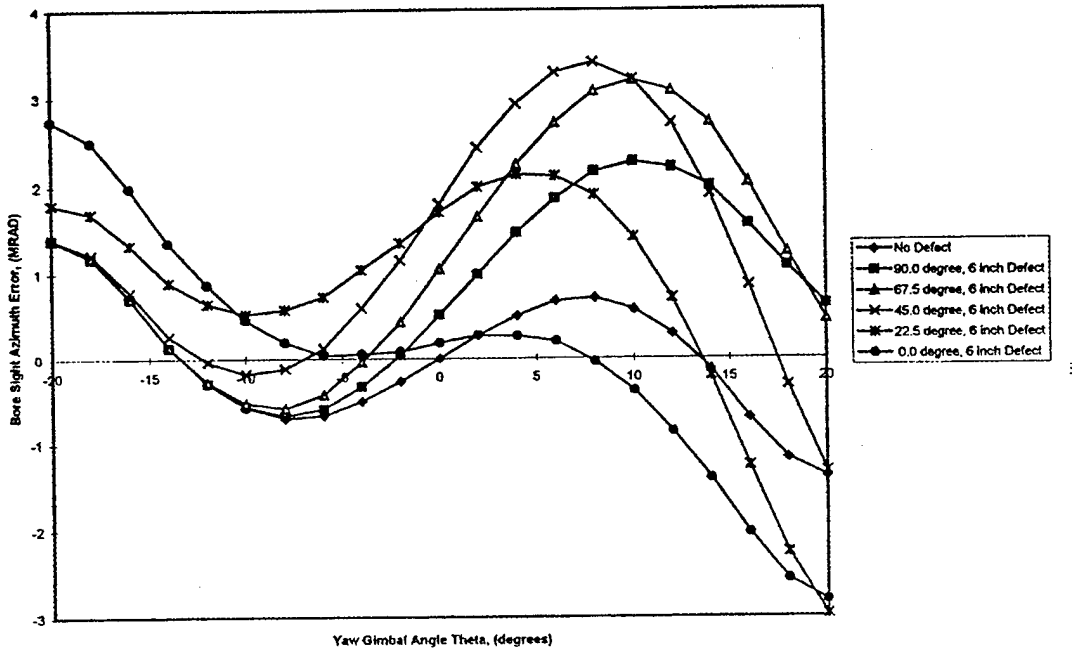

Figure A15. Effect of Angular Position of 6 in. Defect at z = 15 in. on Bore Sight Azimuth Error for RHC Polarized Antenna and Vertically Polarized Incident Wave

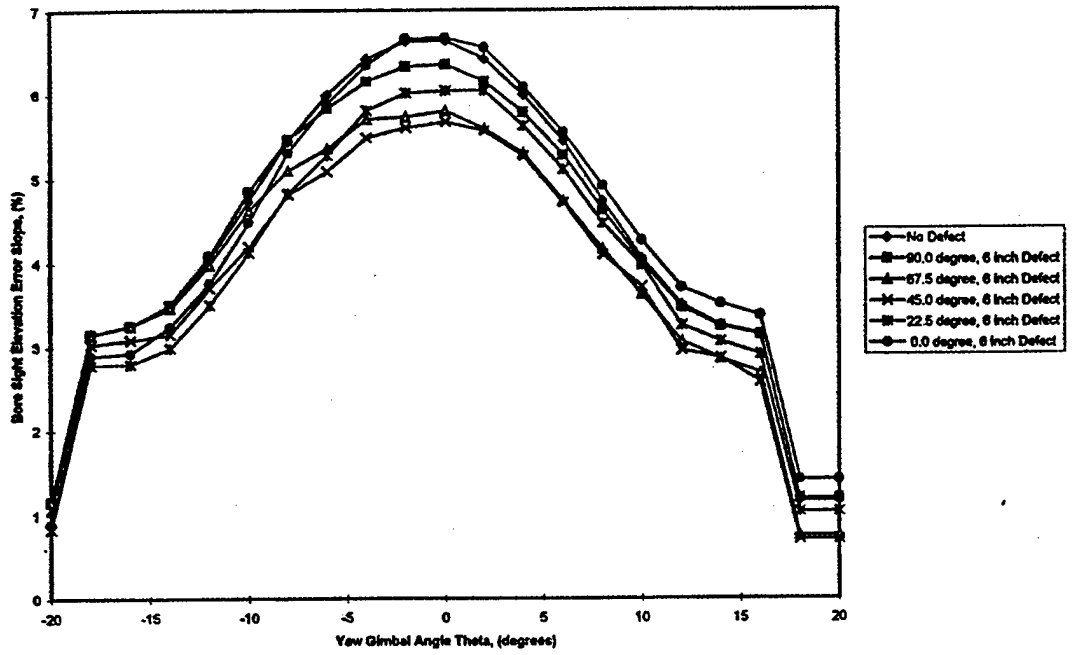

Figure A16. Effect of Angular Position of 6 in. Defect at z = 15 in. on Bore Sight Elevation Error Slope for RHC Polarized Antenna and Vertically Polarized Incident Wave

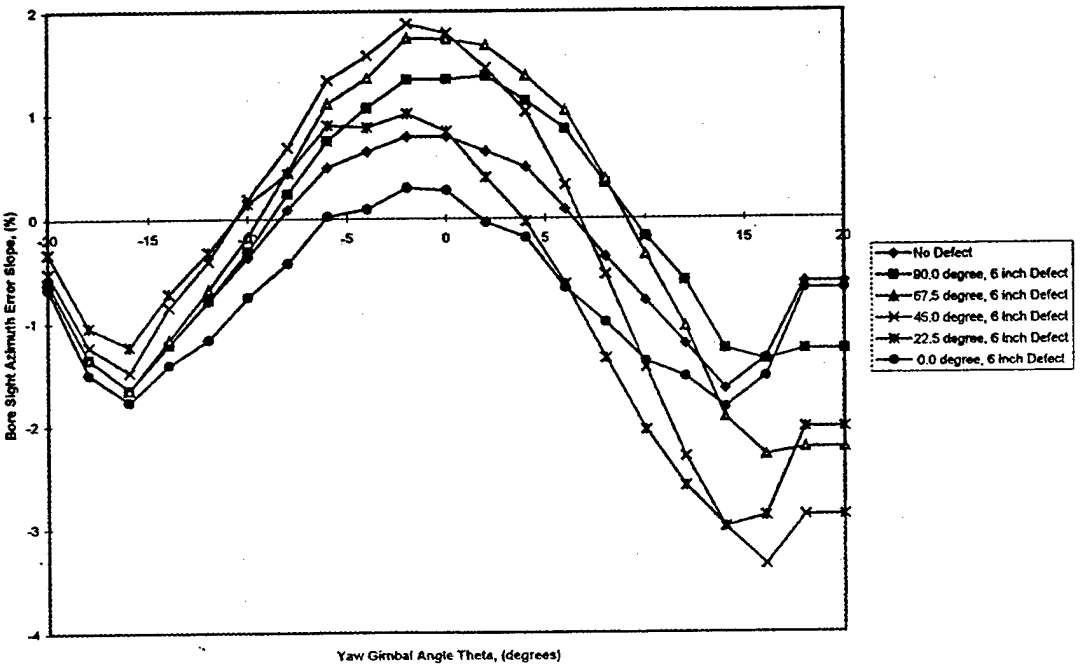

Figure A17. Effect of Angular Position of 6 in. Defect at z = 15 in. on Bore Sight Azimuth Error Slope for RHC Polarized Antenna and Vertically Polarized Incident Wave

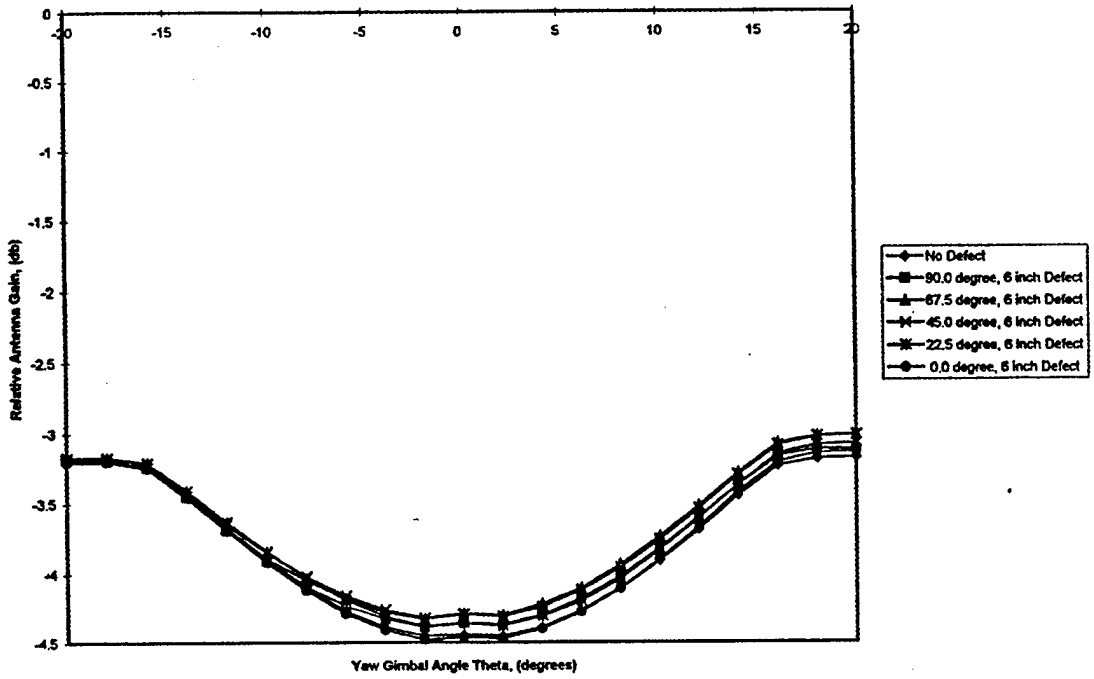

Figure A18. Effect of Angular Position of 6 in. Defect at z=15 in. on Relative Antenna Gain for RHC Polarized Antenna and Vertically Polarized Incident Wave

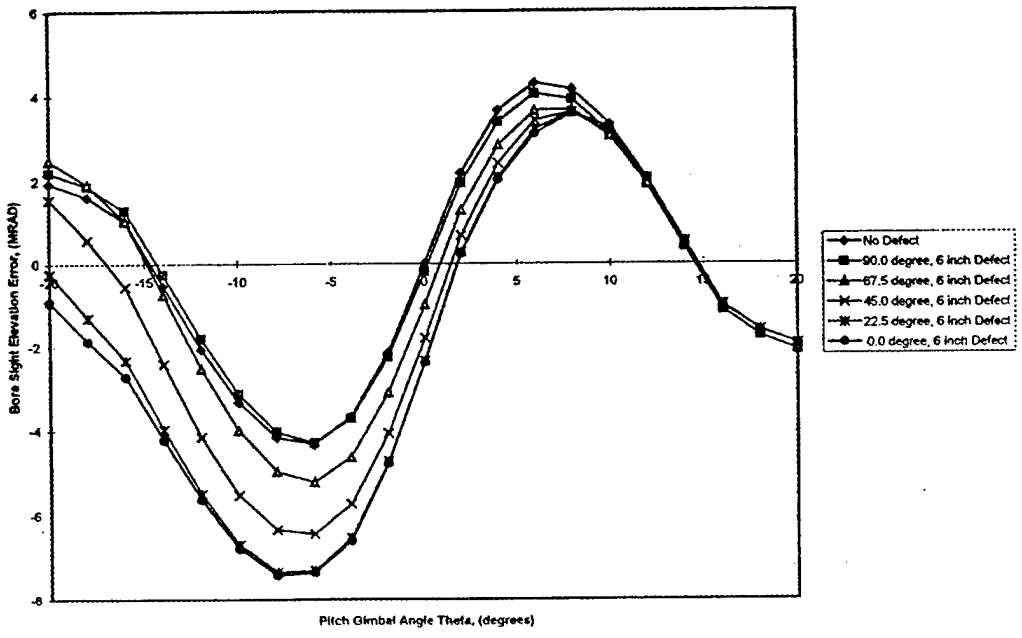

Figure A19. Effect of Angular Position of 6 in. Defect at z=15 in. on Bore Sight Elevation Error for RHC Polarized Antenna and Vertically Polarized Incident Wave

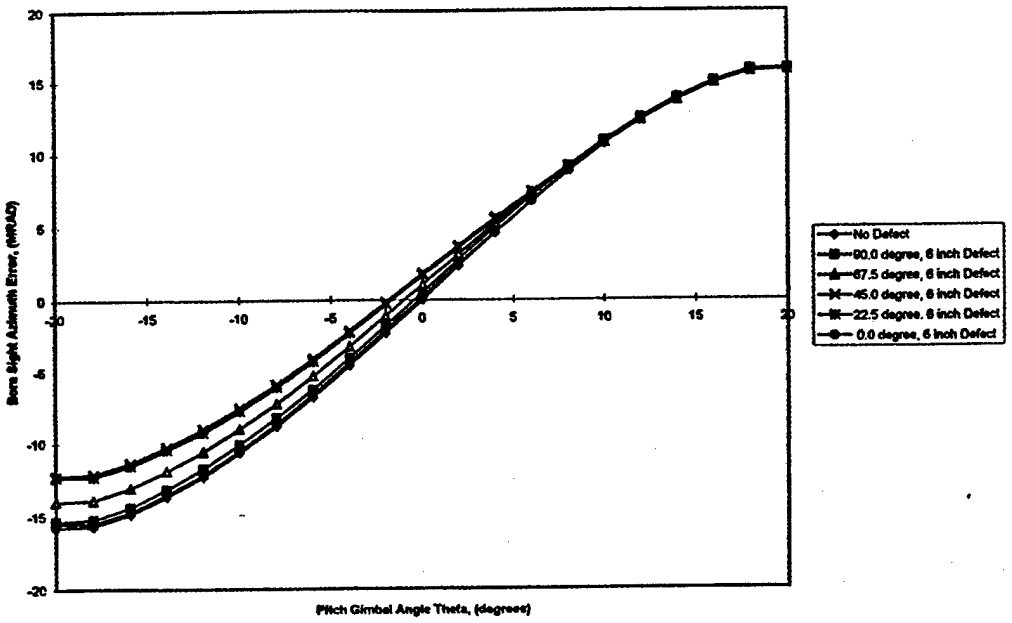

Figure A20. Effect of Angular Position of 6 in. Defect at z = 15 in. on Bore Sight Azimuth Error for RHC Polarized Antenna and Vertically Polarized Incident Wave

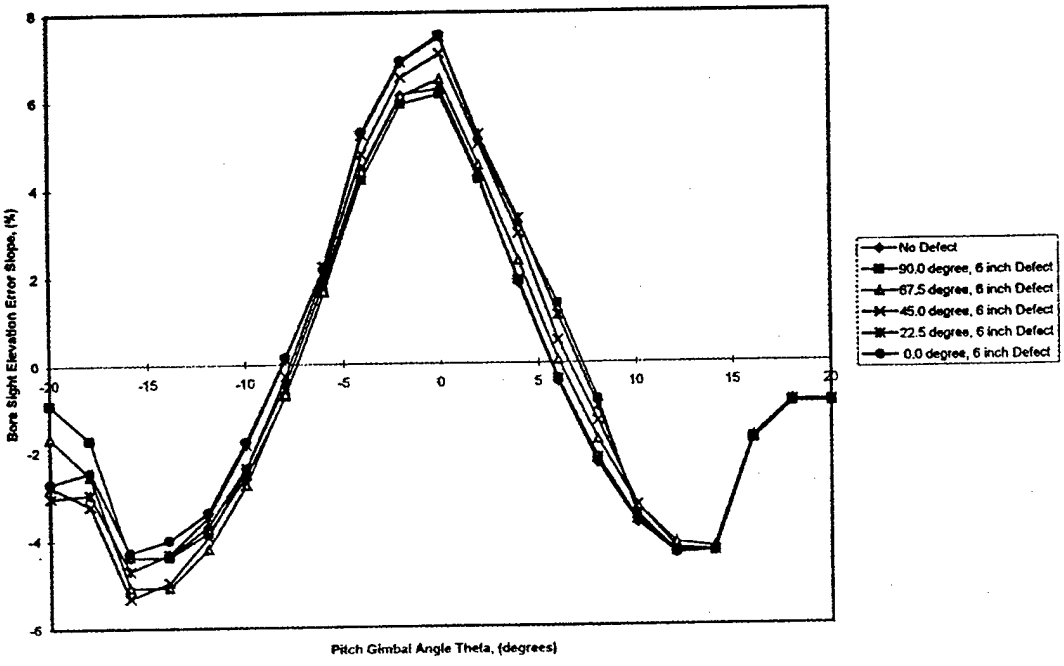

Figure A21. Effect of Angular Position of 6 in. Defect at z = 15 in. on Bore Sight Elevation Error Slope for RHC Polarized Antenna and Vertically Polarized Incident Wave

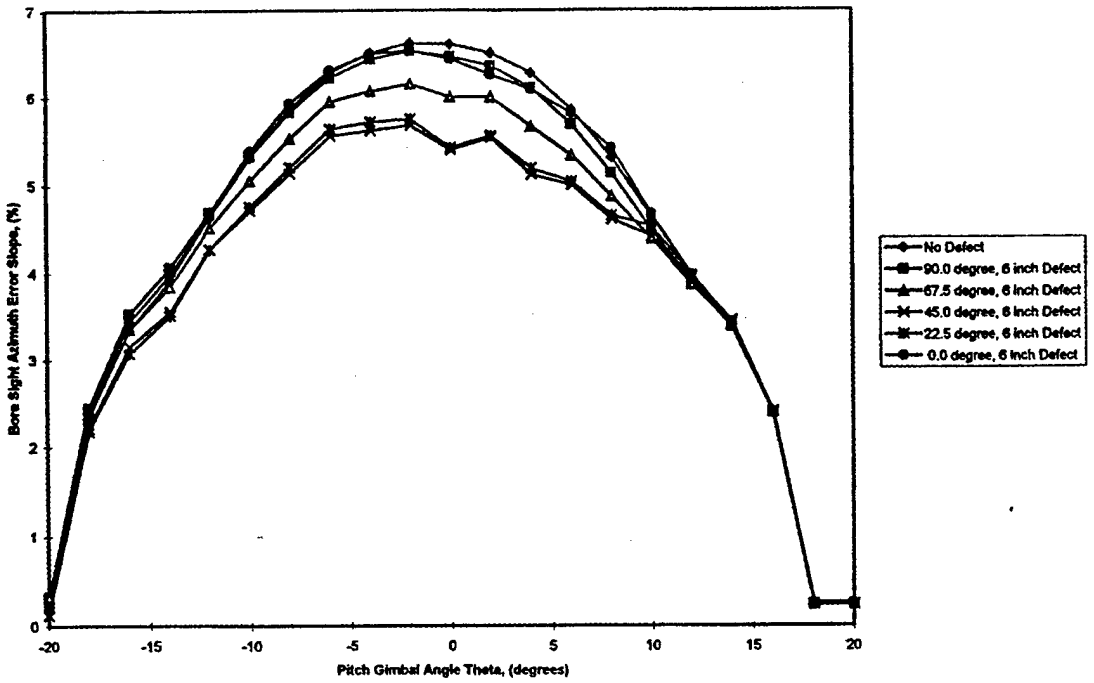

Figure A22. Effect of Angular Position of 6 in. Defect at z = 15 in. on Bore Sight Azimuth Error Slope for RHC Polarized Antenna and Vertically Polarized Incident Wave

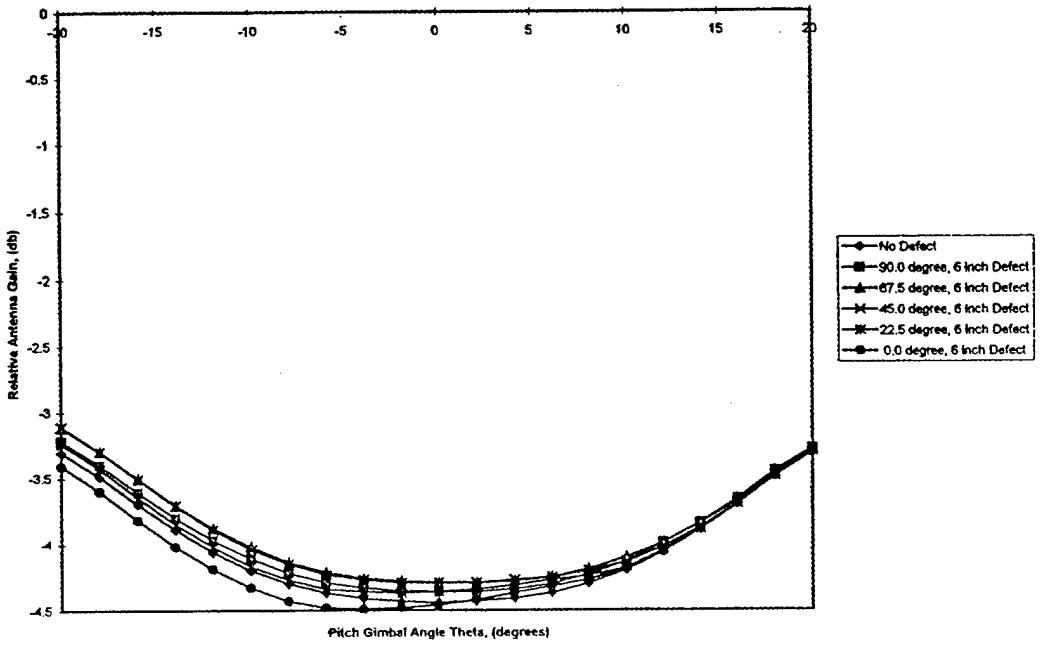

Figure A23. Effect of Angular Position of 6 in. Defect at z = 15 in. on Relative Antenna Gain for RHC Polarized Antenna and Vertically Polarized Incident Wave

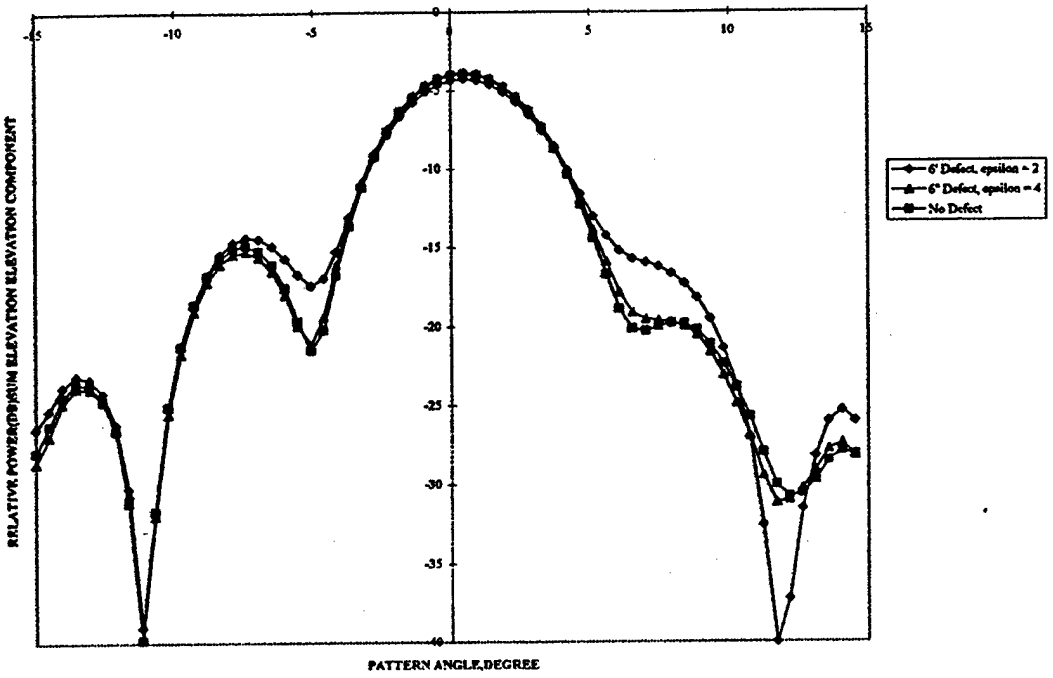

Figure A24. Effect of Defect on Receiving Pattern-Sum Channel Amplitude Elevation Cut

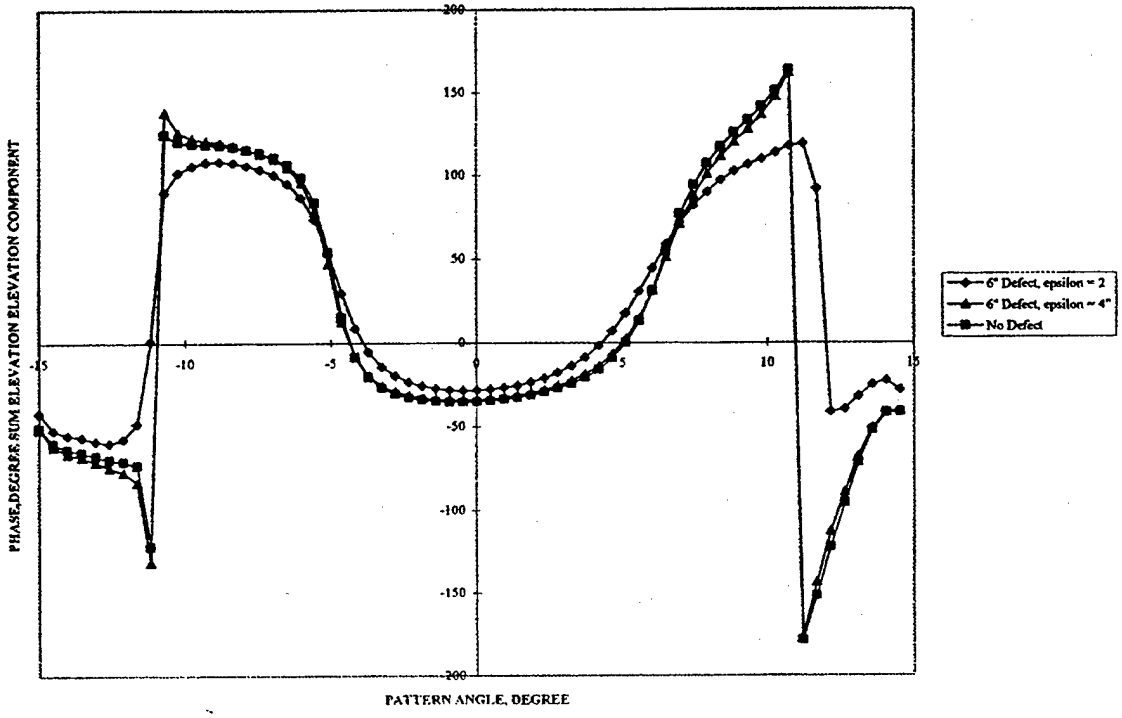

Figure A25. Effect of Defect on Receiving Pattern-Sum Channel Phase Elevation Cut

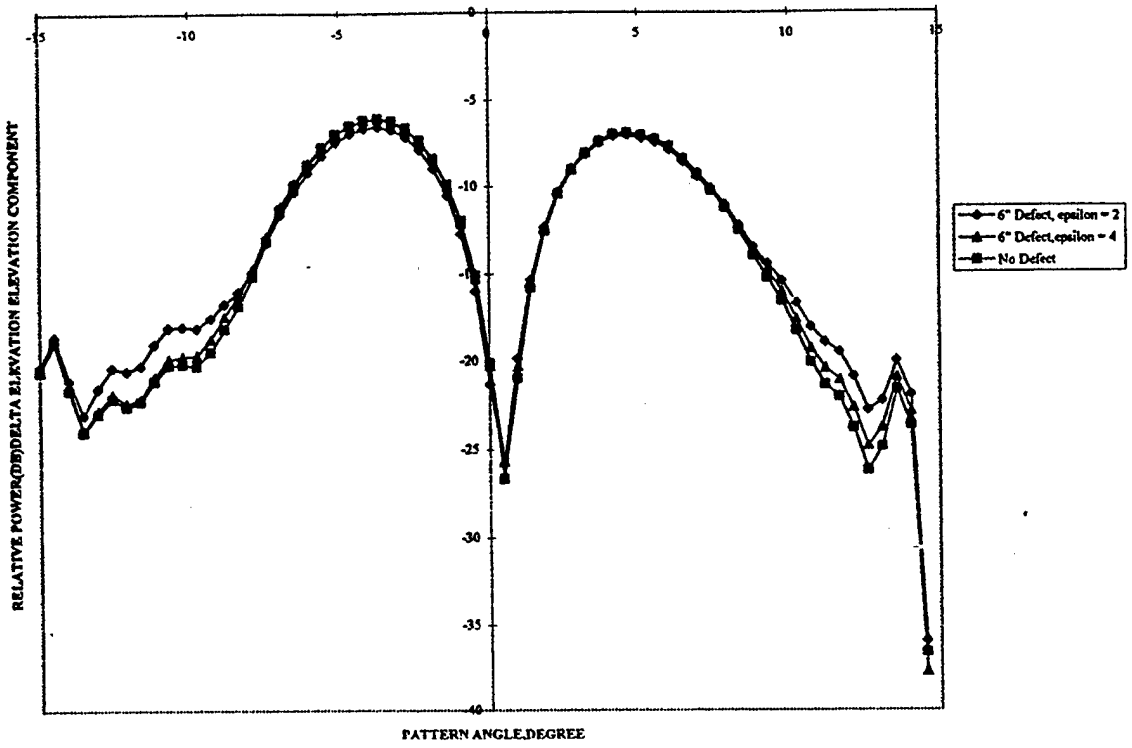

Figure A26. Effect of Defect on Receiving Pattern-Delta Amplitude Elevation Cut

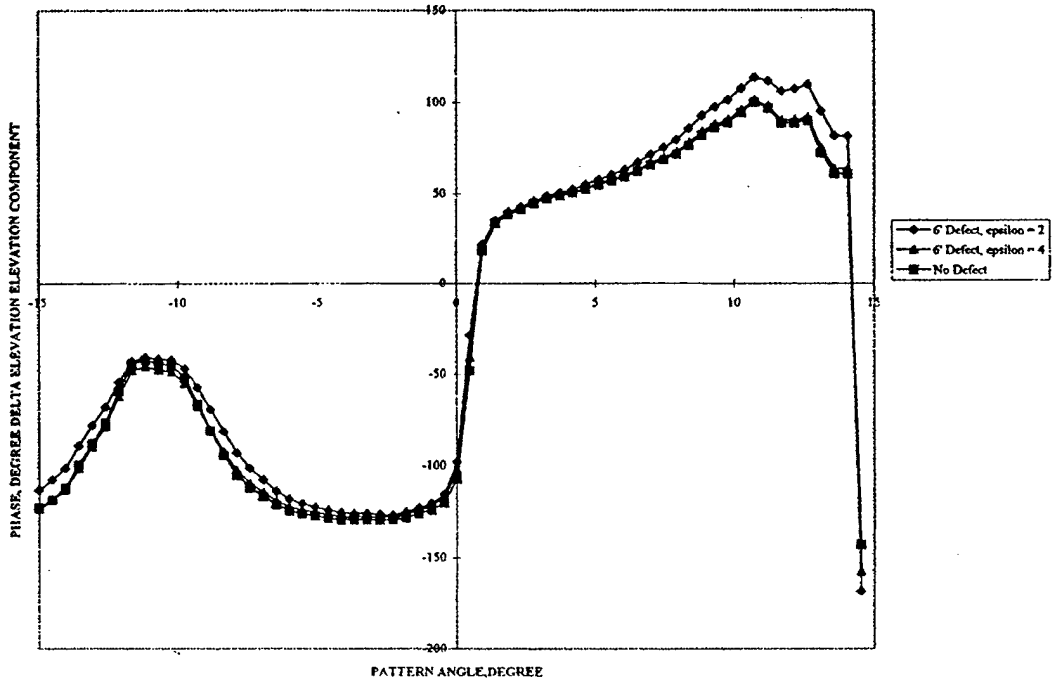

Figure A27. Effect of Defect on Receiving Pattern-Delta Phase Elevation Cut

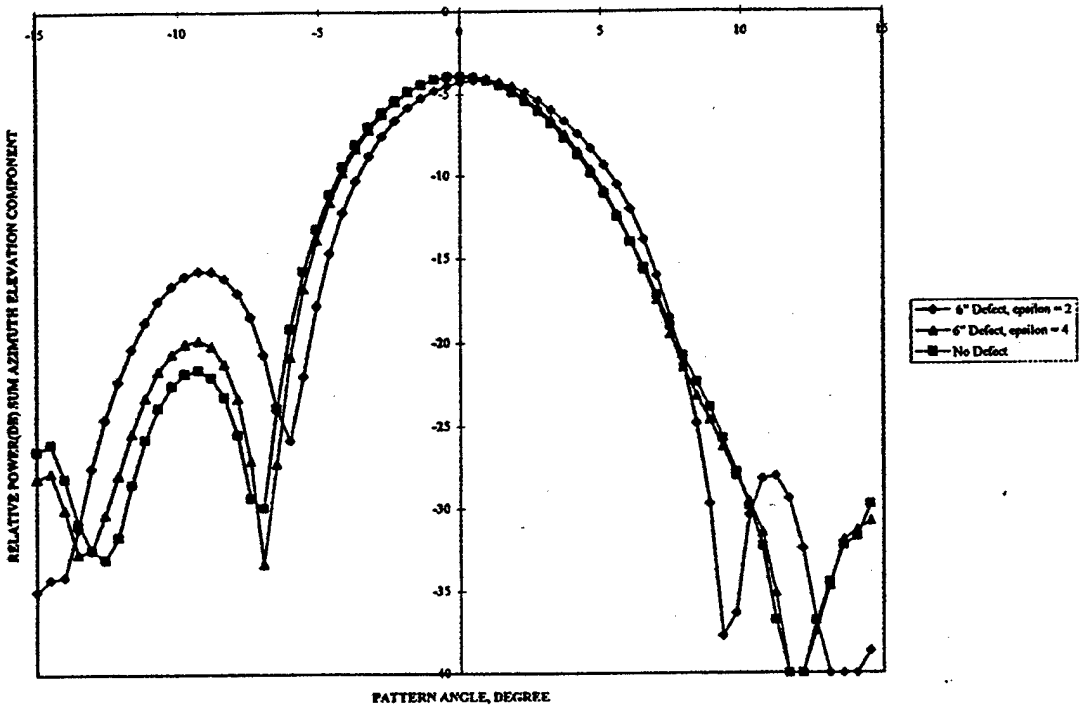

Figure A28. Effect of Defect on Receiving Pattern-Sum Channel Amplitude Azimuth Cut

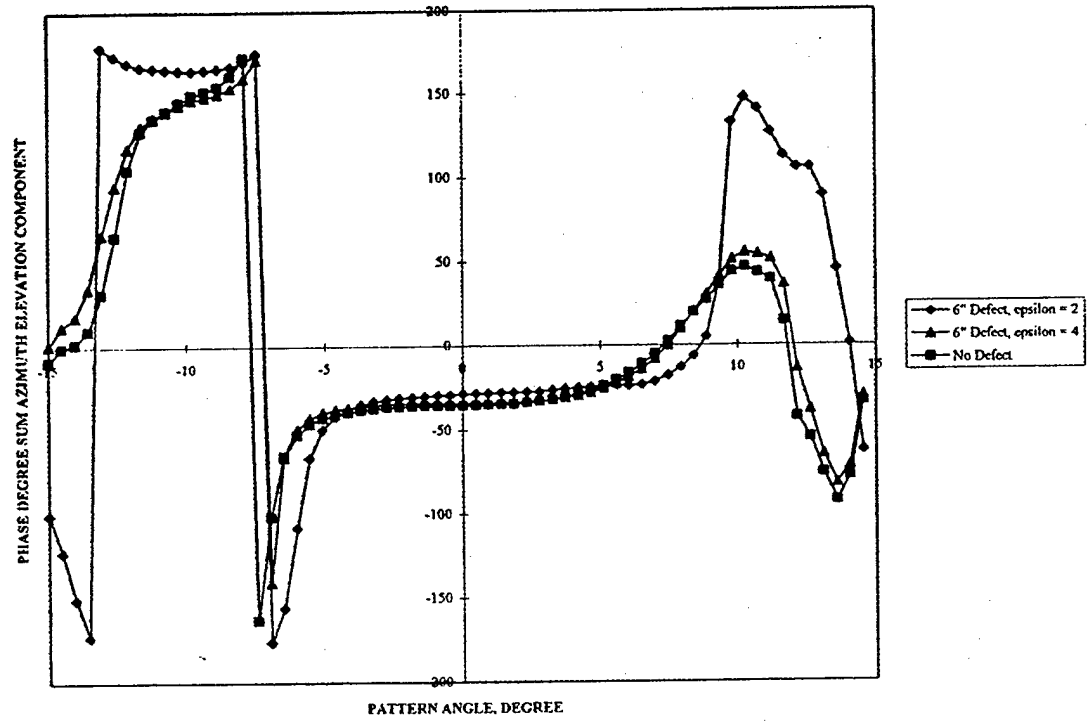

Figure A29. Effect of Defect on Receiving Pattern-Sum Channel Phase Azimuth Cut

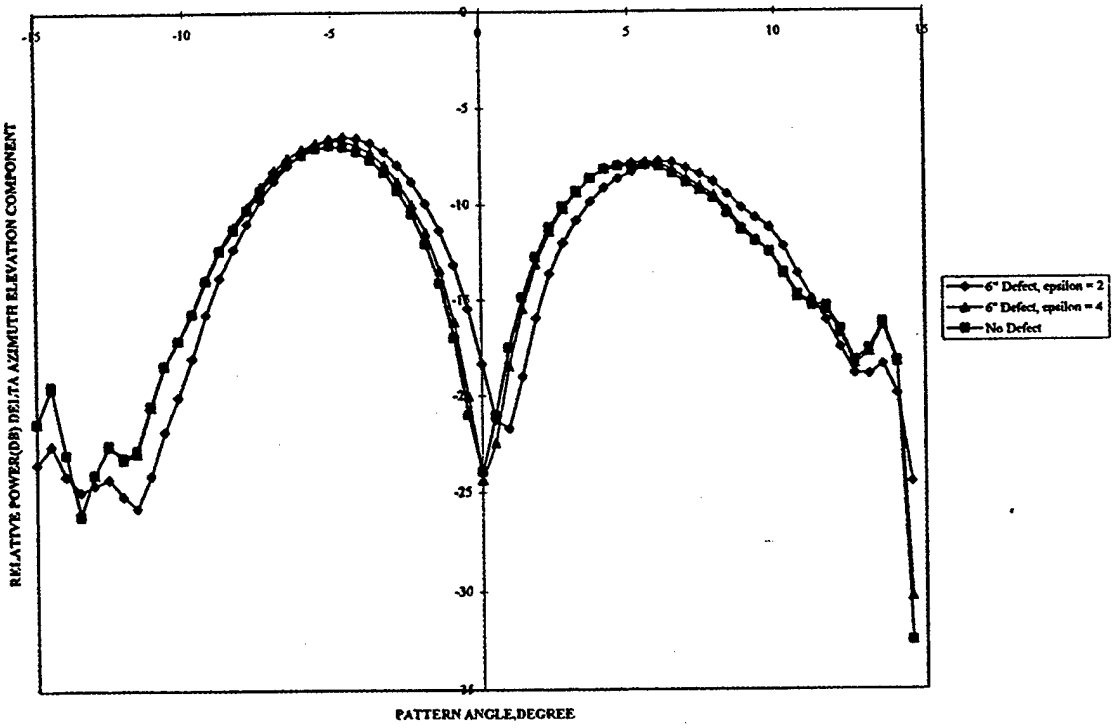

Figure A30. Effect of Defect on Receiving Pattern-Delta Amplitude Azimuth Cut

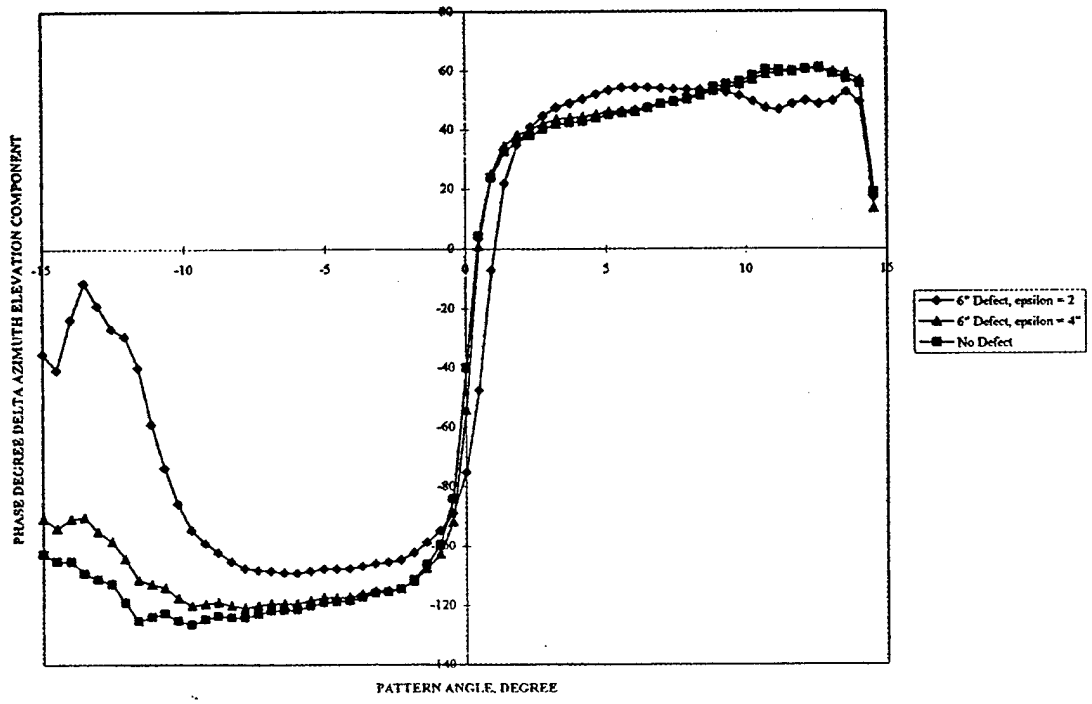

Figure A31. Effect of Defect on Receiving Pattern-Delta Azimuth Amplitude Azimuth Cut

CHANGES IN INPUT REQUIRED

The input data file for RACP™ is shown in Table A1. The case of patch type defect is chosen through the advanced data feature by setting SETDEF=F and the logical variables LVTHK and/or LERTD equal to T (True) and the following additional inputs to describe the patch geometry and the variations in layer thicknesses and/or dielectric properties as described below. Note that LVTHK and LERTD are used in the present version of RACP™ for prescribing changes in layer thicknesses and dielectric properties, which vary following a power law in axial (z direction) and as a sine function (Abs (sin ($n\phi/2+\psi_d$))) in ϕ direction. The value n (input as ND or NERTD) prescribes the number of half cycles of the circumferential variation. To differentiate between such a variation from that of a patch defect ND and/or NERTD are set equal to an integer greater than 99 (= 100 say).

To consider a thickness variation over a patch described by equation (A-1), the following inputs are required.

LVTHK - T

TZIN - Real variable equal to the axial radome coordinate of the center of the patch in inches, i.e., the value of z_1 in equation (A-1).

ND - Integer set > 99 identifying patch defect.

DDZIN(I) - Real array (single value for one layer thick wall) containing the change in thickness (in inches) of layer I at the center of the patch from the prescribed thickness DIN(I).

ZEXP(I) - The array of ratios $z_1/\ell(I)$, $\ell(I)$ being the size of the patch in inches at layer I
(see equation (A-1)) in axial direction.

DDCIN(I) - The array with circumferential dimensions θ (equation (A-1)) in radians of the patch in layer I.

PSID(I) - The array with the values of ϕ_1 in radians for layer I, denoting the position of the center of the patch.

When thickness variations are absent in the patch LVTHK may be set equal to F and other inputs are not required. Alternatively DDZIN may be set equal to 0.0.

For variations in dielectric properties over a patch of the form given by equation (A-1), the required inputs are as described next.

LERTD - T

TKIN - Real variable equal to the axial radome coordinate of the center of the patch in inches, i.e., the value of z_1 in (A-1).

NERTD - Integer set > 99 identifying patch defect.

ERZ(I) - Real array (single value for one layer) containing the change in the dielectric constant of layer I at the center of the patch from the prescribed value ER (A-1).

ZEXPER(I) - The array of ratios $z_1/\ell(I)$, $\ell(I)$ being the size of the patch in inches of layer I in axial direction (see (A-1)).

ERC(I) - The array with circumferential dimensions θ (equation (A-1)) in radians of the patch in layer I.

PSIDER(I) - The array with the values of ϕ_1 in radians for layer I, denoting the position of the center of the patch.

TDZ(I), ZEXPTD(I), TDC(I), and PSITD (I) - These quantities describe the variations of loss tangents in the same way as ERZ(I), ZEXPER(I), ERC(I) and PSIDER(I) describe the variation of the dielectric constants described above.

NOTE: It is important to note that it is advantageous to use a raster scan system (by using either RASTER.COM (with geometric optics approximation) or RASTERNG.COM (for no geometric optics approximation) as the CMD.COM file for consideration of patch type defects. This is done by setting COPY RASTER.COM (or RASTERNG.COM) CMD.COM before execution. Descriptions of the raster scan system and the polar scan system are given in Chapter 4 of the RACP™ reference library (Ref. 20 in the text). The raster scan is commonly used in RACP™ when the antenna is offset from the axis of the radome defined by the coordinates (x_o, y_o, z_o shown in Figure A32 or XROSP, YROSP and ZROSP), but they may be set to zero for no offsets. The angles ϕ_p and θ_1 (Figure A-32) specify the plane of scan and the angle (gimbal angle) in the scan plane of the radome coordinate system. ϕ_p = 90° specifies the elevation $y_A z_A$ plane (pitch plane) of the antenna. θ_L = 0 aligns the z_R (of

radome) with z_A (of antenna). Positive θ_L scans the radome axis in positive y_A direction. ϕ_p = constant selects a great circle plane that is approximately vertical. A special provision permits a single horizontal scan (in $x_A z_A$ plane of antenna, i.e., yaw or azimuth plane) by setting ϕ_p = 0.0 (see page 40 of Ref. 20 of text). When raster scan is used, the angles PSID(I), PSIDER(I), and PSITD(I) defining the patch circumferential position can be kept fixed for any value of ϕ_p or θ_L. On the other hand, if polar scan is used, these quantities have to be changed depending on the value of ϕ_p, the plane of scan.

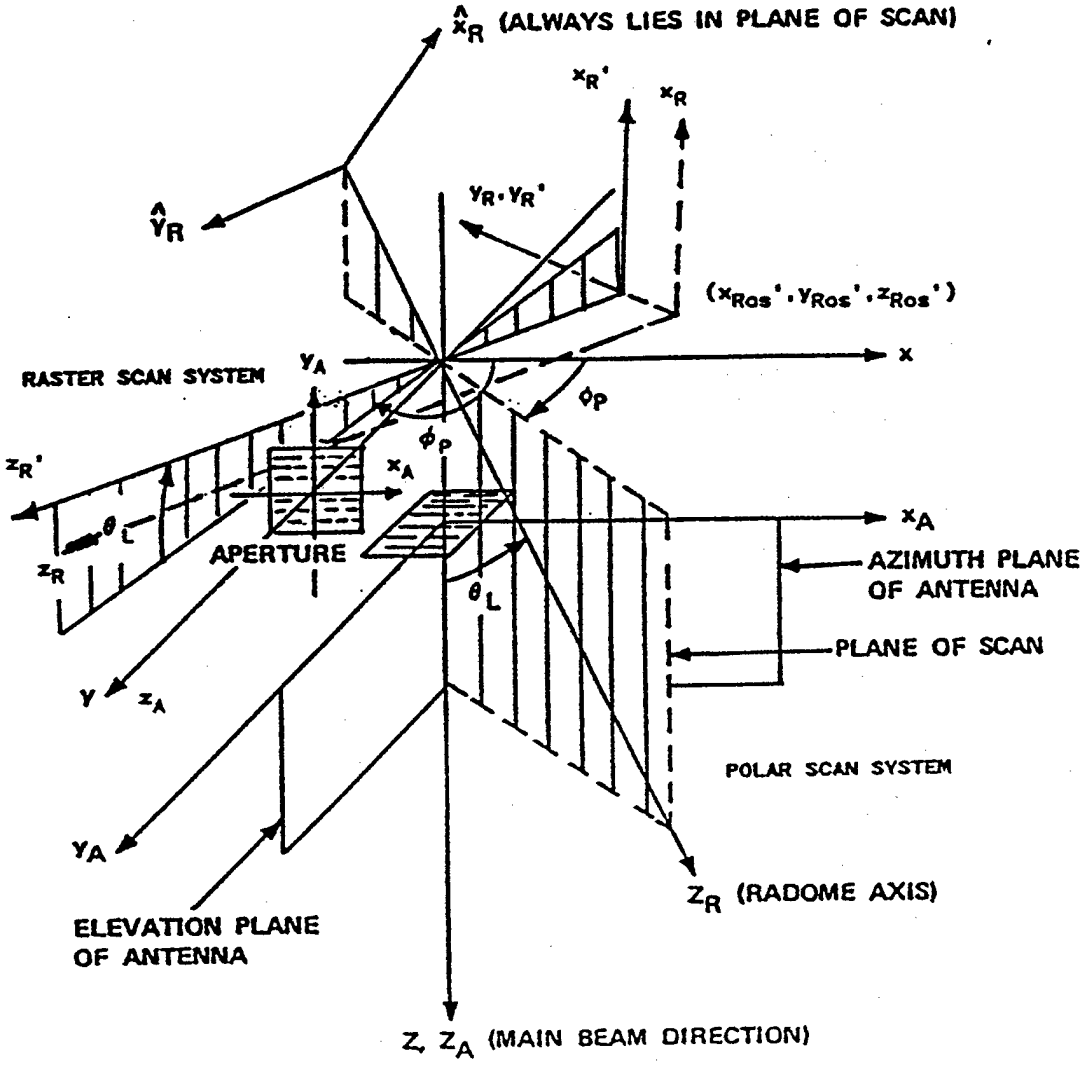

Figure A32. Polar Scan and Raster Scan Coordinate Systems Used by Program RACP

A sample input data set for a 6" patch defect ℓ = 6" with center located at z_1 = 15" ($\underline{z_1/\ell}$ = 15/6 = $\underline{2.5}$) and ϕ_1 = 0° are shown in Table A2. Note that the radius of the radome at z_1 = 15" is close to 4" so that the value of $\underline{\theta}$ (the circumferential dimension of the patch is equal to 6/4) $\underline{\text{is 1.5 radians}}$. The inputs described earlier are underlined in Tables A1 and A2. Changes in thickness, dielectric constant and loss tangent of a single layer are set equal to zero so that the results would be identical to the case with no defects.

Changes have been made in the subroutine RXMIT to consider the effects of the patch defect by the use of relations of the type given by equation (A-1) for computation of the thickness, the dielectric constant and/or the loss tangent, when the point under consideration falls inside the patch. It should be noted that the subroutines SHAPE or SHP computes the radome wall thicknesses for plotting purposes only. No changes have been made in these subroutines so the shape plot obtained may be erroneous if thickness variations are used (LVTHK set equal to T), but boresight errors and receiving patterns will be correct.

Table A1. Input Data File for RACP

```
      READ(5,6) TITLE                                    (1X,A80 FORMAT)
      READ(5,*) SETDEF,GRAFSA,GRAFNF,GRAFRV,SUPPRS,IPENCD
      READ(5,*) NFINE,NPHI,NTHE
      READ(5,*) DIAOS,RR,RA,RAPMAX
      IF (IPENCD.LE.1) READ(5,*) FREQ,OSANG
      IF (IPENCD.EO.2) READ(5,*) FSTART,FSTOP,DELF,OSANG
      READ(5,*) IOPT,IPOL,ICASE,N,IPWR
      READ(5,*) DIN(I),ER(I),TD(I)                       (I=1 to N )
      READ(5,*) FINR(I),ZTOPIN(I)                        (I=1 to NFINE)
      READ(5,*) PHI(I)                                   (I=1 to NPHI planes)
      READ(5,*) THETA(I)                                 (I=1 to NTHETA)
      READ(5,*) NX,NY,NREC
      READ(5,*) NXE,MX,IMOD
      READ(5,*) ANG1,ANG2
      READ(5,*) GRAFXN,GRAFSH,NZ
      READ(5,*) APIN,ZBOTIN,ISHAPE,ALFA
      READ(5,*) IMTR,KMTR
Read the following advanced feature data if SETDEF=F:
      READ(5,1) DUMMY
      READ(5,*) XROSP,YROSP,ZROSP
      READ(5,*,ERR=350) LVTHK,LERTD
      IF (LVTHK) THEN
      READ(5,*) TZIN,ND
      READ(5,*) DDZIN(I),ZEXP(I),DDCIN(I),PSID(I)  (I=1,N)
      ENDIF
      IF (LERTD) THEN
           READ(5,*) TKIN,NERTD
           READ(5,*) ERZ(I),ZEXPER(I),ERC(I),PSIERD(I)  (I=1,N)
           READ(5,*) TDZ(I),ZEXPTD(I),TDC(I),PSITDD(I)  (I=1,N)
           ENDIF
      READ(5,*,ERR=350) LATHK,LAERTD,GRAFAT,LPRTAT,LRDXMN
      IF (LATHK) THEN
           READ(5,*) NPINP
           READ(5,*) ZD(I),(DARB(I,J),J=1,N)    (I=1,NPINP)
           ENDIF
350   CONTINUE
      IF ((.NOT.LVTHK).AND.(.NOT.LERTD).AND.(.NOT.LATHK).AND.
      $ (.NOT.LAERTD)) THEN
      READ(5,*,ERR=355) LRDXMN
355   CONTINUE
```

Table A2. Sample Input Data Set for 6" Defect

```
RCAS 1 FOR RACP ISHAPE=3    (SINGLE LAYER TEST CASE)
F F F F T              0
            1              2              11
        12.8800000          7.0570000          1.9080000          5.0000000
        11.8030000          2.0000000
            1              1              1              1              0
0.700000E-001          5.0000000   3.000000E-003
        2.0520190          26.4300000
         .0000000
        90.0000000
         .0000000
        2.0000000
        4.0000000
        6.0000000
        8.0000000
        10.0000000
        12.0000000
        14.0000000
        16.0000000
        18.0000000
        20.0000000
        16             16          32
        256            16          4
        -15.           15.
        T T            50
        0.             0.          3              0.
        50             50
THIS LINE AND SUBSEQUENT DATA ARE READ IF SETDEF=F.
      0.          0.          0.
      T           T
      15.         100
      0.0         2.5         1.50        0.
      15.         100
      0.0         2.5         1.50        0.
      0.0         2.5         1.50        0.
      F     F     F     F     F
```

APPENDIX B

FLANGED OPEN-ENDED SENSORS FOR MICROWAVE NDE OF LAYERED MEDIA

Suite 250, 500 Office Center Drive
Fort Washington, PA 19034
Tel: 215-542-8400 Fax: 215-542-8401

INTRODUCTION

Flanged open-ended rectangular wave guides and co-axial cables are being employed by many investigators for microwave NDE of ceramics and/or other materials used in various applications. Such interrogations are especially suitable for cases where the electromagnetic properties of the materials or the components have to meet certain specific requirements (for example, in radome applications). Dielectric properties of ceramics and reinforced ceramics are often strongly influenced by the reinforcement and void content as well as delaminations and other types of flaws. Interrogation of such materials to determine such flaws and anomalies by using open-ended sensors appears to be an attractive NDE technique, where a probe is inserted through a slot or other opening at the center of the wave guide (or co-axial cable) to monitor the variations of the standing wave. Since various parameters other than the dielectric properties of the materials being interrogated (such as air gaps, metallic backing plates or other backing materials as well as delaminations) affect the standing wave pattern, analytical estimates of the expected response are very useful for planning the experiments and for correct interpretation of the measurements. Various analyses have been performed for this purpose (see, for example, ref. 1, 2). In what follows the problem shown in Figure B-1 is reconsidered for the purpose of this study.

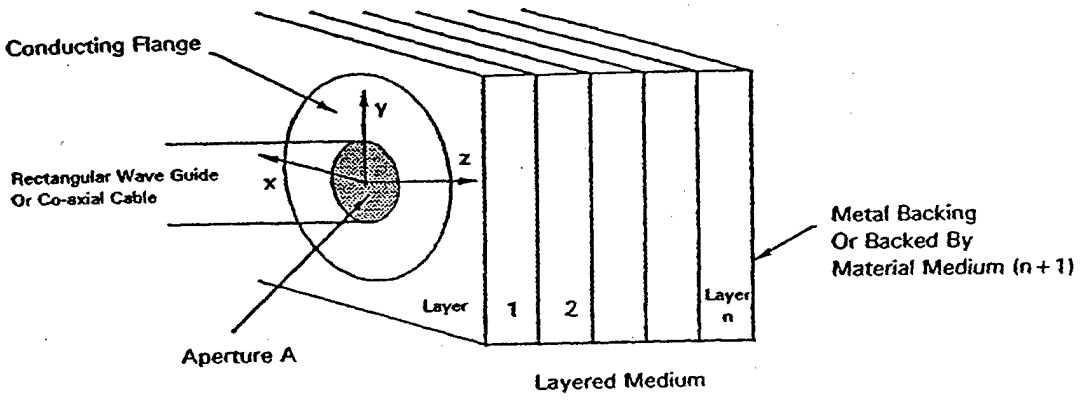

Figure B-1. Layered Medium

STATEMENT OF THE PROBLEM

For interrogation, the dominant TEM mode signal from the wave guide hits the aperture area over the layered medium. For a rectangular wave guide, the aperture is rectangular, whereas for a co-axial cable, it is bounded by two concentric circles. Outside the aperture, the electric fields tangential to the plane of the aperture (z = 0, Figure B-1) may be assumed to be zero because of the presence of the conducting flange. The electric and magnetic vector fields, $\underline{E}$ and $\underline{H}$ (a bar under a quantity indicates a vector), in each of the layers can be expressed in terms of the tangential components of the electric or magnetic fields at the aperture. To do this, the solution of Maxwell's equation for each layer is sought in terms of the vector potential $\underline{F}$ satisfying

$$\nabla^2 \underline{F} + k_1^2 \underline{F} = 0 \tag{B-1}$$

$$\underline{F} = F_x \underline{a}_x + F_y \underline{a}_y \tag{B-2}$$

$\underline{a}_x \underline{a}_y$ are the unit vectors in x and y directions. $\underline{E}$ and $\underline{H}$ are given by

$$\underline{E} = -\underline{\nabla} \times \underline{F} \tag{B-3}$$

$$\underline{H} = \frac{1}{j\omega\mu}\left[k_1^2 \underline{F} + \underline{\nabla\nabla} \cdot \underline{F}\right] \tag{B-4}$$

where $j = \sqrt{-1}$ and ω is the frequency. μ is the magnetic permeability and k_1 is the complex propagation constant of the layer material, i.e.,

$$k_1^2 = k_o^2 \varepsilon = k_o^2 (\varepsilon' - i\varepsilon'') \tag{B-5}$$

$\varepsilon', \varepsilon''$ are the real and imaginary parts of the dielectric constant ε and k_o is the free space propagation constant given by

$$k_o = \frac{2\pi}{\lambda_o} = \frac{\omega}{c} \tag{B-6}$$

λ_o and c are the free space wave length and wave speed, respectively.

SOLUTION IN TERMS FOURIER TRANSFORMS

All quantities appearing in equations (B1-B4) can be assumed as a product of two functions, one varying with space (x, y, z coordinates) and the other with time, t. The time varying function is the same for all quantities and is assumed to be exp ($j\omega t$). In the expressions of the quantities which follow, this time dependent function will be omitted, since their spatial variations are of interest. Further, we will first obtain some relations involving the Fourier transforms of these quantities. Fourier transform $\bar{F}_\alpha$ (over bar denoting the transform) of the function F_α and the inverse relation are given by

$$\bar{F}_\alpha(\kappa_x,\kappa_y,z)=\int_{-\infty}^{\infty}\int_{-\infty}^{\infty}F_\alpha(x,y,z)\exp(j\kappa_x x+j\kappa_x y)dxdy \qquad \text{(B-7)}$$

$$F_\alpha(x,y,z)=\frac{1}{4\pi^2}\int_{-\infty}^{\infty}\int_{-\infty}^{\infty}\bar{F}_\alpha(\kappa_x,\kappa_y,z)\exp(-j\kappa_x x-j\kappa_y y)d\kappa_x d\kappa_y \qquad \text{(B-8)}$$

Similar relations hold for other functions and their transforms. Substitution of equation (B-2) in (B-1) and use of (B-7), (B-8) result in two ordinary differential equations.

$$\frac{\partial^2\bar{F}_\alpha}{\partial z^2}+(k_1^2-\kappa_x^2-\kappa_y^2)\bar{F}_\alpha=0;\quad \alpha=x,y \qquad \text{(B-9)}$$

whose solutions are

$$\bar{F}_\alpha=A_\alpha\cos k_0\lambda z-B_\alpha\sin k_0\lambda z;\quad \alpha=x,y \qquad \text{(B-10)}$$

where A_α and $B_\alpha(\alpha=x,y)$ are unknown complex valued functions of κ_x and κ_y, and z is measured from the center of the layer under consideration. λ is the characteristic root given by

$$\lambda=\sqrt{\varepsilon-\kappa'^2_x-\kappa'^2_y} \qquad \text{(B-11)}$$

such that

$$\mathrm{Re}(\lambda)\geq 0 \text{ and } \mathrm{Im}(\lambda)\leq 0 \qquad \text{(B-12)}$$

κ'_x, κ'_y are nondimensional transform parameters, i.e.,

$$\kappa'_\alpha=\kappa_\alpha/k_0;\quad \alpha=x,y \qquad \text{(B-13)}$$

Substituting (B-10) in (B-3) and (B-4), one obtains

$$\bar{E}_x = -k_o\lambda\left(A_y \sin k_o\lambda z + B_y \cos k_o\lambda z\right) \tag{B-14}$$

$$\bar{E}_y = k_o\lambda\left(A_x \sin k_o\lambda z + B_x \cos k_o\lambda z\right) \tag{B-15}$$

$$\bar{h}_x = j\omega\mu_o\bar{H}_x = \left[\left(k_i^2 - \kappa_x^2\right)\bar{F}_x - \kappa_x\kappa_y\bar{F}_y\right]\frac{\mu_o}{\mu} \tag{B-16}$$

$$\bar{h}_y = j\omega\mu_o\bar{H}_y = \left[\left(k_i^2 - \kappa_y^2\right)\bar{F}_y - \kappa_x\kappa_y\bar{F}_x\right]\frac{\mu_o}{\mu} \tag{B-17}$$

Substituting $z = +h/2$ and $-h/2$ in (B-14) one obtains two expressions which can be inverted to obtain A_y and B_y in terms of $\bar{E}_x^+$ and $\bar{E}_x^-$ defined as

$$\bar{E}_x^{\pm} = \bar{E}_x \quad \text{at } z = \pm h/2 \tag{B-18}$$

By using a similar procedure with equation (B-15) with $z = \pm h/2$, A_x and B_x can be expressed in terms of $\bar{E}_y^{\pm}$, where

$$\bar{E}_y^{\pm} = \bar{E}_y \text{ at } z = \pm h/2 \tag{B-19}$$

Substitution of these relations in (B-10) and in (B-16) and (B-17) at $z = \pm h/2$ yield

$$\frac{k_o\lambda\mu}{\mu_o}\begin{bmatrix}\bar{h}_x^-\\ \bar{h}_x^+\end{bmatrix} = -[B]\left[\left(k_i^2 - \kappa_x^2\right)\begin{bmatrix}\bar{E}_y^-\\ -\bar{E}_y^+\end{bmatrix} + \kappa_x\kappa_y\begin{bmatrix}\bar{E}_x^-\\ -\bar{E}_x^+\end{bmatrix}\right] \tag{B-20}$$

$$\frac{k_o\lambda\mu}{\mu_o}\begin{bmatrix}\bar{h}_y^-\\ \bar{h}_y^+\end{bmatrix} = [B]\left[\left(k_i^2 - \kappa_y^2\right)\begin{bmatrix}\bar{E}_x^-\\ -\bar{E}_x^+\end{bmatrix} + \kappa_x\kappa_y\begin{bmatrix}\bar{E}_y^-\\ -\bar{E}_y^+\end{bmatrix}\right] \tag{B-21}$$

where

$$\bar{h}_x^{\pm} = \bar{h}_x \quad \text{at } z = \pm h/2 \tag{B-22}$$

$$\bar{h}_y^{\pm} = \bar{h}_y \text{ at } z = \pm h/2 \tag{B-23}$$

and the matrix [B] is given by

$$[B] = \begin{bmatrix}\cot k_o\lambda h & \operatorname{cosec} k_o\lambda h\\ \operatorname{cosec} k_o\lambda h & \cot k_o\lambda h\end{bmatrix} \tag{B-24}$$

Multiplying both sides of (B-20) by κ_y and those of (B-21) by $-\kappa_x$, adding of the resulting expressions and inverting, one obtains

$$k_o \begin{bmatrix} \kappa_y \bar{E}_y^- + \kappa_x \bar{E}_x^- \\ -\kappa_y \bar{E}_y^+ - \kappa_x \bar{E}_x^+ \end{bmatrix} = [C] \begin{bmatrix} \kappa_y \bar{h}_x^- - \kappa_x \bar{h}_y^- \\ \kappa_y^+ \bar{h}_x^+ - \kappa_x \bar{h}_y^+ \end{bmatrix} \quad \text{(B-25)}$$

where

$$[C] = -\frac{k_o^2 \mu \lambda}{k_i^2 \mu_o} [B]^{-1} = \frac{\mu \lambda}{\mu_o \varepsilon} \begin{bmatrix} \cot k_o \lambda h & -\operatorname{cosec} k_o \lambda h \\ -\operatorname{cosec} k_o \lambda h & \cot k_o \lambda h \end{bmatrix} \quad \text{(B-26)}$$

A similar procedure involving multiplication of both sides of (B-20) and (B-21) by κ_x and κ_y, respectively, addition of the resulting expressions and inversion yields

$$k_o \begin{bmatrix} \kappa_x \bar{E}_y^- - \kappa_y \bar{E}_x^- \\ -\kappa_x \bar{E}_y^+ + \kappa_y \bar{E}_x^+ \end{bmatrix} = [D] \begin{bmatrix} \kappa_x \bar{h}_x^- + \kappa_y \bar{h}_y^- \\ \kappa_x \bar{h}_x^+ + \kappa_y \bar{h}_y^+ \end{bmatrix} \quad \text{(B-27)}$$

where

$$[D] = -\frac{\mu}{\mu_o \lambda} [B]^{-1} = \frac{\mu}{\mu_o \lambda} \begin{bmatrix} \cot k_o \lambda h & -\operatorname{cosec} k_o \lambda h \\ -\operatorname{cosec} k_o \lambda h & \cot k_o \lambda h \end{bmatrix} \quad \text{(B-28)}$$

COMPLETE SOLUTION FOR THE LAYERED MEDIUM

It may be noted that relations (B-25) and (B-27) are similar in form for all layers of finite thickness with the elements of the matrices [C] and [D] differing from layer to layer because of thickness and material property differences. At the interface (ℓ+1) of layers ℓ and (ℓ+1), we denote the quantities with a superscript*, i.e.,

$$\overline{E}_\alpha^{(\ell)+} = \overline{E}_\alpha^{(\ell+1)-} = \overline{E}_\alpha^{(\ell+1)*} \qquad \text{(B-29)}$$

$$\overline{h}_\alpha^{(\ell)+} = \overline{h}_\alpha^{(\ell+1)-} = \overline{h}_\alpha^{(\ell+1)*}$$

$\overline{E}_\alpha^{(1)*}$, $\overline{h}_\alpha^{(1)*}$ denote the values of the quantities at the top of layer 1 (global z coordinate $z = 0$ in the plane of the aperture A in Figure B-1) and $\overline{E}_\alpha^{(n+1)*}$ and $\overline{h}_\alpha^{(n+1)*}$ are the values at the bottom of layer n ($z = h_1 + \ldots + h_n$), sum of the thicknesses of layers 1 to n.

Now we add second of equation (B-25) for layer ℓ to first of the equation (B-25) for layer (ℓ+1) for ℓ varying from 1 to n and assemble the following system of equations for evaluation of $\kappa_y \overline{h}_x^{(i)*} - \kappa_x \overline{h}_y^{(i)*}$ $(i = 1, 2, \ldots n+1)$

$$k_0 \begin{bmatrix} \kappa_y \bar{E}_y^{*(1)} + \kappa_x \bar{E}_x^{*(1)} \\ 0 \\ 0 \\ \vdots \\ 0 \\ 0 \\ -\kappa_y \bar{E}_y^{*(n+1)} - \kappa_x \bar{E}_x^{*(n+1)} \end{bmatrix} = \begin{bmatrix} (G) \\ C \end{bmatrix} \begin{bmatrix} \kappa_y \bar{h}_x^{*(1)} - \kappa_x \bar{h}_y^{*(1)} \\ \kappa_y \bar{h}_x^{*(2)} - \kappa_x \bar{h}_y^{*(3)} \\ \vdots \\ \kappa_y \bar{h}_x^{*(i)} - \kappa_x \bar{h}_y^{*(i)} \\ \vdots \\ \kappa_y \bar{h}_x^{*(n)} - \kappa_x \bar{h}_y^{*(n)} \\ \kappa_y \bar{h}_x^{*(n+1)} - \kappa_x \bar{h}_y^{*(n+1)} \end{bmatrix} \qquad \text{(B-30)}$$

$$\begin{bmatrix} (G) \\ C \end{bmatrix} = \begin{bmatrix} c_{11}^{(1)} & c_{12}^{(1)} & 0 & 0 & 0 & & & 0 \\ c_{12}^{(1)} & c_{22}^{(1)} + c_{11}^{(2)} & c_{12}^{(2)} & 0 & 0 & & & 0 \\ 0 & c_{12}^{(2)} & c_{22}^{(2)} + c_{11}^{(3)} & c_{12}^{(3)} & 0 & & & 0 \\ 0 & 0 & c_{12}^{(3)} & & & & & 0 \\ 0 & & & & c_{12}^{(i-1)} & c_{22}^{(i-1)} + c_{11}^{(i)} & & 0 \\ 0 & & & & & & & 0 \\ 0 & & & & & & & 0 \\ 0 & & & & & 0 & c_{12}^{(n-1)} & c_{22}^{(n-1)} + c_{11}^{(n)} & c_{12}^{(n)} \\ 0 & 0 & 0 & 0 & 0 & 0 & 0 & c_{12}^{(n)} & c_{22}^{(n)} \end{bmatrix} \qquad \text{(B-31)}$$

where $\overset{(i)}{c_{ij}}$ (i,j = 1,2) are the elements of the matrix [C] (equation (B-26) of layer i). Note that the first of equation (B-25) for layer 1 and second of (B-25) for layer n are left unaltered in the system (B-3) as the first and the last equation.

A similar procedure (addition of second of equation (B-27) for layer ℓ to first of (B-27) for layer (ℓ+1) yields the following system of equations for evaluation of. $\kappa_x \overset{(i)}{\bar{h}_x} + \kappa_y \overset{(i)}{\bar{h}_x}$ (i = 1,2,..., n+1).

$$\begin{bmatrix} \kappa_x \overset{(1)}{\bar{E}y}^* & - & \kappa_y \overset{(1)}{\bar{E}x}^* \\ 0 & & \\ 0 & & \\ \cdot & & \\ \cdot & & \\ \cdot & & \\ \cdot & & \\ \cdot & & \\ 0 & & \\ 0 & & \\ -\kappa_x \overset{(n+1)}{\bar{E}y}^* & + & \kappa_y \overset{(n+1)}{\bar{E}x}^* \end{bmatrix} = \begin{bmatrix} (G) \\ D \end{bmatrix} \begin{bmatrix} \kappa_x \overset{(1)}{\bar{h}x}^* & + & \kappa_y \overset{(1)}{\bar{h}y}^* \\ \kappa_x \overset{(2)}{\bar{h}x}^* & + & \kappa_y \overset{(2)}{\bar{h}y}^* \\ 0 & & \\ 0 & & \\ \cdot & & \\ \kappa_x \overset{(i)}{\bar{h}x}^* & + & \kappa_y \overset{(i)}{\bar{h}y}^* \\ \cdot & & \\ \cdot & & \\ \cdot & & \\ \cdot & & \\ \kappa_x \overset{(n)}{\bar{h}x}^* & + & \kappa_y \overset{(n)}{\bar{h}y}^* \\ \kappa_x \overset{(n+1)}{\bar{h}x}^* & + & \kappa_y \overset{(n+1)}{\bar{h}y}^* \end{bmatrix} \qquad (B-32)$$

$$\begin{bmatrix} (G) \\ D \end{bmatrix} = \begin{bmatrix} d_{11}^{(1)} & d_{12}^{(1)} & 0 & 0 & & & & \\ d_{12}^{(1)} & \left(d_{22}^{(1)} + d_{11}^{(2)}\right) & d_{12}^{(2)} & 0 & & & & \\ 0 & d_{12}^{(2)} & \left(d_{22}^{(3)} + d_{11}^{(3)}\right) & d_{12}^{(3)} & & & & \\ & & d_{12}^{(i-1)} & \left(d_{22}^{(i-1)} + d_{11}^{(i)}\right) & d_{12}^{(i)} & & & \\ 0 & & & d_{12}^{(n-1)} & \left(d_{12}^{(n-1)} + d_{11}^{(n)}\right) & d_{12}^{(n)} & & \\ 0 & & & & d_{12}^{(n)} & d_{22}^{(n)} & & \\ 0 & & & & & & & \end{bmatrix} \qquad \text{(B-33)}$$

Note that $d_{ij}^{(i)}$ (i,j-1,2) are the elements of the matrix [D] (equation (B-28) for layer i). Again, first of equation (B-27) for layer 1 and second of (B-27) for layer n are left unaltered as the first and last equation in the system (B-32).

CASE 1. LAYER n BACKED BY A CONDUCTOR

For a layered system with the n^{th} layer backed by a conductor (Figure B-1), E_x and E_y are identically zero at the back of layer n (global $z = h_1 + \ldots h_n$) and, therefore, the last terms in the vectors on the left hand sides (B-30) and (B-32) are zero. Therefore, each term of the vector involving the transforms of the magnetic fields tangential to the interfaces (or rather their derivatives) appearing on the right hand sides of (B-30) and (B-32) can be evaluated in terms of the transforms of tangential electric fields at the plane of the apeture.

In particular, the transforms of the tangential magnetic fields at the plane of the aperture are

$$\kappa_y \overline{h}_x^{*(1)} - \kappa_x \overline{h}_y^{*(1)} = \frac{\delta_1}{\Delta_1} k_o \left(\kappa_y \overline{E}_y^{*(1)} + \kappa_x \overline{E}_x^{*(1)} \right) \qquad \text{(B-34)}$$

and

$$\kappa_x \overset{(1)}{\overline{h}}^{*}_{x} - \kappa_y \overset{(1)}{\overline{h}}^{*}_{y} = \frac{\delta_s}{\Delta_2} k_o \left(\kappa_y \overset{(1)}{\overline{E}}^{*}_{y} - \kappa_y \overset{(1)}{\overline{E}}^{*}_{x} \right) \tag{B-35}$$

where

$$\begin{aligned}
\Delta_1 &= \text{Det} \begin{bmatrix} (G) \\ C \end{bmatrix} \\
\delta_1 &= \text{Adjoint of } \begin{bmatrix} (G) \\ c_{11} \end{bmatrix} \text{ in determinant of } \begin{bmatrix} (G) \\ C \end{bmatrix} \\
\Delta_2 &= \text{Det} \begin{bmatrix} (G) \\ D \end{bmatrix} \\
\delta_2 &= \text{Adjoint of } \begin{bmatrix} (G) \\ d_{11} \end{bmatrix} \text{ in determinant of } \begin{bmatrix} (G) \\ D \end{bmatrix}
\end{aligned} \tag{B-36}$$

CASE 2. LAYER n BACKED BY A HALF SPACE

If the layered system is not backed by a conductor, but by a half space of material medium (n+1), then the tangential electric fields are not zero at the back of layer n. However, the transforms of electric fields are related to those of the magnetic fields at the interface (n+1) between layer n and medium (n+1) by the following relations.

$$k_o \begin{pmatrix} \overset{(n+1)}{-\kappa_y} \overset{(n+1)}{\overline{E}}^{*}_{y} & \overset{(n+1)}{-\kappa_x} \overset{(n+1)}{\overline{E}}^{*}_{x} \end{pmatrix} = -j \frac{\lambda_{n+1}\mu_{n+1}}{\varepsilon_{n+1}\mu_o} \begin{pmatrix} \overset{(n+1)}{\kappa_y} \overset{(n+1)}{\overline{h}}^{*}_{x} & \overset{(n+1)}{-\kappa_x} \overset{(n+1)}{\overline{h}}^{*}_{y} \end{pmatrix} \tag{B-37}$$

and

$$k_o \begin{pmatrix} \overset{(n+1)}{-\kappa_x} \overset{(n+1)}{\overline{E}}^{*}_{y} & \overset{(n+1)}{+\kappa_y} \overset{(n+1)}{\overline{E}}^{*}_{x} \end{pmatrix} = -\frac{j\mu_{n+1}}{\lambda_{n+1}\mu_o} \begin{pmatrix} \overset{(n+1)}{\kappa_x} \overset{(n+1)}{\overline{h}}^{*}_{x} & \overset{(n+1)}{+\kappa_y} \overset{(n+1)}{\overline{h}}^{*}_{y} \end{pmatrix} \tag{B-38}$$

Subscripts (n+1) indicate quantities for the medium n+1. Substituting these relations in the left hand sides of the last equations in the systems (B-30) and (B-32) and transferring them to the right hand sides of these equations, the last terms in the vectors on the left hand sides become zero. However, the terms $\overset{(G)}{c}_{(n+1)(n+1)}$ and $\overset{(G)}{d}_{(n+1)(n+1)}$ of the matrices $\begin{bmatrix} (G) \\ C \end{bmatrix}$ and $\begin{bmatrix} (G) \\ D \end{bmatrix}$ are changed to

$$(G)_{C_{(n+1)(n+1)}} = (n)_{C_{22}} + j\frac{\lambda_{n+1}\mu_{n+1}}{\varepsilon_{n+1}\mu_0} \tag{B-39}$$

$$(G)_{d_{(n+1)(n+1)}} = (n)_{d_{22}} + \frac{j\mu_{n+1}}{\lambda_{n+1}\mu_0} \tag{B-40}$$

After this modification, inversion of (B-30) and (B-32) can be done in the same manner as discussed for case 1 (see equation (B-34), (B-35) and (B-36), which apply to this case too, with the modifications of $\begin{bmatrix}(G)\\C\end{bmatrix}$ and $\begin{bmatrix}(G)\\D\end{bmatrix}$).

TRANSFORM INVERSIONS AND SOLUTION PROCEDURE

$$\overset{(1)}{\overset{*}{h}}_x = \frac{k_o}{(\kappa_x^2+\kappa_y^2)}\left[\left(\frac{\delta_1}{\Delta_1}\kappa_y^2+\frac{\delta_2}{\Delta_2}\kappa_x^2\right)\overset{(1)}{\overset{*}{E}}_y+\left(\frac{\delta_1}{\Delta_1}-\frac{\delta_2}{\Delta_2}\right)\kappa_x\kappa_y\overset{(1)}{\overset{*}{E}}_x\right] \qquad \text{(B-41)}$$

From equations (B-34) and (B-35), it follows that

$$\overset{(1)}{\overset{*}{h}}_y = \frac{k_o}{(\kappa_x^2+\kappa_y^2)}\left[\left(\frac{\delta_2}{\Delta_2}-\frac{\delta_1}{\Delta_1}\right)\kappa_x\kappa_y\overset{(1)}{\overset{*}{E}}_y-\left(\frac{\delta_2}{\Delta_2}\kappa_y^2+\frac{\delta_1}{\Delta_1}\kappa_x^2\right)\overset{(1)}{\overset{*}{E}}_x\right] \qquad \text{(B-42)}$$

These transforms can be inverted using the relation (8) to evaluate $\overset{(1)}{h}_x^*$ and $\overset{(1)}{h}_y^*$ provided $\overset{(1)}{E}_x^*$ and $\overset{(1)}{E}_y^*$ are known over the aperture (they are zero elsewhere). For an approximate solution, the tangential electric fields at the aperture may be assumed to be the sum of the incident and reflected parts of the dominant TE mode for the wave guide or the co-axial cable. The corresponding magnetic field can then be evaluated for calculation of the aperture admittance, which can be used for suggesting guidelines for nondestructive examination. In the following sections, we will discuss procedures for such calculations. It should be noted, however, that for obtaining a correct solution other modes in the wave guide have to be considered and all the tangential fields at the aperture should be matched with those of the wave guide. For this purpose, it is necessary to express the tangential fields at the aperture in the wave guide at $z=0$ as

$$\underline{E}(x,y,o) = V_{io}\,\underline{e}_o(x,y) + \sum_{n=0}^{\infty} V_m\,\underline{e}_n(x,y) \qquad \text{(B-43)}$$

$$\underline{H}(x,y,o) = Y_o V_{io}\,\underline{h}_o(x,y) - \sum_{n=0}^{\infty} Y_n V_m\,\underline{h}_n(x,y) \qquad \text{(B-44)}$$

V_{io}, V_{ro} are the magnitudes of the dominant incident and reflected modes, V_m are the magnitudes of other reflected modes. Y_n is the admittance of the wave guide in the n^{th} mode, which is known. $\underline{e}_n$ and $\underline{h}_n$ are the orthonormal mode vectors. The normalized aperture admittance for the dominant mode is given

$$\frac{Y}{Y_o} = \frac{V_{io} - V_{ro}}{V_{io} + V_{ro}} \qquad \text{(B-45)}$$

For numerical solution, a finite number of terms ($n \leq N$) are retained in (B-43) and (B-44) and V_m ($n = 0,1...N$) are expressed in terms of V_{io} by matching the magnetic fields obtained from (41) and (B-42) with those from (B-44) by collocation (point matching over a chosen number of points) or other error minimization procedures. It may be noted that some of the fields may be singular at the aperture boundaries when the loss tangents for the material dielectric constants are zero (see Reference 2) and other improved techniques (singular integral equations) may be required for solution. When the loss tangents are not small, one term solution ($n=0$) may be adequate (see Reference 1) and the procedure often yields good correlation with experimental data. For such solution, one may choose

$$V_{io} + V_{ro} = 1 \qquad \text{(B-46)}$$

$$V_m = 0 \quad ; \quad n > 0 \qquad \text{(B-47)}$$

and it is only necessary to find $V_{io} - V_{ro}$ from the dominant magnetic field (see eqn (B-44)) and use (45) to find the normalized aperture admittance. The case of a rectangular wave guide and that of a co-axial cable are considered in the next two sections.

APPROXIMATE SOLUTION FOR RECTANGULAR WAVE GUIDE

The wave guide is assumed to be of lengths a and b in x and y directions, respectively, (Figure B-2) with a > b. Considering only the dominant mode in the guide, which is the TE_{10} mode, and neglecting all other reflected modes, one may choose

$$E_y^{*(1)} = \cos\frac{\pi x}{a} \qquad \text{(B-48)}$$

$$-a/2 \le x \le a/2 \text{ and } -b/2 \le y \le b/2$$

$$E_x^{*(1)} = 0 \qquad \text{(B-49)}$$

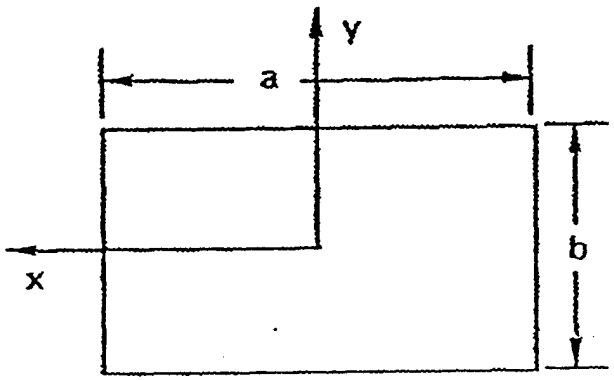

Figure B-2. Rectangular Wave Guide

Note that

$$E_x^{(1)} = E_y^{(1)} = 0, |x| > a/2 \text{ or } |y| > b/2 \qquad \text{(B-50)}$$

because of the presence of the conducting flange (Figure B-1). Using equation (B-7) and (B-48 - B-50) as well as the condition that $E_y^{*(1)}$ is an even function of x and y

$$\overset{(1)}{\overline{E}_y^*} = \int_{-a/2}^{a/2} \int_{-b/2}^{b/2} \cos\pi x/a \cos\kappa_x x \cos\kappa_y y \, dx \, dy$$
$$= \frac{4\pi}{a} \frac{\cos\kappa_x a/2 \sin\kappa_y b/2}{\left(\pi^2/a^2 - \kappa_x^2\right)\kappa_y} \qquad \text{(B-51)}$$

$$\overset{(1)}{\overline{E}_x^*} = 0 \qquad \text{(B-52)}$$

Use of equations (B-52), (B-41), and (B-8) and the condition that $\overset{(1)}{\overline{h}_x}$ is an even function of κ_x and κ_y yields

$$j\omega\mu_o \overset{(1)}{H_x^*} = \overset{(1)}{h_x^*} = \frac{k_o}{4\pi^2} \int_{-\infty}^{\infty} \int_{-\infty}^{\infty} \frac{1}{\left(\kappa_x^2 + \kappa_y^2\right)} \left[\frac{\delta_1}{\Delta_1} \kappa_y^2 + \frac{\delta_2}{\Delta_2} \kappa_x^2 \right] \overset{(1)}{\overline{E}_y^*} \cos\kappa_x x \cos\kappa_x y \, d\kappa_x d\kappa_y \qquad \text{(B-53)}$$

Now we note that $\overset{(1)}{H_x^*}$ within the aperture can be expanded in the following form (as discussed in the previous section)

$$\overset{(1)}{H_x^*} = \overset{(1)}{H_{xo}^*} \cos\pi x/a + \sum_{n>0} \overset{(1)}{H_{xn}^*} f_n(x,y) \qquad \text{(B-54)}$$

where $f_n(x,y)$ are the orthogonal mode functions for higher modes of the wave guide. H_{xo}^* can be evaluated as

$$\overset{(1)}{H_{xo}^*} = \frac{2}{ab} \int_{-a/2}^{a/2} \int_{-b/2}^{b/2} \overset{(1)}{H_x^*} \cos\pi x/a \, dx \, dy \qquad \text{(B-55)}$$

Substitution of equation (B-51) in (B-53) and the resulting expression in (B-55) as well as evaluation of the integrals with respect to x and y (see (B-55)) yields

$$\overset{(1)}{H_{xo}^*} = \frac{8k_o a}{j\omega\mu_o b} \int_{-\infty}^{\infty} \int_{-\infty}^{\infty} I \, d\kappa_x \, d\kappa_y \qquad \text{(B-56a)}$$

where

$$I=\frac{1}{(\kappa_x^2+\kappa_y^2)}\left[\frac{\delta_1}{\Delta_1}\kappa_y^2+\frac{\delta_2}{\Delta_2}\kappa_x^2\right]\frac{\cos^2\kappa_x a/2\sin^2\kappa_y b/2}{(\pi^2-\kappa_x^2a^2)^2\kappa_y^2} \qquad \text{(B-56b)}$$

Noting that the aperture admittance Y is the ratio of H_{xo}^{*} and E_{yo}^{*} (the latter is unity as defined by equation (B-48), see equations (B-43-45) and accompanying discussions), one obtains

$$Y=G+jB=H_{xo}^{*(1)} \qquad \text{(B-57)}$$

which is given by (B-56a, b). Y_o, the admittance of the wave guide for the dominant mode is given by

$$Y_o=-\sqrt{k_o^2-\pi^2/a^2}/\omega\mu_o \qquad \text{(B-58)}$$

k_o, μ_o are the wave number (propagation constant) and the permittivity of the free space. The normalized admittance of the aperture is, therefore, given by

$$y=g=ib=\frac{Y}{Y_o}=-\frac{H_{xo}^{*(1)}\omega\mu_o}{\sqrt{k_o^2-\pi^2/a^2}} \qquad \text{(B-59)}$$

$H_{xo}^{*(1)}$ is given by (B-56). Other quantities of interest are given below.

Reflection Coefficient

$$R_c=(1-y)/(1+y)=\Gamma e^{i\phi} \qquad \text{(B-60)}$$

ϕ is the phase angle

Γ is the magnitude

Voltage Standing Wave Ratio (dB)

$$VSWR=20\log_0((1-\Gamma)/(1+\Gamma)) \qquad \text{(B-61)}$$

The integral in (B-56a) can be converted to a sum of two infinite series by the use of calculus of residues. The residues have to be evaluated at the zeroes of Δ_1 and Δ_2. This procedure is imperative when the materials have zero loss tangents. If the loss tangents are not zero, the integral can be evaluated numerically. For this purpose, the following transformations may be utilized along with the property that the integrand is even in κ_x and κ_y.

$$\kappa_x = k_o \kappa \cos\theta$$

$$0 < \kappa < \infty \quad ; \quad 0 \le \theta \le \pi/2$$

$$\kappa_y = k_o \kappa \sin\theta \qquad \text{(B-62)}$$

$$\kappa = \eta R/(1-R) \qquad ; 0 \le R \le 1$$

η = a chosen multiplier

The integral can then be written as follows. The last expression uses a quadrature formula, w_ℓ and w'_m being the weights.

$$\int_{-\infty}^{\infty}\int_{-\infty}^{\infty} I(\kappa_x,\kappa_y)\,d\kappa_x\,d\kappa_y = 4k_o^2\int_0^{\infty}\int_o^{\pi/2} I(\kappa_x,\kappa_y)\,\kappa\,d\theta\,d\kappa$$

$$= 4k_o^2\int_0^1\int_o^{\pi/2} I(k_o\kappa\cos\theta, k_o\kappa\sin\theta)\,\kappa\,\frac{\eta}{(1-R)^2}\,d\theta\,dR \qquad \text{(B-63)}$$

$$= 4k_o^2\sum_{\ell=1}^{L} w_\ell \sum_{m=1}^{M} w'_m\, I(k_o\kappa_\ell\cos\theta_m, k_o\kappa_\ell\sin\theta_m)\,\frac{\kappa_\ell\eta}{(1-R_\ell)^2}$$

where $\kappa_\ell = \dfrac{\eta R_\ell}{1-R_\ell}$ $\ell = 1,....L$

If one uses trapezoidal rule withequidistant integration points in the domains ($0 \le R \le 1$ and $0 \le \theta \le \pi/2$), then

$$R_\ell = \ell/(L+1) \quad ; \qquad \ell = 1,2,...L$$

$$\theta_m = \frac{(m-1)\pi}{2(M-1)} \quad ; \qquad m = 1,2,....M \qquad \text{(B-64)}$$

$$w_\ell = \frac{1}{(L+1)}$$

$$w'_\ell = \pi/4(M-1) \quad m = 1, M$$

$$= \pi/2(M-1) \quad 2 \le m \le M-1$$

It may be noted that the points $R = 0$ and 1 ($\kappa = 0$ and ∞) are omitted in the quadrature formula, since the value of the integrand is zero at these points.

The expression I in (B-63) can be written in the following form in terms nondimensionalized quantities

$$k_o^2 I = \left(\frac{\delta_1}{\Delta_2}\cos^2\theta + \frac{\delta_2}{\Delta_2}\sin^2\theta\right) \frac{\cos^2(\kappa a'\cos\theta/2)\sin^2(\kappa b'\sin\theta/2)}{(\pi^2 - \kappa^2 a'^2\cos^2\theta)^2 \kappa^2\sin^2\theta} \quad \text{(B-65)}$$

$$a' = k_o a,\ b' = k_o b \quad \text{(B-66)}$$

Closed form expressions of δ_α and Δ_α (α = 1,2) appearing in 56(b) and (65) are given below for a few cases. The following notations are used in the expressions (subscript denotes the layer or backing medium p).

$$\beta_p = \frac{\mu_p \lambda_p}{\mu_o \varepsilon_p} \quad \text{for } \alpha = 1 \quad \text{(B-67)}$$

$$= \frac{\mu_p}{\mu_o \lambda_p} \quad \text{for } \alpha = 2 \quad \text{(B-68)}$$

$$C_p = \cos(k_o \lambda_p h_p) \quad \text{(B-69)}$$

$$S_p = \sin(k_o \lambda_p h_p) \quad \text{B-70)}$$

The expressions which follow are applicable to α = 1 and 2, but appropriate values of β_p (B-67) for $\alpha = 1$ and (B-68) for $\alpha = 2$ have to be used.

A. Single Layer (p=1) Backed by a Half Space (p=2)

$$\delta_\alpha = \beta_1 C_1 + j\beta_2 S_1$$
$$\Delta_\alpha = -\beta_1^2 S_1 + j\beta_2\beta_1 C_1 \quad \text{(B-71a,b)}$$

For a single layer with conductor backing, the terms with $j\beta_2$ have to be omitted.

B. Two Layers (p=1,2) Backed by a Half Space (p=3)

$$\delta_\alpha = \beta_1\beta_2 C_1 C_2 - \beta_2^2 S_1 S_2 + j\beta_3(\beta_1 C_1 S_2 + \beta_2 S_1 C_2)$$
$$\Delta_\alpha = -\beta_1\beta_2(\beta_1 S_1 C_2 + \beta_2 C_1 S_2) \quad \text{(B-72a,b)}$$
$$+ j\beta_3\beta_1(-\beta_1, S_1 S_2 + \beta_2 C_1 C_2)$$

For two layers with conductor backing, the terms with $j\beta_3$ have to be omitted.

C. Three Layers (p=1,2,3) Backed by a Half Space (p=4)

$$\delta_\alpha = \beta_3\left(\beta_1\beta_2 C_1C_2C_3 - \beta_1\beta_3 C_1S_2S_3 - \beta_2^2 S_1S_2C_3 - \beta_2\beta_3 S_1C_2S_3\right) + j\beta_4\left(\beta_1\beta_2 C_1C_2S_3 + \beta_1\beta_3 C_1S_2C_3 - \beta_2^2 S_1S_2S_3 + \beta_2\beta_3 S_1C_2C_3\right)$$

(B-73a,b)

$$\Delta_\alpha = \beta_1\beta_3\left(\beta_1\beta_3 S_1S_2S_3 - \beta_1\beta_2 S_1C_2C_3 - \beta_2^2 C_1S_2C_3 - \beta_2\beta_3 C_1C_2S_3\right) + j\beta_4\beta_1\left(-\beta_1\beta_2 S_1C_2S_3 - \beta_1\beta_3 S_1S_2C_3 - \beta_2^2 C_1S_2S_3 + \beta_2\beta_3 C_1C_2C_3\right)$$

For three layers with conductor backing, the terms with $j\beta_4$ have to be omitted.

D. Four Layers (p-1,2,3,4) Backed by a Half Space (p-4)

$$\begin{aligned}\delta_\alpha = {} & \beta_4\left[\beta_2\left(\beta_1C_1C_2 - \beta_2S_1S_2\right)\left(\beta_3C_3C_4 - \beta_4S_3S_4\right)\right. \\ & \left. - \beta_3\left(\beta_1C_1S_2 + \beta_2S_1C_2\right)\left(\beta_3S_3C_4 + \beta_4C_3S_4\right)\right] \\ & + j\beta_5\left[\beta_2\left(\beta_1C_1C_2 - \beta_2S_1S_2\right)\left(\beta_3C_3C_4 + \beta_4S_3C_4\right)\right. \\ & \left. + \beta_3\left(\beta_1C_1S_2 + \beta_2S_1C_2\right)\left(\beta_4C_3C_4 - \beta_3S_3S_4\right)\right]\end{aligned}$$

(B-74a,b)

$$\begin{aligned}\Delta_\alpha = {} & \beta_1\beta_4\left[-\beta_2\left(\beta_1S_1C_2 + \beta_2C_1S_2\right)\left(\beta_3C_3C_4 - \beta_4S_3S_4\right)\right. \\ & \left. + \beta_3\left(\beta_1S_1S_2 - \beta_2C_1C_2\right)\left(\beta_3S_3C_4 + \beta_4C_3S_4\right)\right] \\ & + j\beta_5\beta_1\left[-\beta_2\left(\beta_1S_1C_2 + \beta_2S_2C_1\right)\left(\beta_3C_3S_4 + \beta_4S_3C_4\right)\right. \\ & \left. - \beta_3\left(\beta_1S_1S_2 - \beta_2C_1C_2\right)\left(\beta_4C_3C_4 - \beta_3S_3S_4\right)\right]\end{aligned}$$

For four layers with conductor backing the terms with $j\beta_4$ have to be omitted.

It may be noted that the expressions for δ and Δ for more than four layers (without or with a half space backing) are not incorporated in the code written for computation purposes and, hence, the code cannot handle greater than four layers. Similar expressions can be easily obtained and inserted in the code, if desired.

SERIES SOLUTION FOR A RECTANGULAR LAYER BACKED BY A CONDUCTIVE SHEET

As mentioned earlier, the integral (B-53) can be expressed as a sum of two series by the use of the calculus of residues. The residues have to be calculated at the complex zeroes of Δ_1 and Δ_2. For the case of a single layer of thickness h_1, the zeroes of Δ_1 are of interest, which are the roots of

$$\sin(k_o \lambda_1 h_1) = 0 \tag{B-75}$$

and the series solution for normalized guide admittance is given by

$$y_s = \frac{jk_o'}{\sqrt{1-\pi^2/a'^2}} \left[-\cot k_o' h_1' + \frac{4k_o'}{b'h_1'} \sum_{n=0,1}^{\infty} \frac{\alpha_n \exp(-jk_n' b'/2)\sin(jk_n' b'/2)}{k_n'^3} \right] \tag{B-76}$$

where

k_n' = $\left[\varepsilon_r - \pi^2/a'^2 - n^2\pi^2/h_1'^2\right]^{1/2}$ with negative imaginary part; n=0,1,...

ε_r = complex dielectric constant of the lossy plate

j = $\sqrt{-1}$ (B-77)

$[a', b', h_1']$ = [a,b,h_1] k_o, a,b are the wave guide dimensions and h_1 is the plate thickness

k_o = free space wave number

α_n = 1/2 for n=0 and 1 for n>0

The series and the integral have been found to give identical results and are compared in Appendix C with some results available in literature for the single layer case.

SOLUTION FOR A CO-AXIAL CABLE

For a co-axial cable, the aperture is in the form of an annular region bounded by two concentric circles of inner and outer radii a and b, respectively (Figure B-3). In this case, the geometry is referred to a cylindrical coordinate system ρ,ψ (See Figure B-3) and z, where

$$x = \rho\cos\psi \qquad \text{(B-78)}$$
$$y = \rho\sin\psi$$

and we restrict our attention to the case of an axisymmetric electric field incident on the aperture. Thus, in the layered medium

$$E_x = E_\rho(\rho,z)\cos\psi \qquad \text{(B-79)}$$
$$E_y = E_\rho(\rho,z)\sin\psi$$

and

$$H_x = -H_\psi(\rho,z)\sin\psi \qquad \text{(B-80)}$$
$$H_y = H_\psi(\rho,z)\cos\psi$$

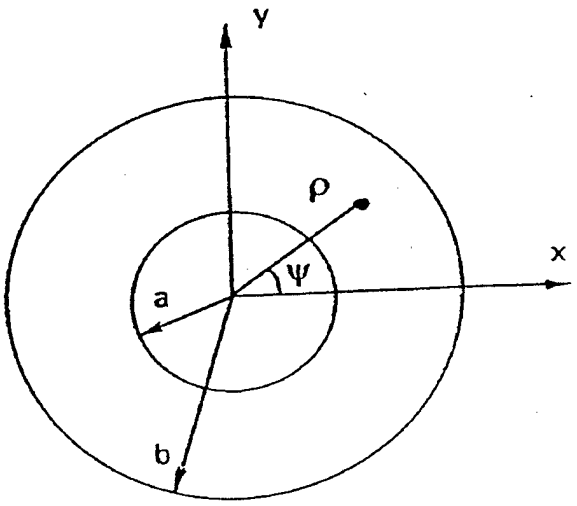

Figure B-3. Co-Axial Cable

Using (B-78) and the first two equations of (B-62) expressing the transform variables κ_x and κ_y in terms of (κ,θ), one can write

$$\exp(j\kappa_x x + j\kappa_y y) = \exp(j k_o \kappa\rho \cos(\psi - \theta)) \tag{B-81}$$

The right hand side of (B-81) can be expressed in a series form given below [3]

$$\exp(j k_o \kappa\rho \cos(\psi - \theta)) = J_o(k_o \kappa\rho) + 2\sum_{n=1}^{\infty} (j)^n J_n(k_o \kappa\rho) \cos n(\psi - \theta) \tag{B-82}$$

Substituting (B-82) in (B-7) and changing the integration, with respect to x and y to that with respect to ρ, ψ, one can evaluate the Fourier transforms of the quantities in (B-79) and (B-80). Performing the integration with respect toψ, the following results are obtained.

$$\begin{aligned}
\bar{E}_x &= 2\pi j \tilde{E}_\rho \cos\theta \\
\bar{E}_y &= 2\pi j \tilde{E}_\rho \sin\theta \\
\bar{H}_x &= -2\pi j \tilde{H}_\psi \sin\theta \\
\bar{H}_y &= 2\pi j \tilde{H}_\psi \cos\theta
\end{aligned} \tag{B-83}$$

where ~ over a quantity indicates its Hankel transform, i.e.,

$$\tilde{E}_\rho = \int_0^\infty \rho E_\rho J_1(k_o \kappa\rho) d\rho \tag{B-84}$$

J_1 denoting the Bessel function of the first kind.

It follows form (B-83) that because of axisymmetry

$$\kappa_x \bar{E}_y - \kappa_y \bar{E}_x = 0$$

and (B-85)

$$\kappa_x \bar{H}_x + \kappa_y \bar{H}_y = 0$$

Therefore, one needs to use only (B-30) to solve the problem. Equation (B-32) is identically satisfied. Using (B-34) for the case with conductor backing, or its modified form for the half space backed case (as discussed in case 2 earlier), one obtains the following relation between the Hankel transforms of the magnetic and electric fields on the top surface of the layered medium.

$$\tilde{h}_\psi^{*(1)} = j\omega\mu_o \tilde{H}_\psi^{*(1)} = -\frac{\delta_1}{\Delta_1} k_o \tilde{E}_p^{*(1)} \tag{B-86}$$

As discussed earlier, a correct solution can be obtained by assuming the electric field at the aperture as a sum of the incident and reflected parts of all possible modes in the co-axial cable (the field is zero outside the aperture), and matching the magnetic fields at the aper-

ture with those obtained by inverting (B-82) (see [2]). For obtaining an approximate solution, when the loss tangents of the layers are not zero (or not too small), one can consider only the dominant incident and reflected modes in the co-axial cable, i.e.,

$$\begin{aligned} \overset{(1)}{E^*_p} &= 1/\rho \qquad a \le \rho \le b \\ &= 0 \qquad \rho < a, \rho > b \end{aligned} \tag{B-87}$$

Substituting (B-87) in (B-84) and performing the integration between ρ=a and ρ=b, one obtains

$$\overset{(1)}{\tilde{E}^*_\rho} = -\left(J_o(k_o\kappa b) - J_o(k_o\kappa a)\right)/k_o\kappa \tag{B-88}$$

Use of this result in (B-86) and inversion of the Hankel transform $\overset{(1)}{\underset{\sim}{H}}_\psi$ in (B-86) result in

$$j\omega\mu_o \overset{(1)}{H^*_\psi} = \int_o^\infty \frac{\delta_1}{\Delta_1} k_o \left(J_o(k_o\kappa b) - J_o(k_o\kappa a)\right) J_1(k_o\kappa\rho)\, d(k_o\kappa) \tag{B-89}$$

Now we note that the magnetic field in the wave guide at the plane of the aperture can be expanded in the form

$$\overset{(1)}{H^*_\psi} = \overset{(1)}{H^*_{\psi o}}/\rho + \sum_{n=1}^{\infty} \overset{(1)}{H^*_{\psi n}} f_n(\rho) \tag{B-90}$$

where $f_n(\rho)$ are the orthogonal mode functions of higher order, satisfying the condition

$$\int_a^b f_n(\rho)\, d\rho = 0 \tag{B-91}$$

Substituting (B-89) in (B-90), integrating with respect to ρ (from a to b) and using (B-91), one obtains

$$\begin{aligned} \overset{(1)}{H^*_{\psi o}} &= \frac{1}{\ell n(b/a)} \int_a^b \overset{(1)}{H^*_\psi}\, d\rho \\ &= -\frac{k_o}{j\omega\mu_o \ell n(b/a)} \int_o^\infty I_1 d\kappa \end{aligned} \tag{B-92}$$

where

$$I_1 = \frac{\delta_1}{\Delta_1 \kappa}\left(J_o(\kappa b') - J_o(\kappa a')\right)^2 \qquad \text{(B-93)}$$

$$a' = k_o a \text{ and } b' = k_o b$$

As discussed in the case of the rectangular wave guide problem, the aperture admittance, Y, is the ratio of $H^{*(1)}_{\psi o}$ and $E^{*(1)}_{\rho o}$ (the latter is chosen as unity in (B-87)) and, therefore,

$$Y = H^{*(1)}_{\psi o} \qquad \text{(B-94)}$$

which is given by (B-92, B-93). Y_o, the admittance of the co-axial cable in the dominant mode, is given by

$$Y_o = G + jB = \frac{k_c}{\omega \mu_c} = \frac{k_o \sqrt{\varepsilon_c}}{\omega \mu_c} \qquad \text{(B-95)}$$

where the quantities with subscript c indicate properties of the core of the co-axial cable. Therefore, the normalized admittance can be written as

$$y = g + jb = \frac{Y}{Y_o} = \frac{j\mu_c}{\mu_o \ell n(b/a)\sqrt{\varepsilon_c}} \int_o^\infty I_1 \, d\kappa \qquad \text{(B-96)}$$

Other quantities of interest, such as reflection coefficient R_c ($y = (1-R_c) / (1+R_c)$), etc., can be computed in the same manner as discussed for the rectangular wave guide problem.

COMPUTER CODE

A computer code ADMIT has been written to evaluate the integrals and results for the case of one term of approximation and non-zero loss tangents. The following input properties are fed in NAMELIST/INPUT.

NF	= No. of Frequencies
FINT	= Starting Value of Frequency in GHZ
DF	= Increment of Frequency in GHZ
EPSR (1), EPSI (I)	= Real and Imaginary Part (Negative) of Dielectric Constant for Material I = 1, NMAT
H (I)	= Thickness of Material Layer I
A, B	= Dimension of Rectangular Wave Guide (A > B) or Inner and Outer Radii of Co-Axial Cable (A < B) in Inches
ITYP	= 1 for Rectangular Wave Guide, = 2 for Co-Axial Cable
NMAT	= Total No. of Materials
NLAY	= No. of Layers of Finite Thickness (limited to ≤4 at this time) (Note that NLAY = NAMT for Conductor Backed Case and NALAY = NMAT-1 for Half-Space Backed Problem)
CSPR, CSPI	= Real and Imaginary Parts of Dielectric Constants of Core for Co-Axial Cable Case
NZET	= No. of Integration Points for Integration (B-63) with Respect to R, Value of L in last of equation (B-63). Note that a similar transformation and quadrative formula is used for evaluation of the integral in (B-92) for co-axial cable.
ETZET	= The multiplier used in (B-62)
MPHI	= No. of Integration Points for integration (B-63) with respect θ, value of M in second of equation (B-64)

NMH	= Sequence No. of Material Layer whose thickness or dielectric constants are to be varied, if desired
NHE	= No. of Thickness Increments of Material Layer NMH as desired
DH	= Thickness Increment Note that frequency is varied (N=1, ... NF) first for each set of layer thicknesses or properties (NH=1, ...NHE).
DEPSR, DEPSI	= Increments in Dielectric Constants of Material NMH as desired
ITN, IDDT	= Print Options for checking purposes. No input is required if such printings are not needed. They are set to zero.
KOPT	= For calculation of changes in the lift-off and orthogonal directions (see Appendix E)
RXX(I), RYY(I); I=1,NF	= Real and Imaginary Parts of Reflection Coefficients for No Defect
RXZ(I), RYZ(I), I=1, NF	= Real and Imaginary Parts of Reflection Coefficients for a Very Small Defect Thickness

All inputs are straightforward except those required for integration. A value of ETZET = 4.0 should be adequate for all cases. It has been found that MPHI of the order 30 or 40 is required for convergence of the integral with respect to θ. Note that although this integration (with respect to θ) does not appear in the case of co-axial cable (eqn (88)), the Bessel functions are evaluated in the code using an integration scheme. MPHI = 30 to 40 was found to be all right for such evaluation. The value of NZET is very crucial and it should be of the order of 12000 when the loss tangents are small (of the order of -0.001). For loss tangents of the order of -0.1, NZETA = 1000 may be adequate. NZETA = 6000 may work for a loss tangent of -0.01. It should be noted that four integrals are evaluated for integration points (NZET, MPHI), (NZET, MPHI/2), (NZET/2, MPHI) and (NZET/2, MPHI/2) and printed for checking convergence.

Output consists of input data, normalized and actual admittances, complex reflection coefficient, its magnitude and phase (in degrees) and VSWR. Plot files are created to give real and imaginary points of admittance (normalized or actual) as well as magnitude and

phase of reflection coefficient versus frequencies or thickness variations for a particular layer. The plot file ADMAT.PLTA contains frequencies (or thicknesses of material NMH if NF=1), real and imaginary parts of normalized admittances and real and imaginary parts of actual admittances in five successive columns. The plot file ADMIT.PLTB has frequencies (or thicknesses of material NMH if NF=1), real and imaginary parts of the reflection coefficients and VSWR (db) and phase (degrees) in five columns. The plot file ADMIT.PLTC contains frequencies, the projections of the reflection coefficient vectors for no defect case on to the lift off vector and the orthogonal component as well as the changes in the projections when there is a defect (from no defect case). The file ADMIT.PLTD has frequencies and the direction cosines of the lift off vector and those of the orthogonal component in five columns.

A list of the code follows.

LISTING OF THE CODE ADMIT

```
C PROGRAM ADMIT
C COMPUTES ADMITTANCES OF RECTANGULAR WAVE GUIDE OR
C CO-AXIAL CABLES WITH FLANGES FACING A LAYERED MEDIUM
C
C PC COMPILE INCREASE STACK SIZE TO HEX C00 = 3K decimal
C ACTUAL COMPILE LINE BELOW: MS-FORTRAN VERSION 5.1
C FL /FPi /F C00 ADMIT.FOR
C PC CHANGE ADMIT.PLTA,ADMIT.PLTB TO ADMIT.PTA,ADMIT.PTB
C     DUE TO FILE EXTENSION LIMITATION OF 3 CHARACTERS
C
C**********************************************************************
C INPUT DATA
C**********************************************************************
C ALL DIMENSIONS A,B AND H IN INCHES, FREQUENCIES IN GHZ
C A,B=RECTANGULAR WAVE GUIDE DIMENSIONS A LARGER
C A,B=INNER AND OUTER RADII OF CO-AXIAL CABLE
C NF=NO OF FRQUECIES, FINT= STARTING VALUE GHZ, DF= INCREMENT GHZ
C EPSR(I), EPSI(I)= REAL AND NEGATIVE IMAGINARY PARTS OF DIELECTRIC
C   CONSTANTS OF MATERIAL I, I=1,NMAT
C CSPR, CSPI= REAL AND IMAGINARY PARTS FOR DIELECTRIC
C   CONSTANT FOR CORE OF CO-AX
C ITYP=1 FOR RECTAGULAR GUIDE, =2 FOR CO-AX
C H(I)=THICKNESS OF MATERIAL I, I=1,NMAT, ANY LARGE NO FOR HALF SPACE
C NLAY=NO OF LAYERS, NMAT=NO OF MTLS
C NMH=MTL NO WHOSE THICKNESS OR PROPERTIES TO BE VARIED
C NHE=NO OF THICKNESS OR PROPERTY INCREMENTS OF THIS MTL AND
C DH,DEPSR,DEPSI=VALUE OF INCREMENTS AT EACH STEP FOR ABOVE
C NLAY=NMAT FOR CONDUCTOR BACKED CASE, NMAT-1 FOR HALF SPACE BACK
C NZET= NO OF INTERVALS FOR INFINITE ZETA INTEGRATION
C ETZET= PARAMETER ZETA=ETZET*R/(1-R), 0<R<1
C MPHI= NO OF INTEGRATION INTERVALS FOR PHI INTEGRATION 0<PHI<PI/2
C BOTH NZET AND MPHI MUST BE EVEN INTEGERS
C
C ITN=1 FOR PRINTINTING VALUE OF LAMBDA AND TAN(AMBDA*H)-CHECK
C IDDT=1 FOR PRINTING FUNCTIONS FOR CHECK
C
C***********************************
C OUTPUT ADMIT.OUT IS SELF EXPLANATORY
C***********************************
C**********************************************************************
C PLOT FILE ADMIT. PTA CONTAINS FREQUENCIES (OR THICNESSES OF MTL NMH IF
C NF=1) AND CORRESPONDING NORMALIZED COMPLIANCES AND ACTUAL COMPLIANCES
C**********************************************************************
C PLOT FILE PTB CONTAINS FREQUENCIES (OR THICKNESS OF MTL NMH IF
C NF=1) AND CORRESPONDING RFLECTION COEFFS, VSWR(DB) AND PHASE(DEG)
C**********************************************************************
      IMPLICIT REAL*8 (A-H,O-Z)
      IMPLICIT INTEGER*4 (I-N)
```

```
C
      COMPLEX*16 AMB(10),AD(2,10),SMY,CPY,TN(10),TOP,BOT,TOP1,
     1BOT1,TOP2,BOT2,DDT(2),SUM1,SUM2,ARGC,XC1,XC2,ZSUM(4),SMULT,
     1EPSC(10),CPSC
C
      DIMENSIONEPSR(10),EPSI(10),H(10),HNON(10),EXRA(10),EXIA(10)
C
      NAMELIST/INPUTNF,FINT,DF,EPSR,EPSI,H,A,B,NZET,MPHI,ETZET,ITYP,
     1NMAT,NLAY,CSPR,CSPI,NMH,NHE,DH,DEPSR,DEPSI,ITN,IDDT
C
      OPEN(UNIT=5,FILE='ADMIT.DAT',STATUS='OLD')
      OPEN(UNIT=6,FILE='ADMIT.OUT',STATUS='UNKNOWN')
      OPEN(UNIT=7,FILE='ADMIT.PTA',STATUS='UNKNOWN')
C PLOT FILE PTA CONTAINS FREQUENCIES (OR THICNESSES OF MTL NMH IF
C NF=1) AND CORRESPONDING NORMALIZEDCOMPLIANCES AND ACTUALCOMPLIANCES
      OPEN(UNIT=8,FILE='ADMIT.PTB',STATUS='UNKNOWN')
C PLOT FILEPTB CONTAINS FREQUENCIES (OR THICKNESS OF MTL NMH IF
C NF=1) AND CORRESPONDINGRFLECTIONCOEFFS, VSWR(DB) AND PHASE(DEG)
      NHE=1
      ITN=0
      IDDT=0
      DH=0.0D0
      DEPSR=0.0D0
      DEPSI=0.0D0
      READ(5,INPUT)
      IF (ITYP.EQ.1) GO TO 1
      WRITE(6,609)CSPR,CSPI
      CALLSQROOT(CSPR,CSPI)
      CPSC=DCMPLX(CSPR,CSPI)
    1 PI=3.1415926D0
      PI2=PI*PI
      SMULT=DCMPLX(0.0D0,1.0D0)
      KMAX=2
      IF(ITYP.EQ.2)KMAX=1
      AN=NZET
      ANI=1.0D0/AN
      AM=MPHI
      AMI=0.5D0*PI/AM
      NZET1=NZET-1
      MPHI1=MPHI+1
      WRITE(6,601)NF,FINT,DF
      WRITE(6,602)A,B
      WRITE(6,603)NZET,MPHI,ETZET
      IF(ITYP.EQ.1) WRITE(6,604)ITYP
      IF(ITYP.EQ.2) WRITE(6,605)ITYP
      WRITE(6,606)NMAT,NLAY
      IF(NHE.EQ.1) GO TO 2
      WRITE(6,620)NHE
      H(NMH)=H(NMH)-DH
      EPSR(NMH)=EPSR(NMH)-DEPSR
      EPSI(NMH)=EPSI(NMH)-DEPSI
```

```
  2 DO 550 IX=1,NHE
    IF(NHE.EQ.1) GO TO 3
    EPSR(NMH)=EPSR(NMH)+DEPSR
    EPSI(NMH)=EPSI(NMH)+DEPSI
    H(NMH)=H(NMH)+DH
  3 WRITE(6,621) IX
    DO 10 I=1,NMAT
    EPSC(I)=DCMPLX(EPSR(I),EPSI(I))
 10 WRITE(6,610)I,EPSR(I),EPSI(I),H(I)
    IF (NMAT.EQ.NLAY) WRITE(6,607)
    IF (NMAT.GT.NLAY) WRITE(6,608)
    FREQ=FINT-DF
    DO 500 N=1,NF
    FREQ=FREQ+DF
    WRITE(6,611)FREQ
C
C     NONDIMENSIONALIZATION
C
    AKP=0.53195D0*FREQ
    BNON=B*AKP
    ANON=A*AKP
    IF(ITYP.EQ.2) GO TO 40
    PIA=PI/ANON
    DIVR=DSQRT(1.0D0-PIA*PIA)
 40 DO 50 I=1,NLAY
 50 HNON(I)=H(I)*AKP
    DO 55 I=1,4
 55 ZSUM(I)=DCMPLX(0.0D0,0.0D0)
C
C     INTEGRATION LOOP FOR ZETA
C
    DO 400 I=1,NZET1
    AI=I
    RI=AI*ANI
    RIM=1.0D0-RI
    RKI=1.0D0/RIM
    WTI=RKI/RIM
    RKI=RKI*RI*ETZET
    RKIS=RKI*RKI
C
C       CALCULATE LAMBDA ETC FOR EACH ZETA
C
    DO 110 L=1,NMAT
    EXR=EPSR(L)-RKIS
    EXI=EPSI(L)
    CALL SQROOT(EXR,EXI)
    EXRA(L)=EXR
    EXIA(L)=EXI
    AMB(L)=DCMPLX(EXR,EXI)
    AD(1,L)=AMB(L)/EPSC(L)
```

```
110 AD(2,L)=1.0/AMB(L)
  LX=NLAY+1
  DO 115K=1,KMAX
  IF(NLAY.EQ.NMAT) AD(K,LX)=DCMPLX(0.0D0,0.0D0)
  IF(NLAY.LT.NMAT) AD(K,LX)=AD(K,LX)*SMULT
115 CONTINUE
  DO 120L=1,NLAY
  AMHI=EXIA(L)*HNON(L)*2.0D0
  IF(AMHI.GT.-30.0D0) GO TO 118
  TN(L)=SMULT
  GO TO 120
118 AMHR=EXRA(L)*HNON(L)
  IF(TN.EQ.0) GO TO 119
  WRITE(6,650)L,AMHR,AMHI
119 CASH=DCOS(AMHR)
  SASH=DSIN(AMHR)
  EAMI=DEXP(AMHI)
  AMP=1.0-EAMI
  AMQ=1.0+EAMI
  TOP1=CASH*AMP+SMULT*SASH*AMQ
  BOT1=SMULT*CASH*AMQ-SASH*AMP
  TN(L)=TOP1/BOT1
  IF(TN.EQ.0) GO TO 120
  WRITE(6,651)I,L,TN(L)
120 CONTINUE
  DO 200K=1,KMAX
  IF(NLAY.GT.1) GO TO 130
  TOP=AD(K,1)
  BOT=-AD(K,1)*AD(K,1)*TN(1)
  IF(NLAY.EQ.NMAT) GO TO 125
  TOP=TOP+AD(K,LX)*TN(1)
  BOT=BOT+AD(K,1)*AD(K,LX)
125 GO TO 190
130 IF(NLAY.GT.2) GO TO 140
  TOP=AD(K,2)*(AD(K,1)-AD(K,2)*TN(1)*TN(2))
  BOT=-AD(K,1)*AD(K,2)*(AD(K,1)*TN(1)+AD(K,2)*TN(2))
  IF(NLAY.EQ.NMAT) GO TO 135
  TOP=TOP+AD(K,LX)*(AD(K,1)*TN(2)+AD(K,2)*TN(1))
  BOT=BOT+AD(K,1)*AD(K,LX)*(AD(K,2)-AD(K,1)*TN(1)*TN(2))
135 GO TO 190
140 IF(NLAY.GT.3) GO TO 150
  TOP1=AD(K,1)*(AD(K,2)-AD(K,3)*TN(2)*TN(3))
  TOP2=AD(K,2)*TN(1)*(AD(K,2)*TN(2)+AD(K,3)*TN(3))
  TOP=(TOP1-TOP2)*AD(K,3)
  BOT1=AD(K,1)*TN(1)*(AD(K,3)*TN(2)*TN(3)-AD(K,2))
  BOT2=AD(K,2)*(AD(K,2)*TN(2)+AD(K,3)*TN(3))
  BOT=(BOT1-BOT2)*AD(K,1)*AD(K,3)
  IF(NLAY.EQ.NMAT) GO TO 145
  TOP1=AD(K,1)*(AD(K,2)*TN(3)+AD(K,3)*TN(2))
  TOP2=AD(K,2)*TN(1)*(AD(K,2)*TN(2)*TN(3)-AD(K,3))
  TOP=TOP+AD(K,LX)*(TOP1-TOP2)
  BOT1=-AD(K,1)*TN(1)*(AD(K,2)*TN(3)+AD(K,3)*TN(2))
```

```
      BOT2=AD(K,2)*(AD(K,2)*TN(2)*TN(3)-AD(K,3))
      BOT=BOT+(BOT1-BOT2)*AD(K,1)*AD(K,LX)
  145 GO TO 190
  150 WRITE(6,612)
      STOP
  190 DDT(K)=TOP/BOT
      IF(DDT.EQ.0) GO TO 200
      WRITE(6,622)I,K,DDT(K)
  200 CONTINUE
      SUM1=DCMPLX(0.0D0,0.0D0)
      SUM2=SUM1
C
C  INTEGRATION OVER PHI FOR ITYP=1 AND BESSEL FUNCTIONS FOR CO-AX
C  FOR EACH ZETA
C
      DO 300 J=1,MPHI1
      PHI=AMI*(J-1)
      PHSS=DSIN(PHI)
      IF(ITYP.EQ.1) GO TO 210
      ARG1=RKI*BNON*PHSS
      ARG2=RKI*ANON*PHSS
      ARG=DCOS(ARG1)-DCOS(ARG2)
      ARGC=DCMPLX(ARG,0.0D0)
      GO TO 250
  210 PHCC=DCOS(PHI)
      ARG1=RKI*ANON*PHCC
      ARG2=DCOS(0.5D0*ARG1)/(PI2-ARG1*ARG1)
      ARG2S=ARG2*ARG2
      IF(J.NE.1) GO TO 212
      ARG1S=0.25D0*BNON*BNON*RKI
      GO TO 215
  212 ARG1=RKI*BNON*PHSS
      ARG2=DSIN(0.5D0*ARG1)/(PHSS*RKI)
      ARG1S=ARG2*ARG2*RKI
  215 ARG=ARG1S*ARG2S
      ARGC=(DDT(1)*PHSS*PHSS+DDT(2)*PHCC*PHCC)*ARG
  250 IF((J.EQ.1).OR.(J.EQ.MPHI1)) ARGC=ARGC/2.0D0
      SUM1=SUM1+ARGC
      JJ=J/2
      JJ2=2*JJ
      IF(J.EQ.JJ2) GO TO 255
      SUM2=SUM2+2.0D0*ARGC
  255 CONTINUE
  300 CONTINUE
      IF(ITYP.EQ.1) GO TO 305
C
C   MODIFICATION REQUIRED FOR CO-AX
C
      XC1=SUM1*SUM1*DDT(1)/RKI
      XC2=SUM2*SUM2*DDT(1)/RKI
      SUM1=XC1
      SUM2=XC2
```

```
C
C   SUM  OVERZETA
C
 305 SUM1=SUM1*WTI
     SUM2=SUM2*WTI
     ZSUM(1)=ZSUM(1)+SUM1
     ZSUM(2)=ZSUM(2)+SUM2
     II=I/2
     II2=2*II
     IF(I.NE.II2) GO TO 400
     ZSUM(3)=ZSUM(3)+2.0D0*SUM1
     ZSUM(4)=ZSUM(4)+2.0D0*SUM2
 400 CONTINUE
     WRITE(6,613)
     DO 405 I=1,4
     ZSUM(I)=ZSUM(I)*ETZET*ANI
     IF(ITYP.EQ.1) GO TO 402
     ZSUM(I)=ZSUM(I)/(AM*AM)
     GO TO 405
 402 ZSUM(I)=ZSUM(I)*AMI
 405 WRITE(6,614)I,ZSUM(I)
C
C   CALCULATE ADMITTANCE, REFLECTION COEFFICIENT
C
     IF(ITYP.EQ.2) GO TO 410
     SMY=SMULT*32.0D0*A*ZSUM(1)/(B*DIVR)
     CPY=-SMY*AKP*DIVR/(FREQ*31.917D0)
     GO TO 420
 410 SMY=SMULT*ZSUM(1)/(CPSC*DLOG(B/A))
     CPY=SMY*AKP*CPSC/(FREQ*31.917D0)
 420 WRITE(6,615)SMY
     WRITE(6,616)CPY
     ARGC=(1.0D0-SMY)/(1.0D0+SMY)
     XR1=DREAL(ARGC)
     XR2=DIMAG(ARGC)
     GAM=DSQRT(XR1*XR1+XR2*XR2)
C
C VAX - VAX FORTRAN RETURNS DEGREES PHZ=DTAN2D(XR2,XR1)
C PC  - MS  FORTRAN RETURNS RADIANS PHZ=DTAN2(XR2,XR1)
C
C    PHZ=DATAN2D(XR2,XR1)
     PHZ=DATAN2(XR2,XR1)
C
C PC - CONVERT RADIANS TO DEGREES PC VERSION ONLY
C
     PHZ = 180.0*PHZ/PI
C
     WRITE(6,617)XR1,XR2,GAM,PHZ
     IF(NF.GT.1) WRITE(7,618)FREQ,SMY,CPY
     IF(NF.EQ.1) WRITE(7,618)H(NMH),SMY,CPY
     RLS=-20.0D0*DLOG(GAM)
     WRITE(6,625)RLS
```

```
      VSWR=20.D0*DLOG10((1.0D0+GAM)/(1.0D0-GAM))
      WRITE(6,626)VSWR
      IF(NF.GT.1)WRITE(8,618)FREQ,XR1,XR2,VSWR,PHZ
      IF(NF.EQ.1)WRITE(8,618)H(NMH),XR1,XR2,VSWR,PHZ
  500 CONTINUE
  550 CONTINUE
      CLOSE(UNIT=5)
      CLOSE(UNIT=6)
      STOP
C
  601 FORMAT(//4X,'INPUT DATA FOR CALCULATION OF NORMALIZED ',
     1'ADMITTANCE AND REFLECTION COEFFICIENTS',///,4X,
     1'NO OF FREQUENCIES=',I4,' STARTING VALUE=',E12.4,'INC=',
     1E12.4,/)
  602 FORMAT(4X,'GUIDE OR CO-AX CABLE DIMENSIONS A,B=',2E12.4,/)
  603 FORMAT(4X,'INTEGRN PARAMETERS NZETA=',I5,
     1'MPHI=',I5,'ETZET=',E12.4,/)
  604 FORMAT(4X,'CASE OF RECTANGULAR GUIDE ITYP=',I4,/)
  605 FORMAT(4X,'CASE OF CO-AXIAL CABLE ITYP=',I4,/)
  606 FORMAT(4X,'NO OF MTLS=',I4,'NO OF LAYERS=',I4,/)
  607 FORMAT(///,4X,'LAYERS ARE BACKED BY CONDUCTING SHEET',///)
  608 FORMAT(///,4X,'LAYERS ARE BACKED BY HALF SPACE',///)
  609 FORMAT(4X,'DIELECTRIC CONST FOR CABLE CORE=',2E12.4,/)
  610 FORMAT(4X,'DIELECTRIC CONST FOR MTL ',I3,' =',2E12.4,
     1'THICKNESS=',E12.4)
  611 FORMAT(///,10X,'RESULTS FOR FRQUENCY IN GHZ=',E12.4,///)
  612 FORMAT(4X,'NLAY.GT.3  EXPRESSION NOT AVAILABLE IN CODE',/)
  613 FORMAT(//,4X,'RESULTS FOR ACCURACY CHECK FOR INTEGRALS',/,
     14X,'1-N*M, 2-N*(M/2), 3-(N/2)*M, 4-(N/2)*(M/2)',//)
  614 FORMAT(4X,'VALUE OF INTEGRAL NO',I3,2E12.4)
  615 FORMAT(//,4X,'CALCULATIONS BELOW ARE FOR ACCURATE VALUE',
     1//,4X,'NORMALIZED ADMITTANCE=',2E12.4,/)
  616 FORMAT(4X,'ACTUAL ADMITTANCE=',2E12.4,/)
  617 FORMAT(4X,'REFL COEF=',2E12.4,'MAGNITUDE=',E12.4,/,
     14X,'PHASE IN DEG=',E12.4,/)
  618 FORMAT(1X,5E12.4)
  620 FORMAT(4X,'NO OF PROPERTY OR LAYUP SETS=',I4,/)
  621 FORMAT(//,4X,'*** RESULTS FOR LAYP SET',I3,' GIVEN BELOW')
  622 FORMAT(4X,'IZET=',I4,' DDT(',I2,')=',2E12.4)
  625 FORMAT(4X,'RL=',E12.4,/)
  626 FORMAT(4X,'VSWR=',E12.4,/)
  650 FORMAT(1X,'LAYER ',I2,'LMDARH,2LMDAIH=',2E12.4)
  651 FORMAT(1X,'IZET',I4,'LAYER',I2,'FNCTN=',2E12.4)
C
C  END OF MAIN PROGRAM
C
      END
C
C  SUBROUTINE SQROOT
C
      SUBROUTINE SQROOT(PREAL,PIMAG)
      IMPLICIT REAL*8 (A-H,O-Z)
```

```
SRSQ=DSQRT(PREAL*PREAL+PIMAG*PIMAG)
SR=DSQRT(SRSQ)
THETA=-DASIN(-PIMAG/SRSQ)
IF(PREAL.LT.0.0D0)THETA=-THETA-3.1415926D0
THETA=THETA/2.0D0
PREAL=SR*DCOS(THETA)
PIMAG=SR*DSIN(THETA)
 RETURN
 END
```

REFERENCES

1. Bakhtiari, S., "Open-Ended Sensors for Microwave NDE of Layered Composite Media", Ph.D Dissertation, Colorado State University, Fort Collins, CO, 1992.
2. Li, C.L., "Determination of Electromagnetic Properties of Materials Using Flanged Open-Ended Co-Axial Probe - Full Wave Analysis", IEEE Transactions on Instrumentation and Measurement, Vol. 44, No. 1, pp. 19-26, February 1995.
3. Gradshteyn, I.S. and Ryzhik, I.M., Table of Integrals Series and Products, Academic Press, New York, 1965.

msc®
Materials Sciences Corporation

APPENDIX C

INTEGRAL AND SERIES SOLUTION RESULTS COMPARED WITH THOSE REPORTED BY BAKHTIARI FOR RECTANGULAR WAVE GUIDES

Suite 250, 500 Office Center Drive
Fort Washington, PA 19034
Tel: 215-542-8400 Fax: 215-542-8401

COMPARISON WITH BAKHTIARI'S RESULTS FOR RECTANGULAR WAVE GUIDE

Figures C1-C6 show the variations of normalized conductances and susceptances for a single layer with the layer thickness d (backed by a conductor) for three values of the dielectric properties at a frequency of 10 GHz. The wave guide dimensions are a = 0.9" and b = 0.4". It may be noted that the present results are the same for series as well as integral solutions. They are compared with those reported by Bakhtiari, S. (Figures 3.3a and b in "Open-Ended Sensors for Microwave Nondestructive Evaluation of Layered Composite Media", Ph.D. Dissertation, Colorado State University, Fort Collins, CO, 1992). It may be noted that although the trend of the results are the same as those from the present calculations, some of the peak values (occurring for some specific values of d) reported by Bakhtiari are lower than those obtained here. The likely reason is that the integrals (and the series) are evaluated in this study with a greater accuracy.

Some cases considered by Bakhtiari, et al (Bakhtiari, S., Ganchev, S.I., and Zoughi, R., "Microwave Swept Frequency Optimization for Accurate Thickness on Dielectric Property Monitoring of Conductor-Backed Composites", Materials Evaluation, p. 740, June 1993) were also studied in the present program. The variation of the phase of the complex reflection coefficient with frequency at x-band (8.2 to 12.4 GHz, the wave guide dimensions are a=0.9", b=0.4") over chosen band widths were studied in the paper. Figure C7 (d=4.28 mm, ε_r = 12.4-j2.4) shows the results over 9.5 to 11.0 GHz, which are the same as those in Figure 3 (measured and calculated) in the paper. Results in Figure C8 (d=1.95, 2 and 2.05 mm, ε_r=20.0-j0.02) are also close to those given in Figure 4 of Bakhtiari's work. Figure C9 (d=2.08, 2.18 mm, ε_r=12.4-j2.4) compare well with the results in Bakhtiari's Figure 5. However, some of the results given in Figure 7 (d=2.0mm) of the paper do not compare with the present calculations shown in Figure C10. Although the measured and calculated values (in the paper) for ε_r=20-j0.02 compare extremely well with those in Figure C10 over the entire frequency range, there are some differences in the two results for ε_r=19-j0.02. For ε_r=21-j0.02, however, the results (only calculated values are given in the paper) are drastically different. ϕ showing a drastic change (from +180° to -180° with increasing frequency) in Bakhtiari's calculations at a frequency of about 8.4 GHz. This change is absent in Figure C10, which show smooth variations of the phase with frequency as well as the dielectric constant. Calculations were performed over wider fre-

quency ranges and various other values of dielectric constants and the results are given in Figures C11-C15. No drastic changes in ϕ were observed except at a frequency range of 16.4-17.2 GHz, but the changes are from -180 to 180 with increasing frequency (similar to that shown in Figure C7) and they were found to occur for all three values of ε_r(19-j0.02, 20-j0.02 and 21-j0.02). It appears that there may be some error in this result reported by Bakhtiari.

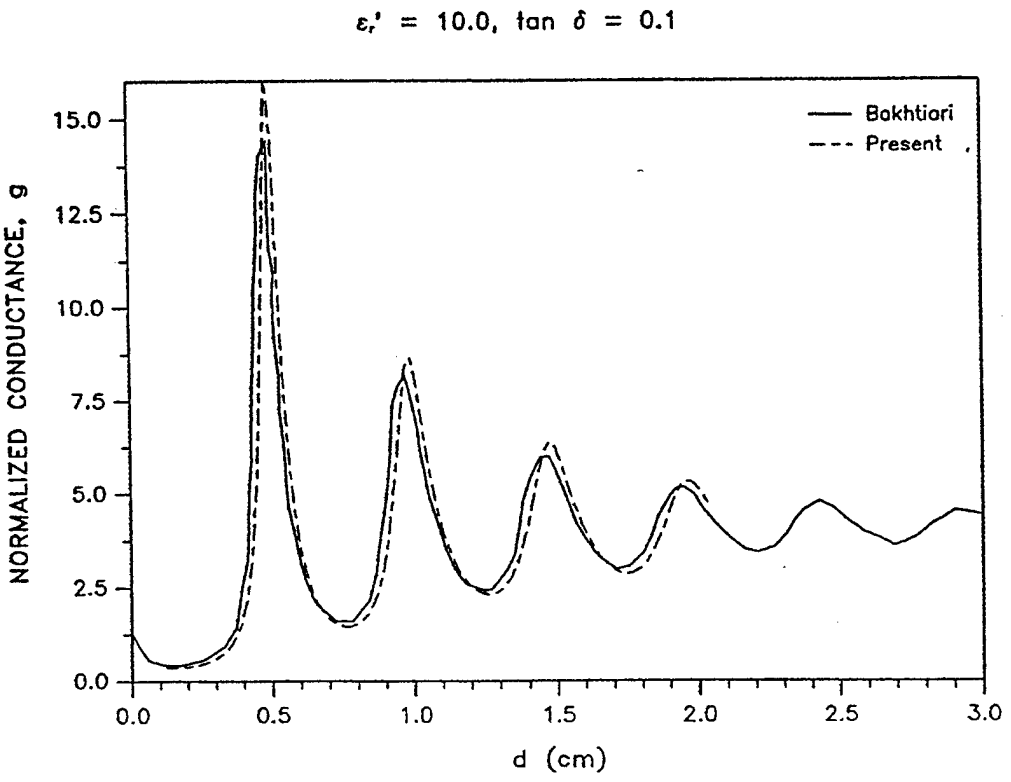

Figure C1. Real Part Normalized Conductance as a Function of Slab Thickness for Lossy Dielectric Materials

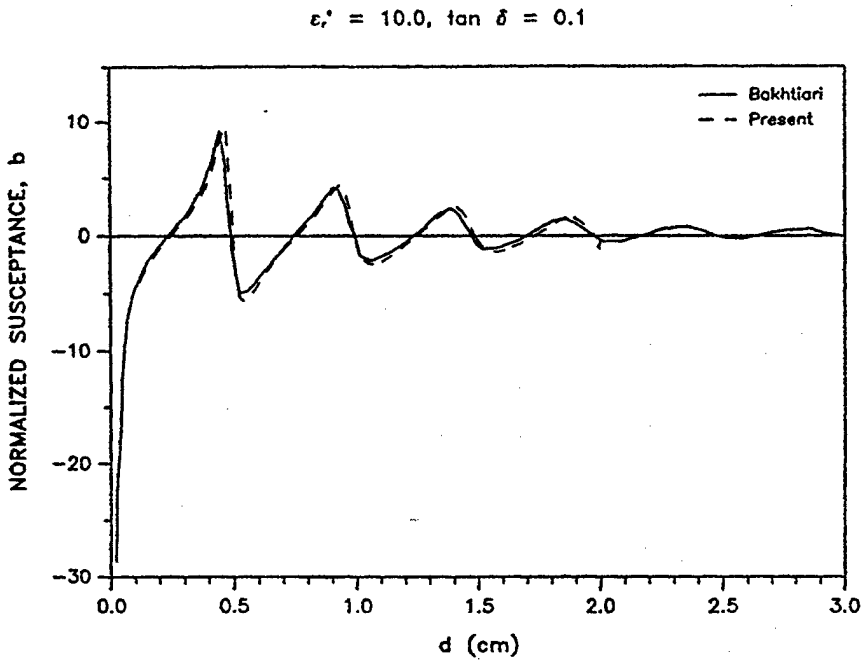

Figure C2. Imaginary Part Normalized Susceptance as a Function of Slab Thickness for Lossy Dielectric Materials

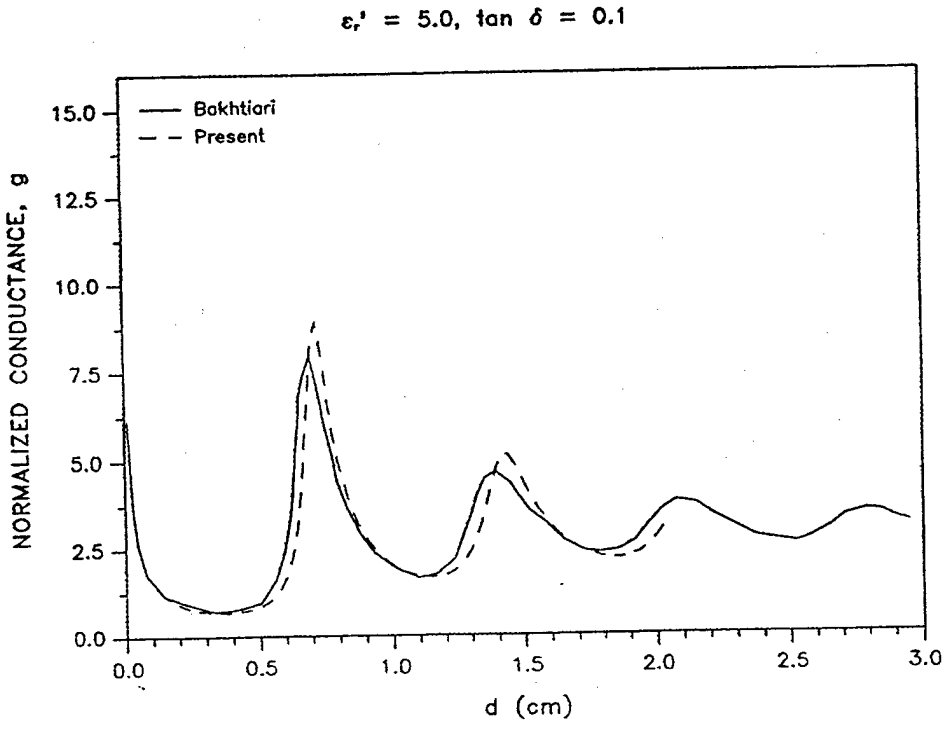

Figure C3. Real Part Normalized Conductance as a Function of Slab Thickness for Lossy Dielectric Materials

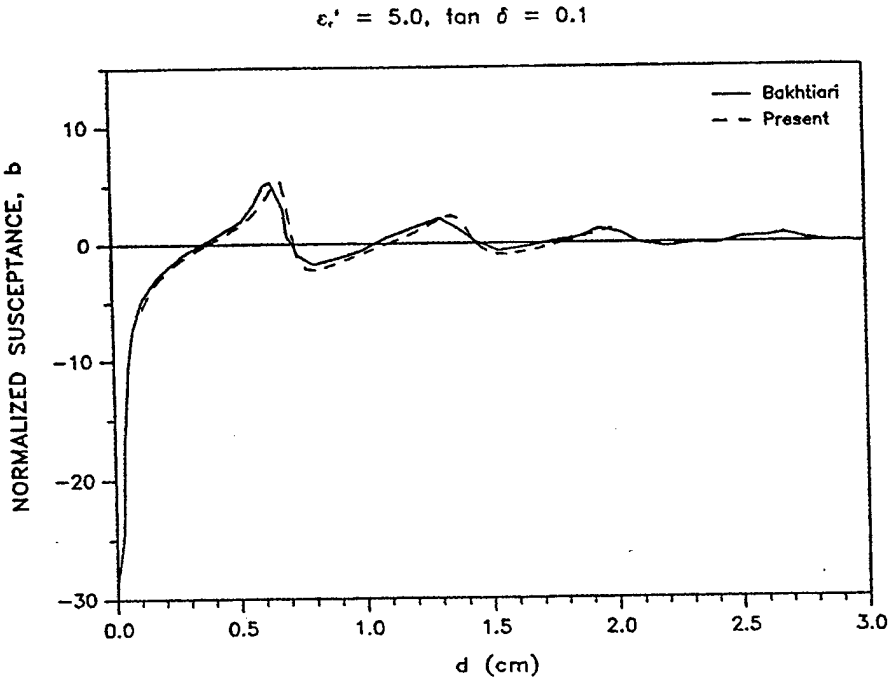

Figure C4. Imaginary Part Normalized Susceptance as a Function of Slab Thickness for Lossy Dielectric Materials

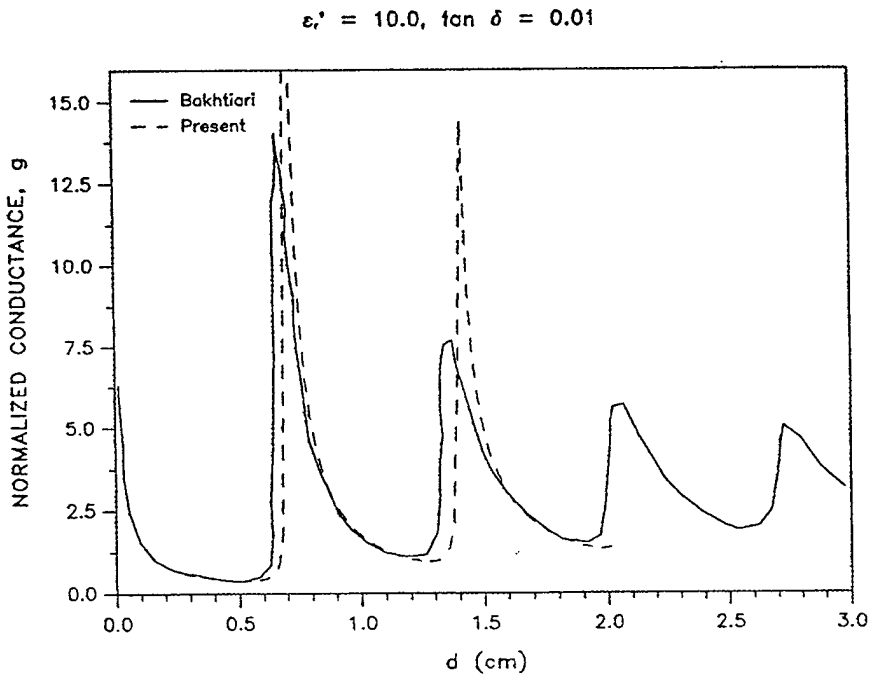

Figure C5. Real Part Normalized Conductance as a Function of Slab Thickness for Lossy Dielectric Materials

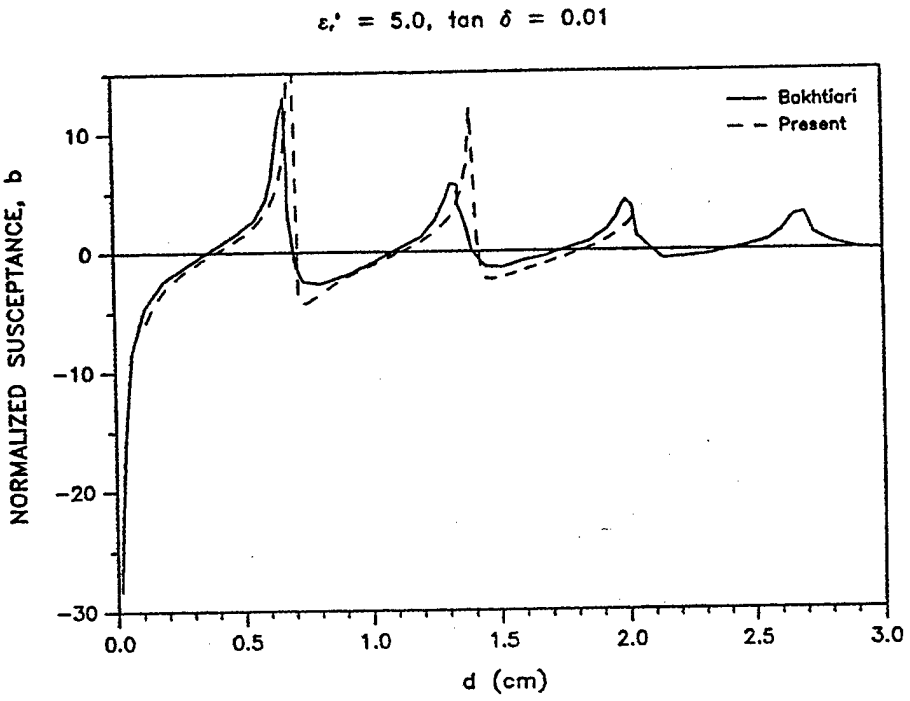

Figure C6. Imaginary Part Normalized Susceptance as a Function of Slab Thickness for Lossy Dielectric Materials

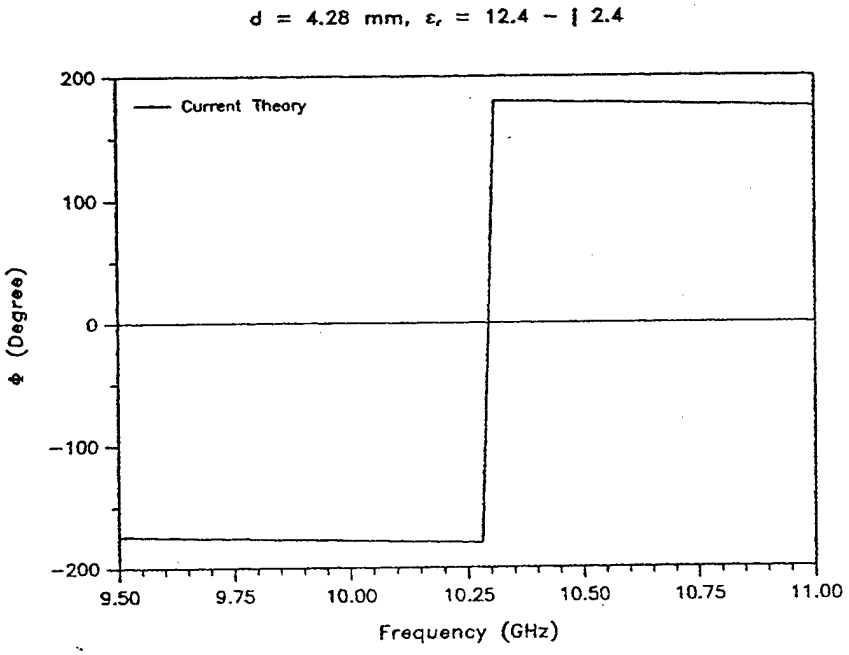

Figure C7. Theoretical Phase for a Lossy Dielectric Sheet

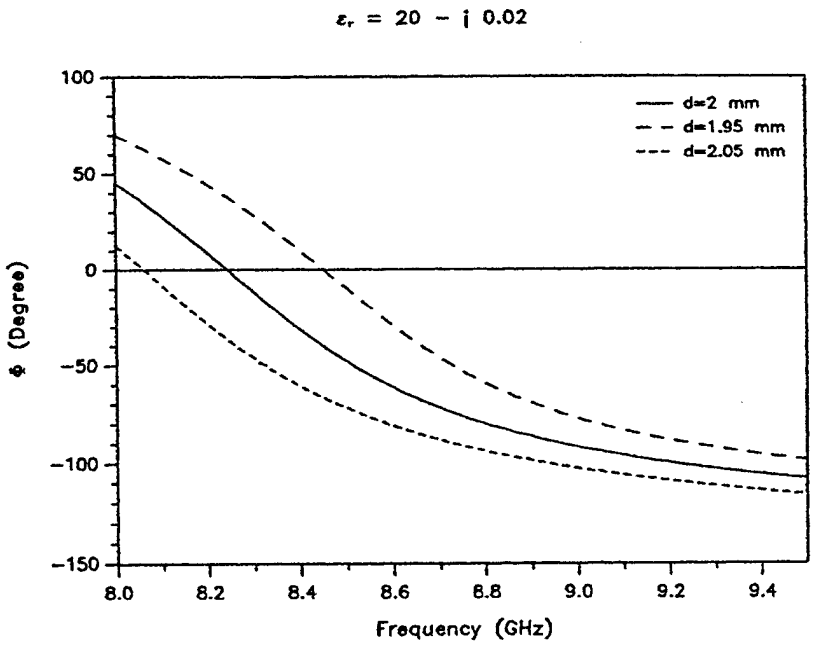

Figure C8. Theoretical Phase for Low-Loss TBC Sheets with Various Thicknesses

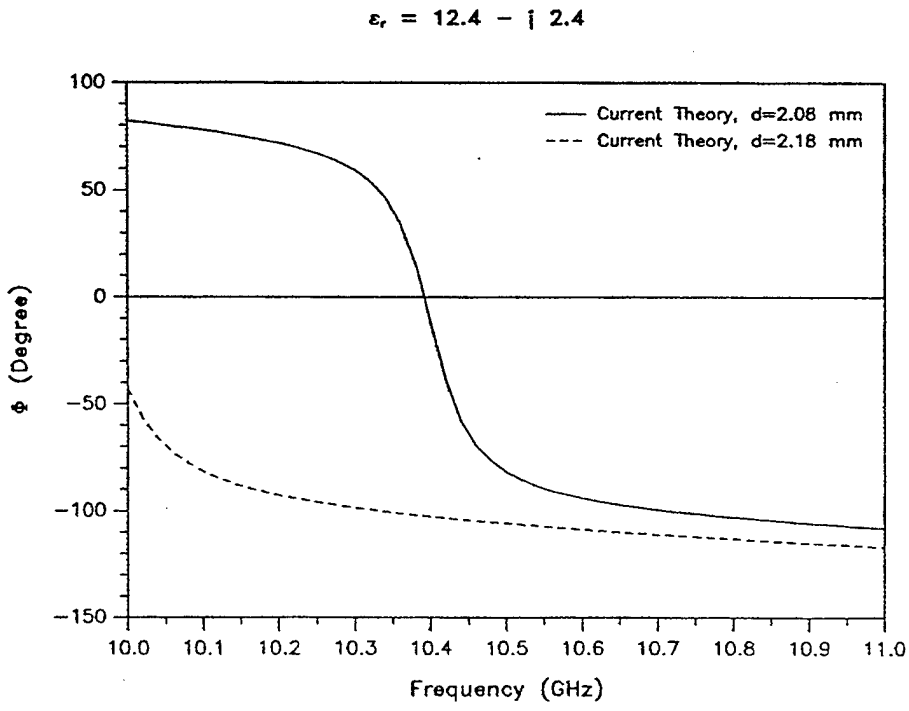

Figure C9. Theoretical Phase for Low-Loss TBC Sheets

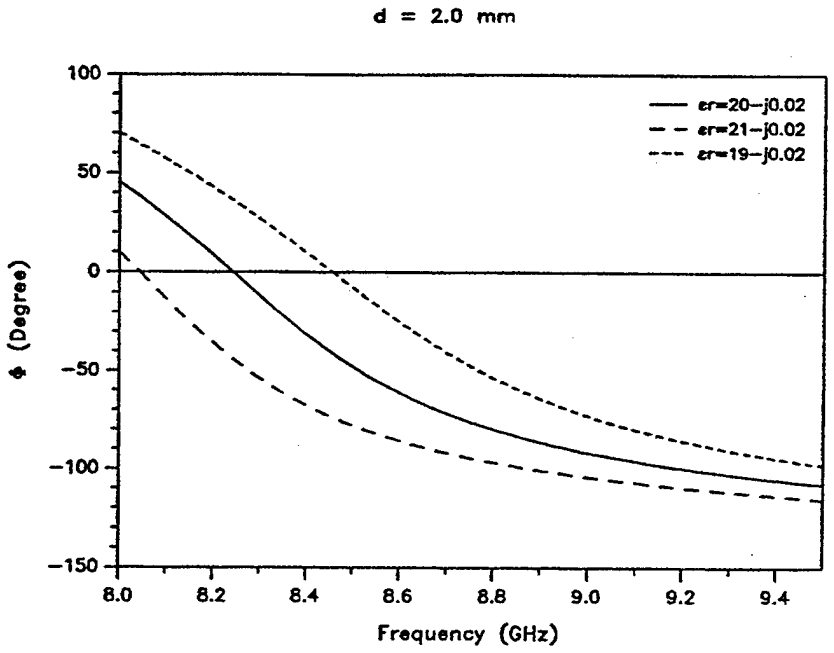

Figure C10. Theoretical Phase for Low-Loss TBC Sheets with Various Permittivities

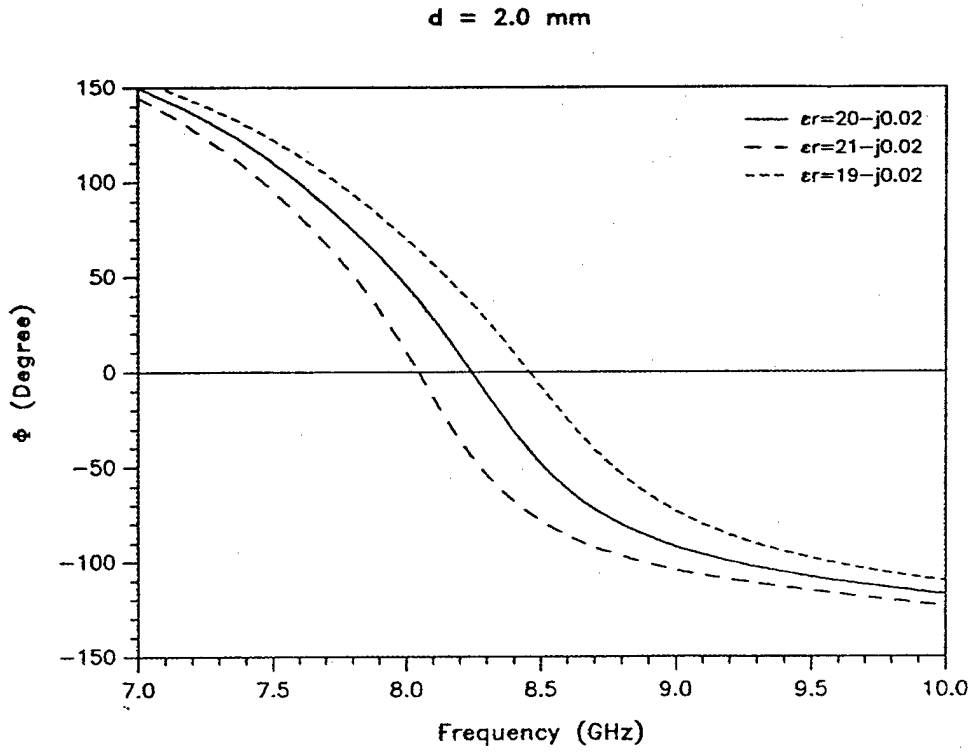

Figure C11. Theoretical Phase for Low-Loss TBC Sheets with Various Permittivities

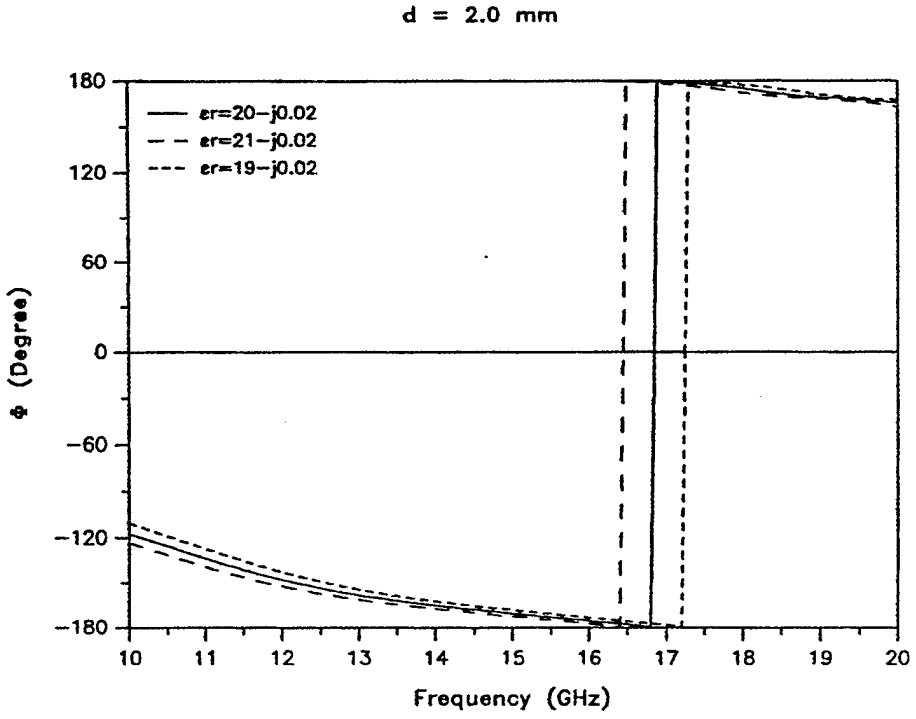

Figure C12. Theoretical Phase for Low-Loss TBC Sheets with Various Permittivities

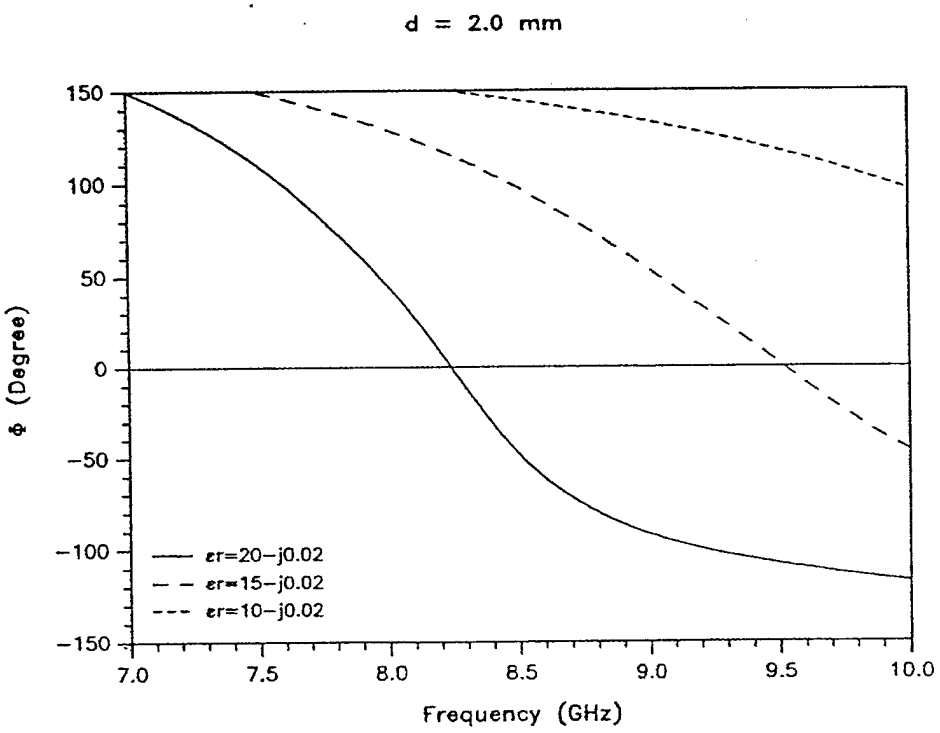

Figure C13. Theoretical Phase for Low-Loss TBC Sheets with Various Permittivities

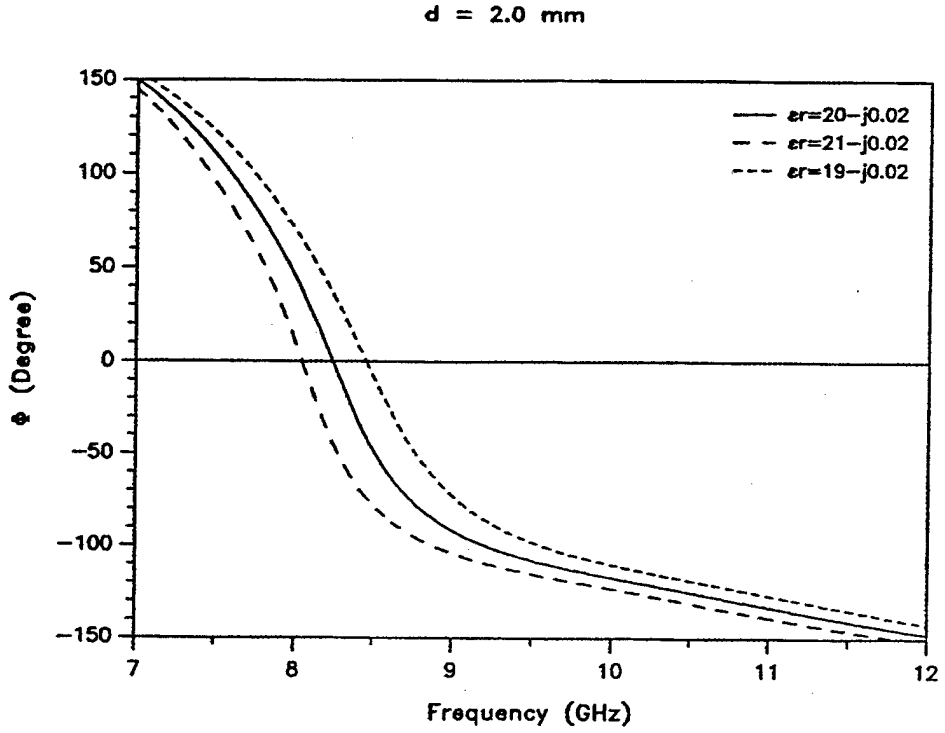

Figure C14. Theoretical Phase for Low-Loss TBC Sheets with Various Permittivities

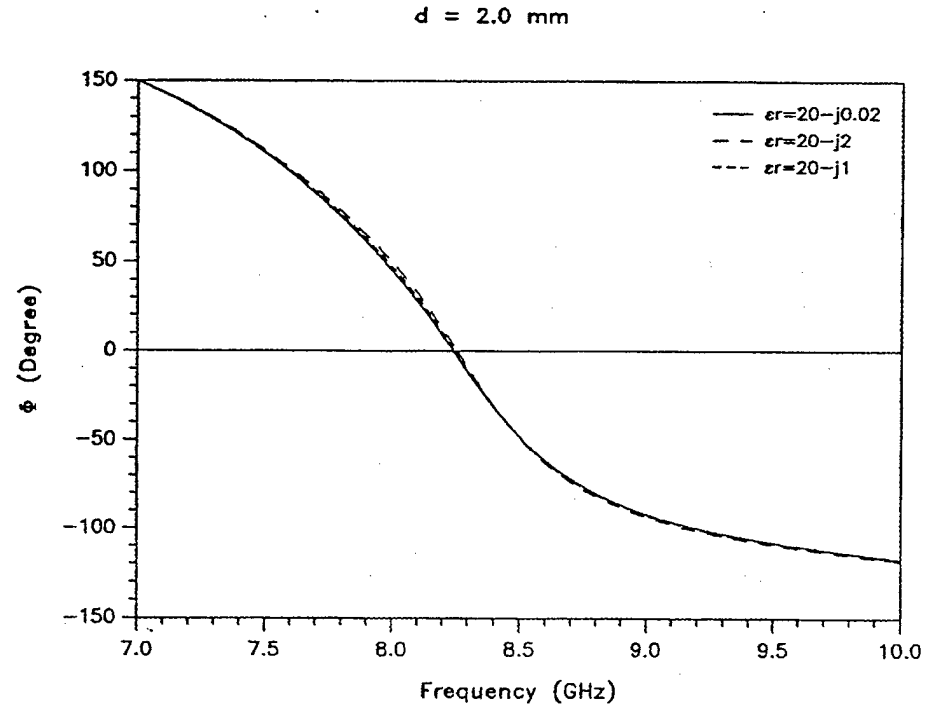

Figure C15. Theoretical Phase for Low-Loss TBC Sheets with Various Permittivities

msc®
Materials Sciences Corporation

APPENDIX D

RESULTS FOR VARYING AIR GAPS IN FRONT OF A DIELECTRIC SLAB OF VARIOUS THICKNESSES, BACKED BY AIR

Suite 250, 500 Office Center Drive
Fort Washington, PA 19034
Tel: 215-542-8400 Fax: 215-542-8401

RESULTS FOR VARYING AIR GAPS BETWEEN A RECTANGULAR WAVE GUIDE AND DIELECTRIC SLABS OF VARYING THICKNESSES BACKED BY AIR

Unavoidable air gaps exist between the microwave sensors and the dielectric slab being interrogated. This appendix gives the results of a systematic study of the effects of air gaps between a rectangular wave guide and the slab thickness d for $\varepsilon_r = 2.8$ and $\tan\delta = .05$. The slab is backed by air. The results (actual admittances in ohm^{-1}) are given in the following figures.

Figure	Plots	d, inch
D1	Conductance vs. air gap and frequency	0.075"
D2	Susceptance vs. air gap and frequency	0.075"
D3	Conductance vs. air gap and frequency	0.125"
D4	Susceptance vs. air gap and frequency	0.125"
D5	Conductance vs. air gap and frequency	0.235"
D6	Susceptance vs. air gap and frequency	0.235"
D7	Conductance vs. air gap and frequency	0.38"
D8	Susceptance vs. air gap and frequency	0.38"
D9	Conductance vs. air gap and frequency	Half Space
D10	Susceptance vs. air gap and frequency	Half Space
D11	Susceptance vs. conductance for varying air gaps and frequencies	0.075"
D12	Susceptance vs. conductance for varying air gaps and frequencies	0.125"
D13	Susceptance vs. conductance for varying air gaps and frequencies	0.235"
D14	Susceptance vs. conductance for varying air gaps and frequencies	0.38"
D15	Susceptance vs. conductance for varying air gaps and frequencies	Half Space

The results show the strong influence of the air gap thickness on the susceptance when the thickness is small (<0.05"). On the other hand, conductance of slabs of small thickness (≤0.125") is not that sensitive to small air gap thicknesses. For slabs of larger thicknesses (≥0.235"), the conductance is also sensitive to small air gaps. Frequency influences the results most for certain ranges of air gaps (usually for small or large values). In general, it appears that smallest possible gap is desirable for obtaining better resolutions for imaging purposes, but slightly higher values (<0.02") may be acceptable.

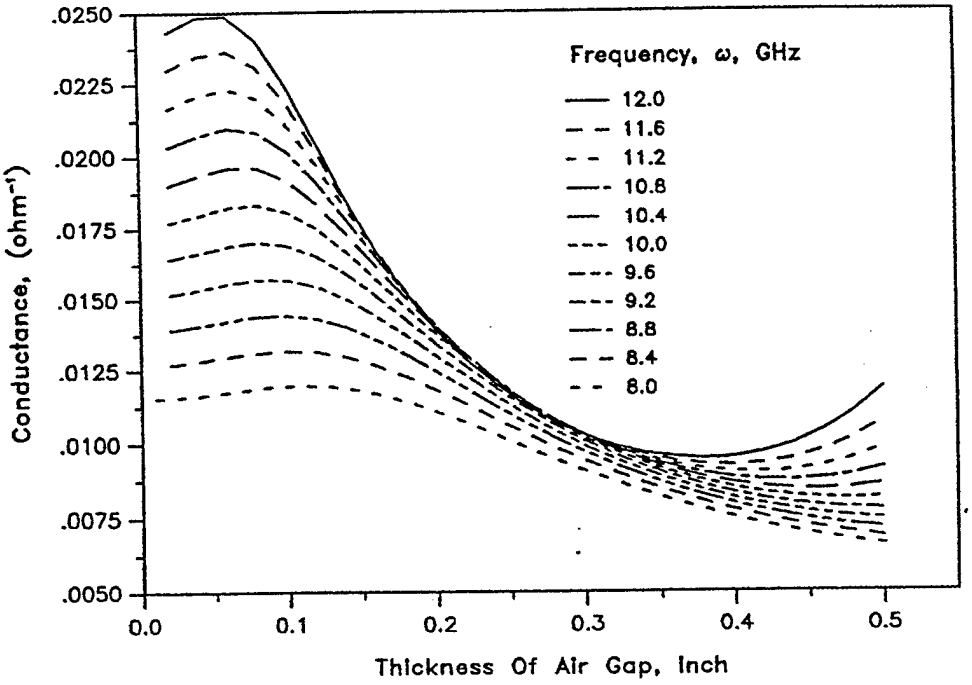

Figure D1. Conductance of a Dielectric Slab of Thickness 0.075 inch and $\varepsilon_r = 2.8$, $\tan\delta = .05$ Backed by Air for Varying Air Gap

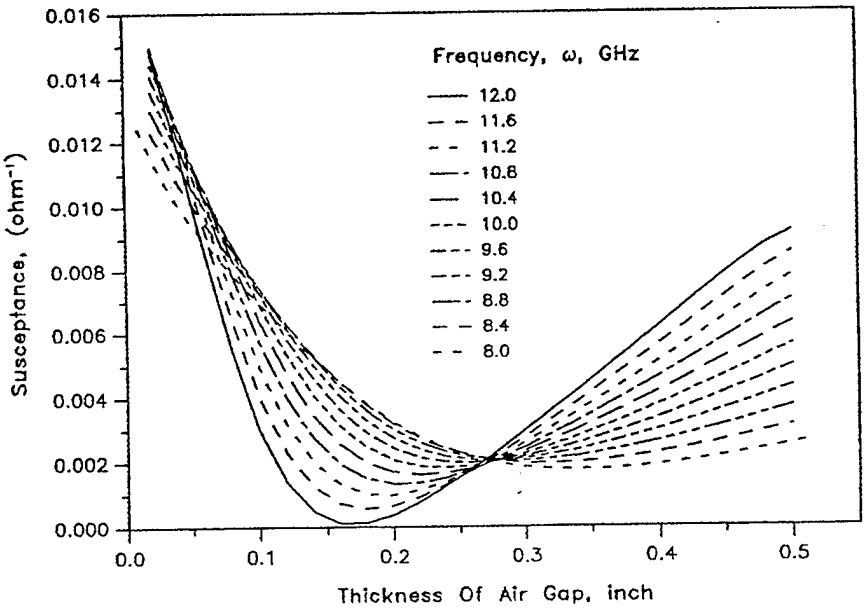

Figure D2. Susceptance of a Dielectric Slab of Thickness 0.075 inch and $\varepsilon_r = 2.8$, $\tan\delta = .05$ Backed by Air for Varying Air Gap

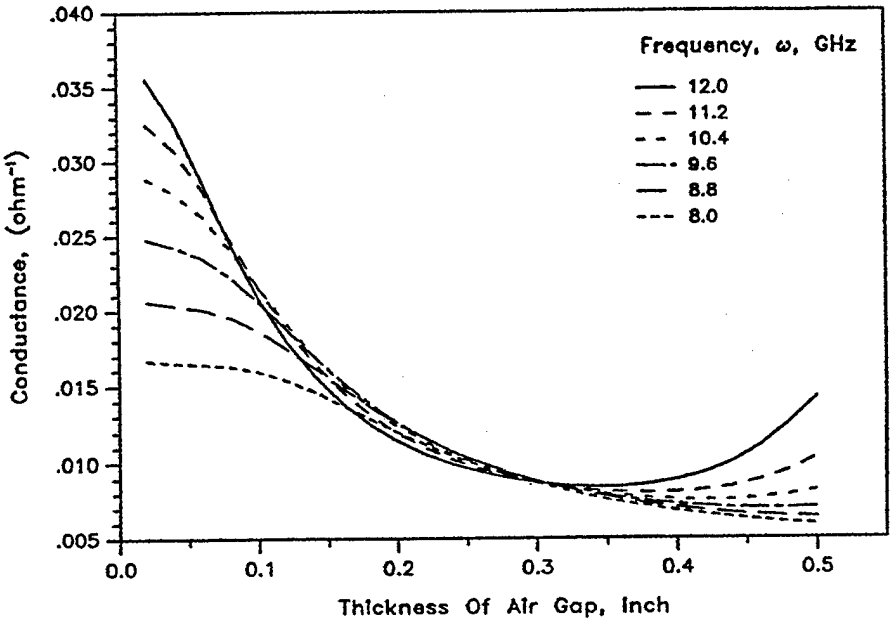

Figure D3. Conductance of a Dielectric Slab of Thickness 0.125 inch and $\varepsilon_r = 2.8$, $\tan\delta = .05$ Backed by Air for Varying Air Gap

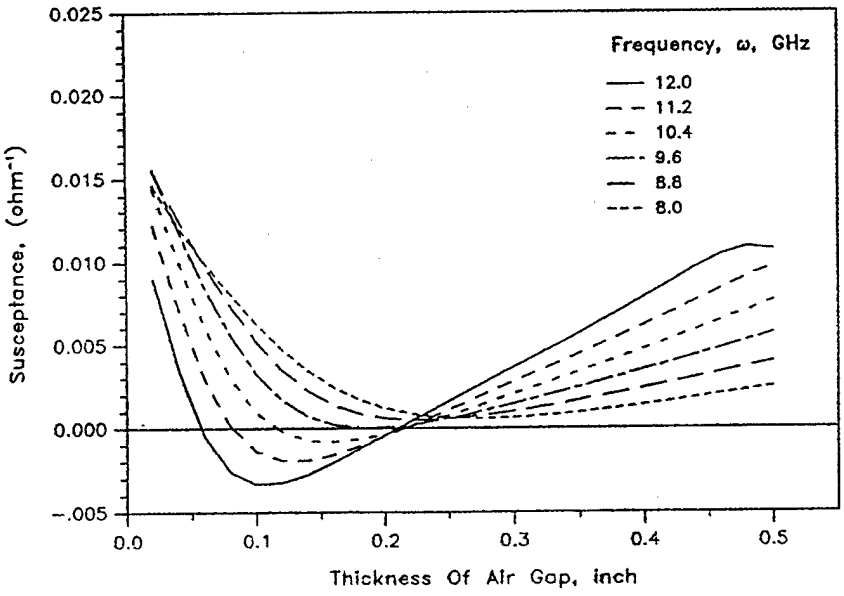

Figure D4. Susceptance of a Dielectric Slab of Thickness 0.125 inch and $\varepsilon_r = 2.8$, $\tan\delta = .05$ Backed by Air for Varying Air Gap

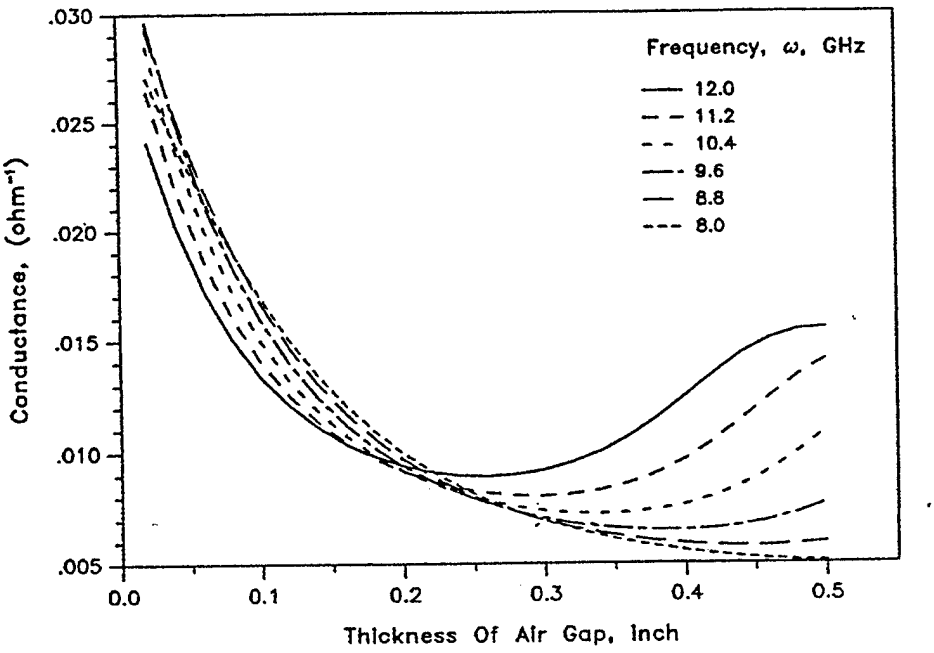

Figure D5. Conductance of a Dielectric Slab of Thickness 0.235 inch and $\varepsilon_r = 2.8$, $\tan\delta = .05$ Backed by Air for Varying Air Gap

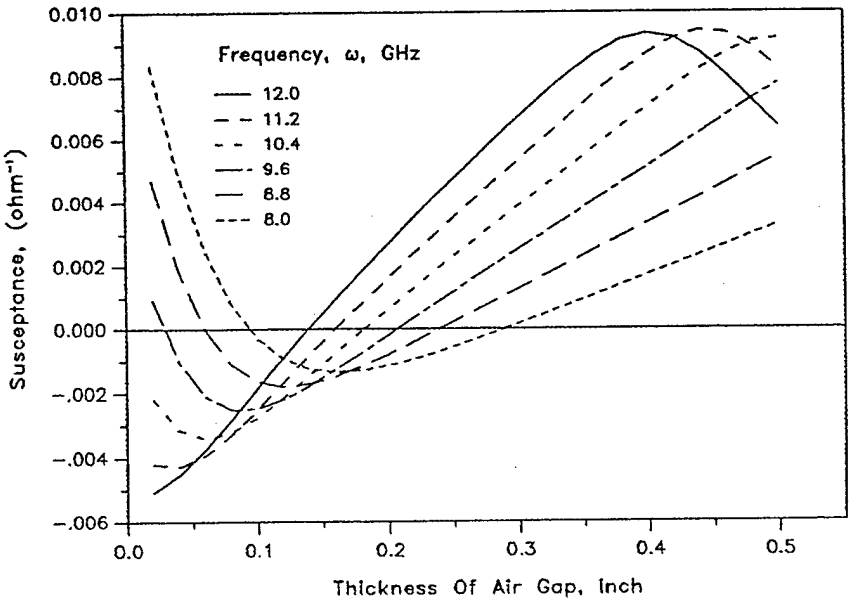

Figure D6. Susceptance of a Dielectric Slab of Thickness 0.235 inch and $\varepsilon_r = 2.8$, $\tan\delta = .05$ Backed by Air for Varying Air Gap

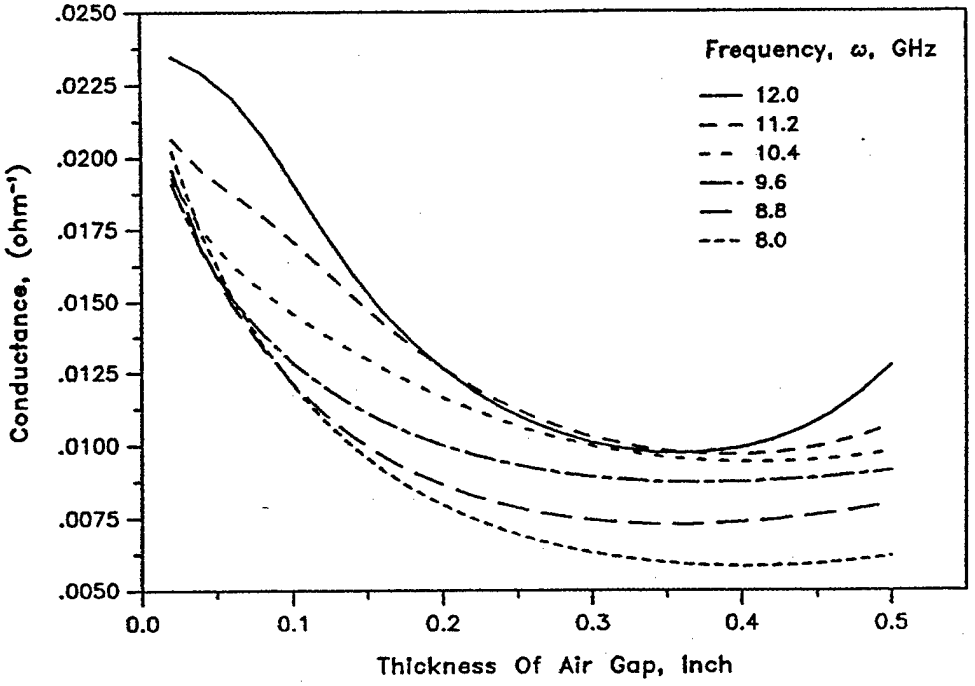

Figure D7. Conductance of a Dielectric Slab of Thickness 0.380 inch and $\varepsilon_r = 2.8$, $\tan\delta = .05$ Backed by Air for Varying Air Gap

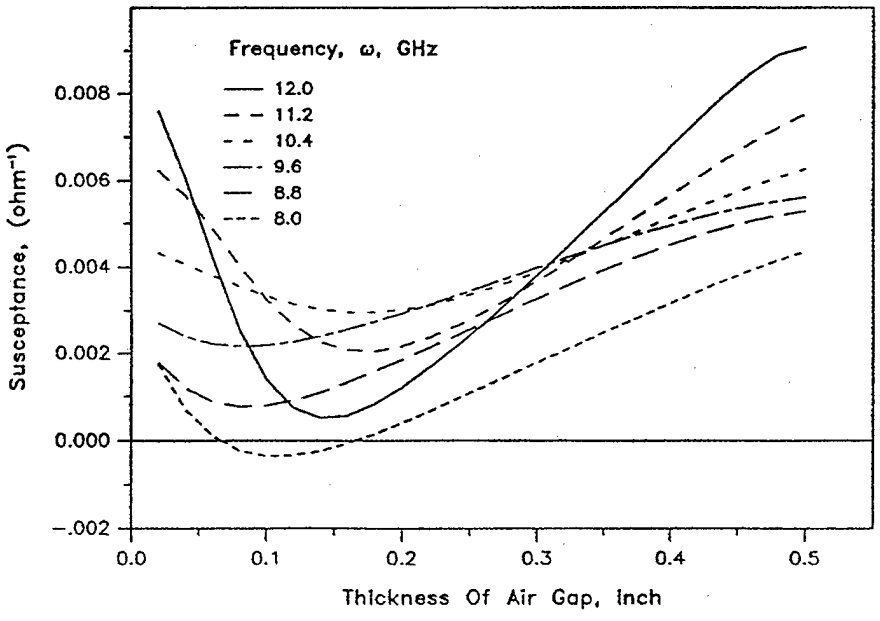

Figure D8. Susceptance of a Dielectric Slab of Thickness 0.380 inch and $\varepsilon_r = 2.8$, $\tan\delta = .05$ Backed by Air for Varying Air Gap

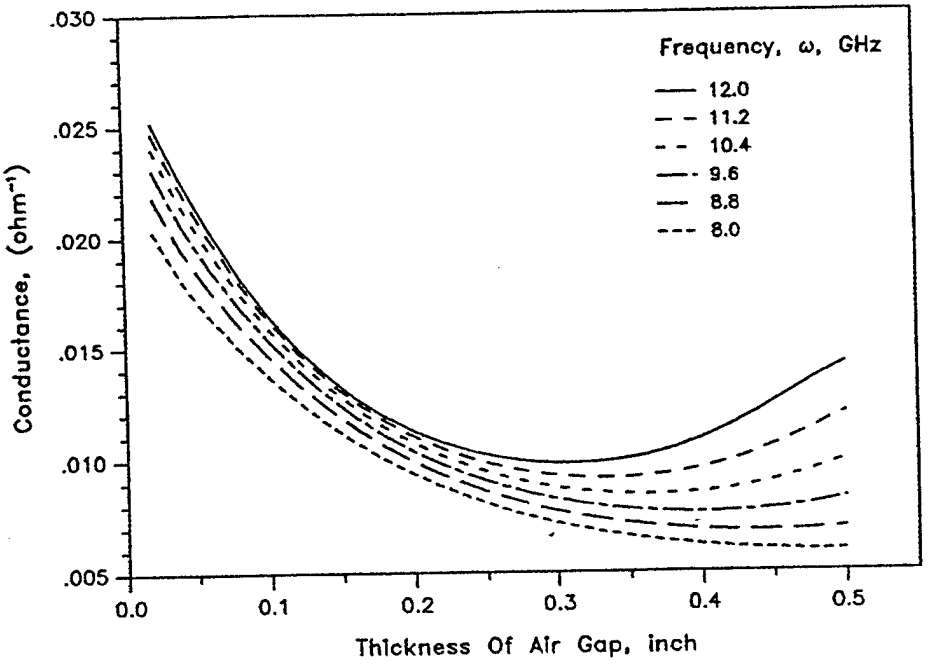

Figure D9. Conductance of a Dielectric Half Space $\varepsilon_r = 2.8$, $\tan\delta = .05$ for Varying Air Gap

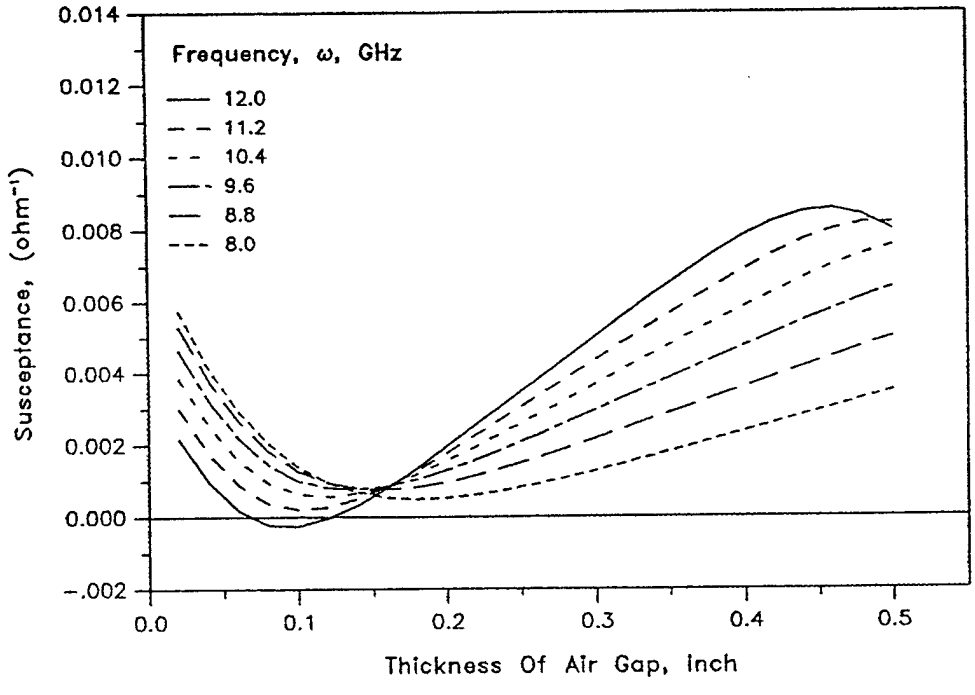

Figure D10. Susceptance of a Dielectric Half Space $\varepsilon_r = 2.8$, $\tan\delta = .05$ for Varying Air Gap

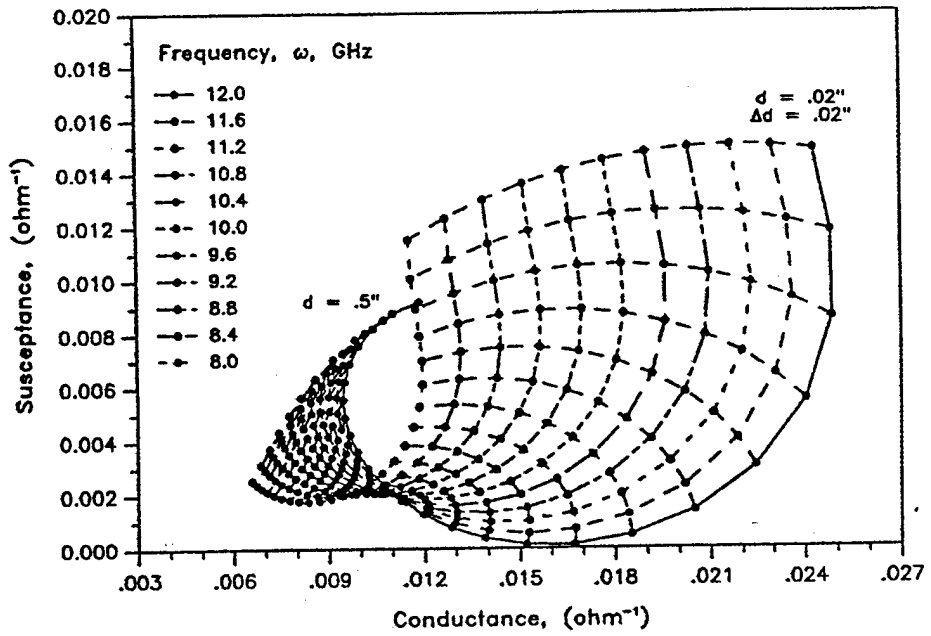

Figure D11. Relationship of Susceptance, Conductance, & Air Gap (d) on a Dielectric Slab of Thickness 0.075 inch and $\varepsilon_r = 2.8$, $\tan\delta = .05$ Backed by Air

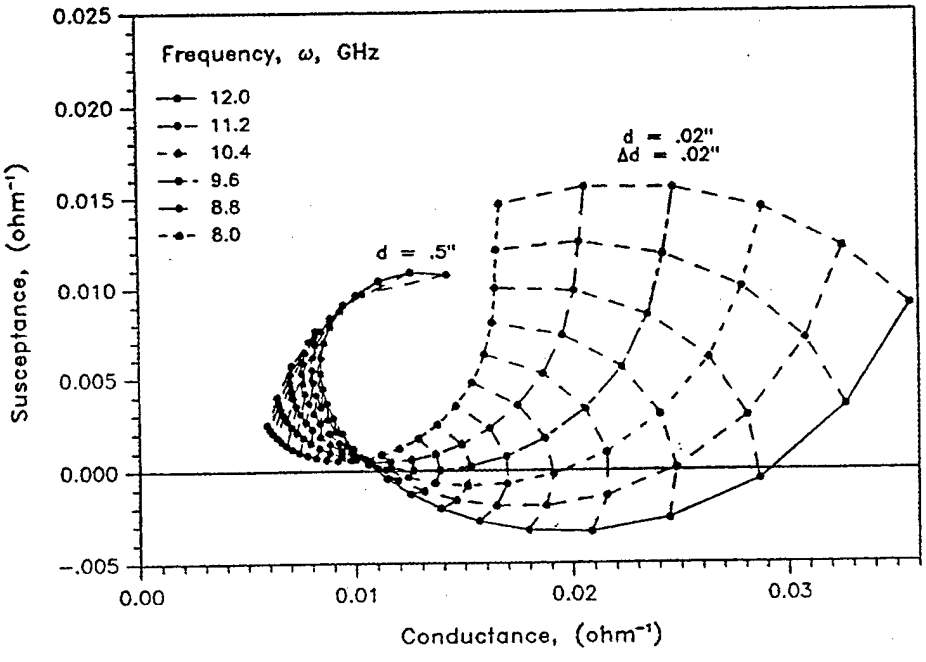

Figure D12. Relationship of Susceptance, Conductance, & Air Gap (d) on a Dielectric Slab of Thickness 0.125 inch and $\varepsilon_r = 2.8$, $\tan\delta = .05$ Backed by Air

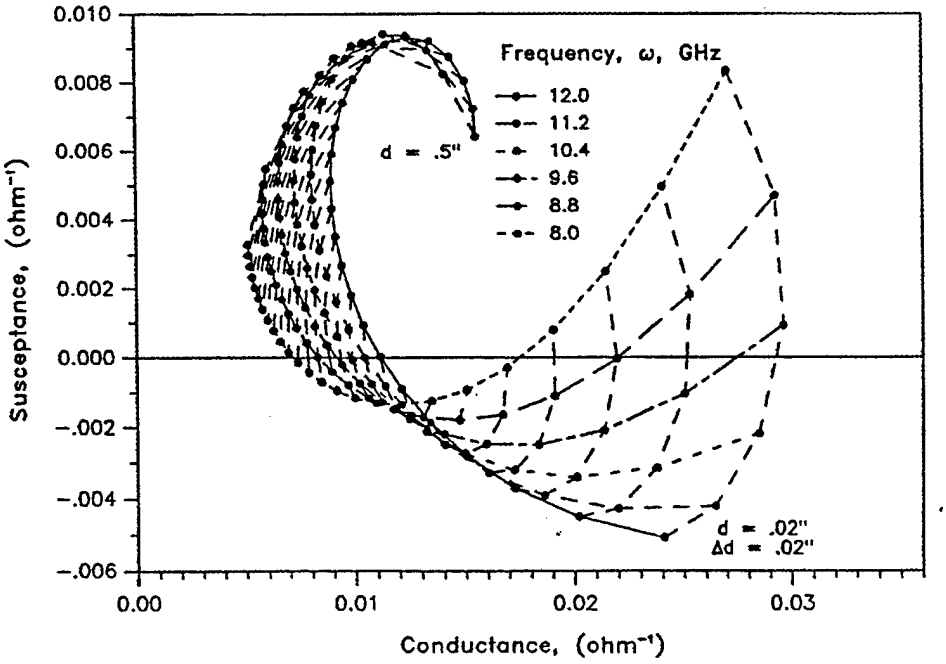

Figure D13. Relationship of Susceptance, Conductance, & Air Gap (d) on a Dielectric Slab of Thickness 0.235 inch and $\varepsilon_r = 2.8$, $\tan\delta = .05$ Backed by Air

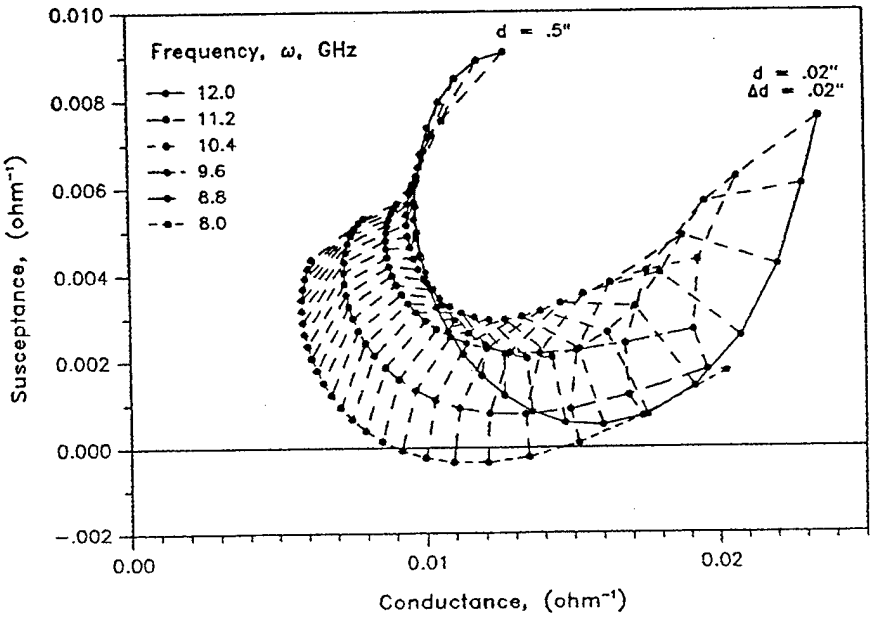

Figure D14. Relationship of Susceptance, Conductance, & Air Gap (d) on a Dielectric Slab of Thickness 0.380 inch and $\varepsilon_r = 2.8$, $\tan\delta = .05$ Backed by Air

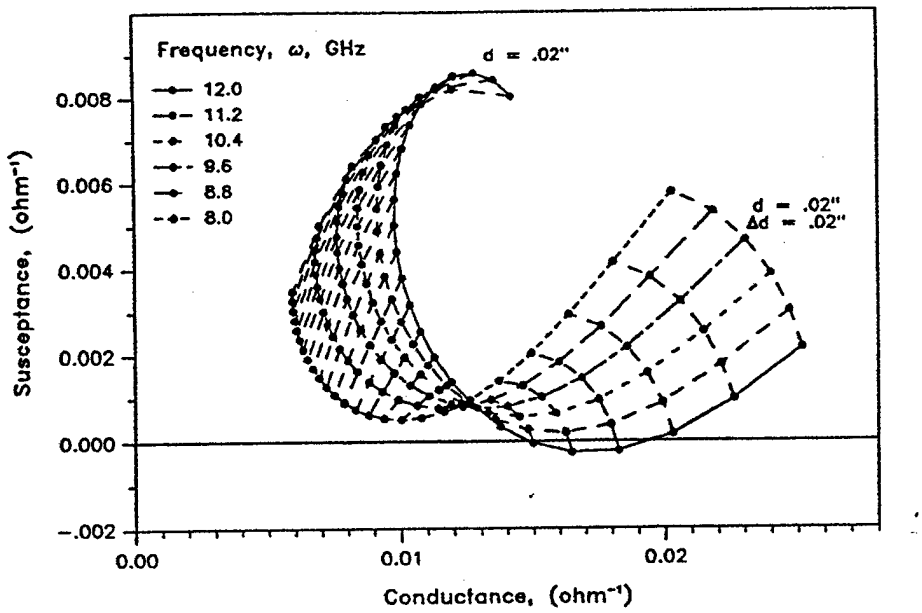

Figure D15. Relationship of Susceptance, Conductance, & Air Gap (d) on a Dielectric Half Space, $\varepsilon_r = 2.8$, $\tan\delta = .05$

msc®
Materials Sciences Corporation

APPENDIX E

EFFECTS OF FREQUENCY ON LIFT OFF

Suite 250, 500 Office Center Drive
Fort Washington, PA 19034
Tel: 215-542-8400 Fax: 215-542-8401

25 Years Advanced Composites Technology

INTRODUCTION

Dielectric properties of layered materials are often influenced by air gaps or delaminations, which may be present between the layers. Use of microwave NDE for detecting the air gap at such delaminations has been suggested by some investigators. In this approach the sensor (a rectangular wave guide) is placed in front of a coupling dielectric sheet, which is backed by the specimen being interrogated. An unintentional air gap is usually present between the coupling material and the specimen surface. This is called the lift-off effect and one first attempts to find the direction of the change in the tip of the vector (complex reflection coefficient) due to small lift-off (air gap). This direction (that of the change) is called the lift-off direction. For the purpose of detecting the presence or absence of a delamination type air gap inside the specimen, the change in the component of the complex reflection coefficient vector, which is orthogonal to the lift-off direction, is normally used, so as to minimize the lift-off effects produced by wobbling of the wave guide and the coupling sheet over the specimen during scanning. At certain frequencies the lift-off is a minimum and the orthogonal component is a maximum. This Appendix describes the results of a parametric study performed to find the frequency ranges which should be used so as to minimize the lift-off effect in support of microwave NDE studies at NSWC.

LIFT-OFF DIRECTION

The lift-off direction is determined by considering the following cases, i.e., the presence of a small air gap c of varying thicknesses and no air gap between the coupling material B (next to the rectangular wave guide) and the sample material D as shown in Figure E1. For this study, the following parameters were chosen.

Region A - x-band wave guide a=0.9", b=0.4"

Region B - Coupling dielectric sheet, thickness = 0.375", ε_r=2.7, tanδ=0.05

Region C - Unintentional air gap of thickness t varied from 0 to 0.02"

Region D - Sample, ε_r=4.5, tanδ=0.05, thickness = 4"

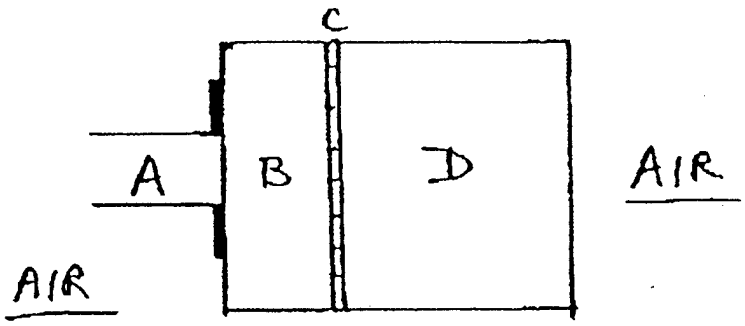

Figure E1. Geometry to Determine the Lift-Off Direction

A - Wave Guide

B - Coupling Material

C - Air Gap

D - Sample

The objective was to find the trajectory of the tip of the reflection coefficient factor (X,Y, R = X+iY) as the unintentional air gap thickness was changed (using the code ADMIT for calculations) and the tangent to this trajectory for zero air gap thickness (t=0). It was found that a line drawn from the tip for zero air gap thickness to that for a gap thickness of t=0.01" is adequate to define the tangent or the lift-off direction. Let

$$RXX, RYY = X,Y \text{ for } t=0$$
$$RXZ, RYZ = X,Y \text{ for } t=0.01" \qquad \text{(E-1)}$$
$$DX = RXZ-RXX$$
$$DY = RYZ-RYY$$

The direction cosines of the lift-off direction is

$$DXX = DX/DL \qquad \text{(E-2)}$$
$$DYY = DY/DL$$
$$DL = (DX^2 + DY^2)^{1/2}$$

The direction cosines of the orthogonal vector (to lift-off vector) is

$$PDX = -DYY \qquad \text{(E-3)}$$
$$PDY = DXX$$

The projection of the reflection coefficient vector for t=0 on to the lift-off direction is

$$RDXZ = RXX \bullet DXX + RYY \bullet DYY \qquad \text{(E-4)}$$

and on to the orthogonal direction is

$$RDPZ = RXX \bullet PDX + RYY \bullet PDY \qquad \text{(E-5)}$$

Note that all the quantities defined above are functions of frequency.

MINIMIZATION OF LIFT-OFF EFFECT

This minimization is desirable to increase the accuracy of prediction of presence of delaminations within the sample D at different locations (Figure E2). The following cases were considered as shown in Figure E2, but the thickness of the unintentional air gap C was chosen as zero.

Distance of air gap in D from C, x = 1", 2", 3"

Air gap thickness δ = 0.005", 0.01", 0.02"

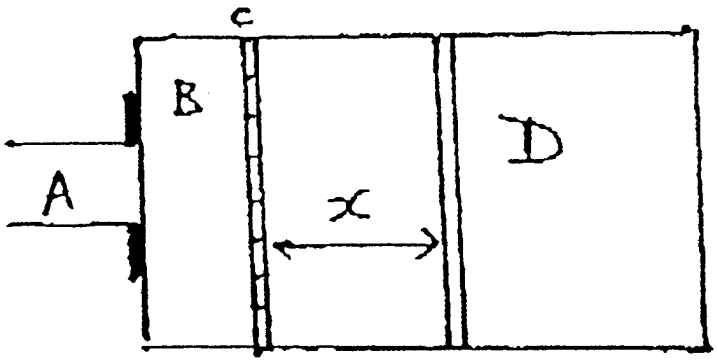

Figure E2. Geometry for Study

A - Wave Guide

B - Coupling Material

C - Unintentional Air Gap is Absent

D - Sample with Delamination

The reflection coefficient vectors (X, Y) for each of these cases were computed using the code ADMIT and their projections on lift-off and orthogonal directions were calculated.

Lift-Off: DRDX =X•DXX + Y•DYY (6)

Orthogonal: DRPD=X•PDX + Y•PDY

Finally, changes of these projections from those for no defect case (equation (E4) and (E5)) were determined.

Lift-Off: DRLF=DRDX - RDXZ

Orthogonal: DRPF=DRPD - RDPZ

RESULTS

Values of DRLF and DRPF for δ = 0.005", 0.01", and 0.02" are plotted against frequency (9 to 11 GHz) in Figures E3, E4, and E5 for the defect locations x=1", 2", and 3", respectively. It may be noted that at the frequencies the orthogonal component DRPF are maximum, the lift-off components DRLF are minimum. As the distance x of the defect from the coupling material is increased, the components reduce in magnitude (an expected effect) and the maximum values are attained at an increasing number of frequencies. The frequencies at which the orthogonal components are maximum should be chosen for interrogation to determine existence of possible delaminations in the sample. Figure E6 shows the variations of the projections of the reflection coefficient vector (RDXZ, RDPZ) for no defect case on to the lift-off and orthogonal directions for various frequencies.

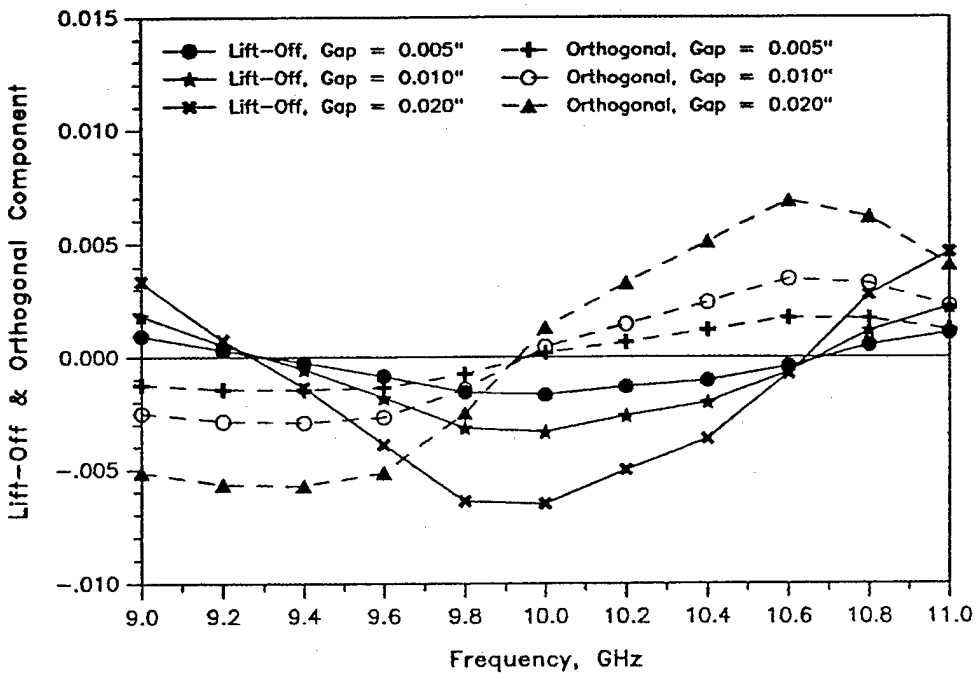

Figure E3. Frequency vs. Lift-Off and Orthogonal Components
Air Gap at 1" from Front Side in Material 2

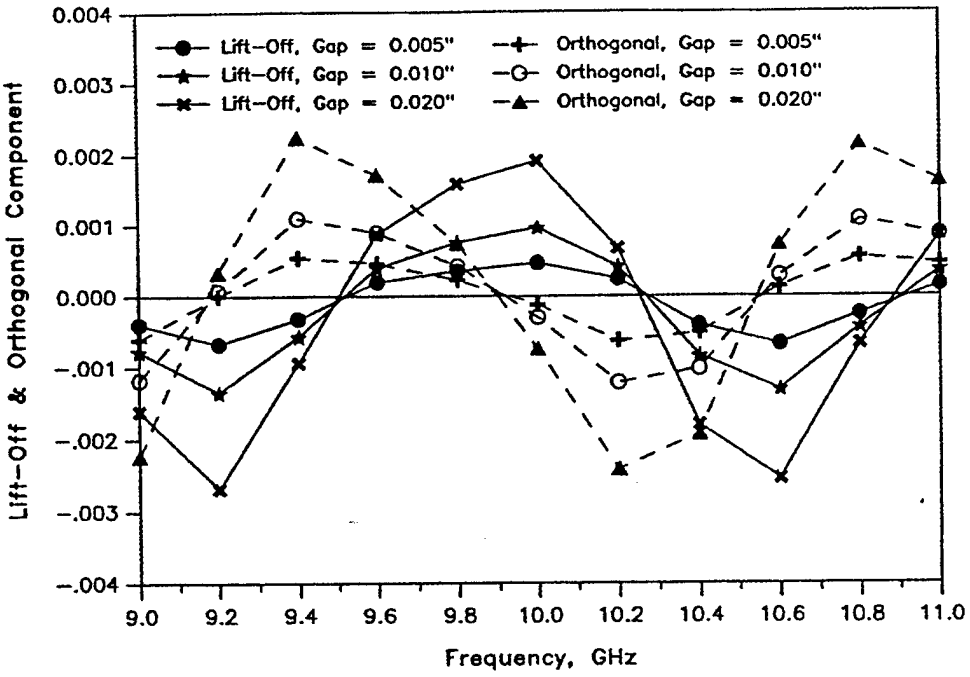

Figure E4. Frequency vs. Lift-Off and Orthogonal Components
Air Gap at 2" from Front Side in Material 2

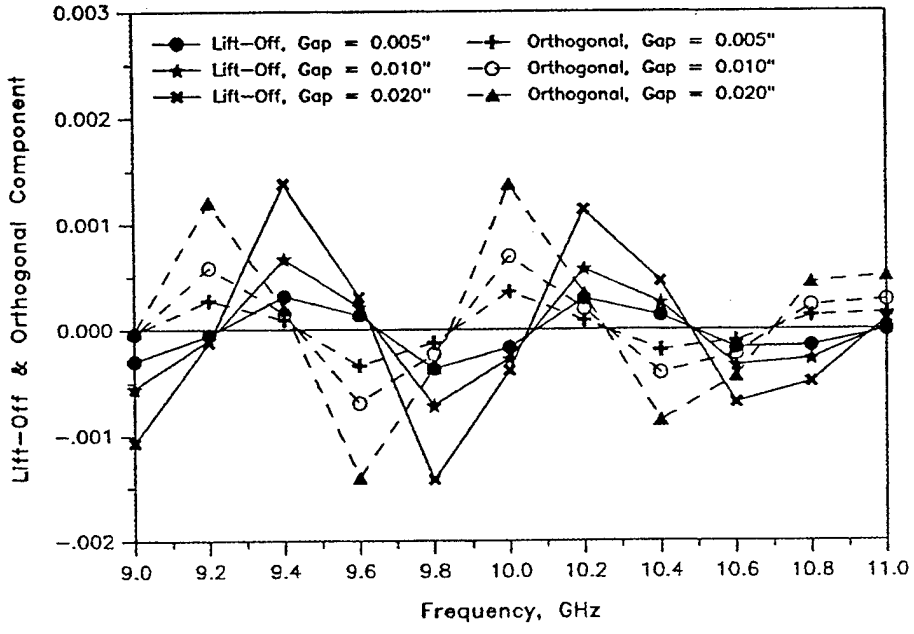

Figure E5. Frequency vs. Lift-Off and Orthogonal Components
Air Gap at 3" from Front Side in Material 2

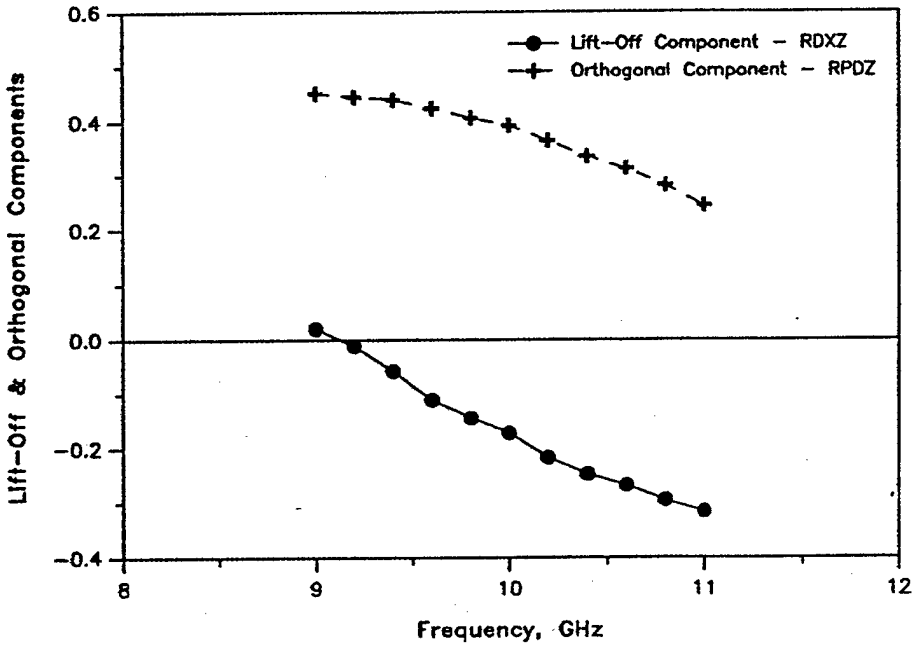

Figure E6. Projection of Reflection Coefficient for Zero Defect on to Lift-Off and Orthogonal Direction

APPENDIX F

COMPARISON OF RESULTS FOR CO-AXIAL LINE WITH THOSE REPORTED IN LITERATURE

Suite 250, 500 Office Center Drive
Fort Washington, PA 19034
Tel: 215-542-8400 Fax: 215-542-8401

INTRODUCTION

This appendix gives some comparison of results obtained using the computer code ADMIT for the co-axial line with the results presented by Bakhtiari, et al., and Li, et al. The results show excellent comparison and the fact that the computer code is free from any bugs and the results can be used with confidence for selecting frequencies and other parameters for interrogating specimens.

Figures F1 - F10 compare the results with those reported by Bakhtiari, et al. (Bakhtiari, S., Ganchev, S. I., and Zoughi, R., "Analysis of Radiation from an Open-Ended Co-Axial Line into Stratified Dielectrics", IEEE Transactions on Microwave Theory and Techniques, Vol. 42, No. 7, July 1994). There are no differences in the results.

Figure F11 compares the results with those reported by Li, et al., (Li, C.L., and Chen, K.M., "Determination of Electromagnetic Properties of Materials Using Flanged Open-Ended Co-Axial Probe - Full Wave Analysis", IEEE Transactions on Instrumentation and Measurement, Vol. 44, No. 1, p. 19, February 1995). The results are found to differ at higher frequencies, either due to the effect of small damping included in the present analysis or the consideration of higher modes considered by Li, et al. Most likely, the later effect plays a more dominant role.

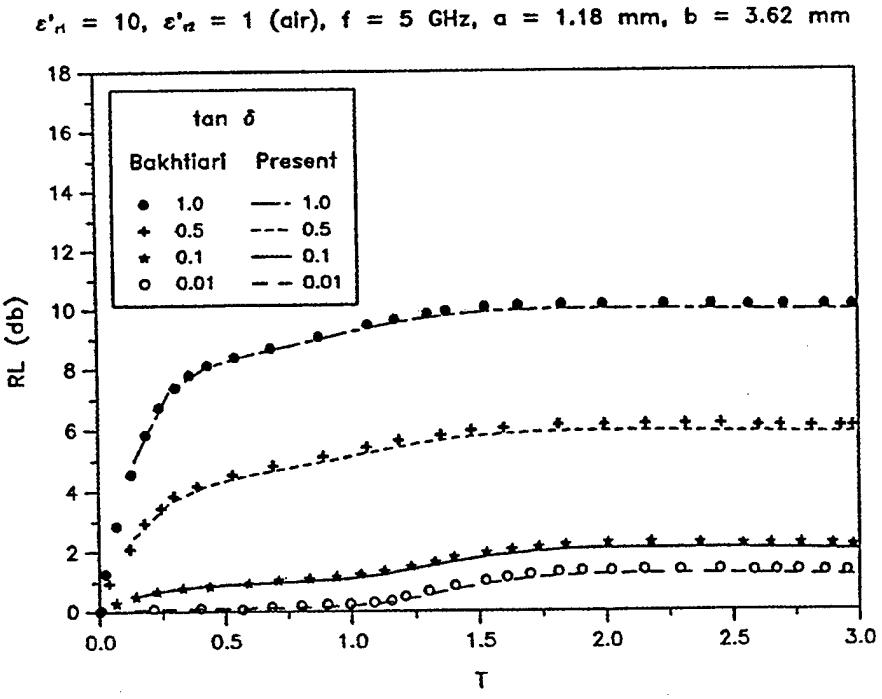

Figure F1. Return Loss Versus Normalized Slab Thickness for a Dielectric Layer Backed by Free-Space

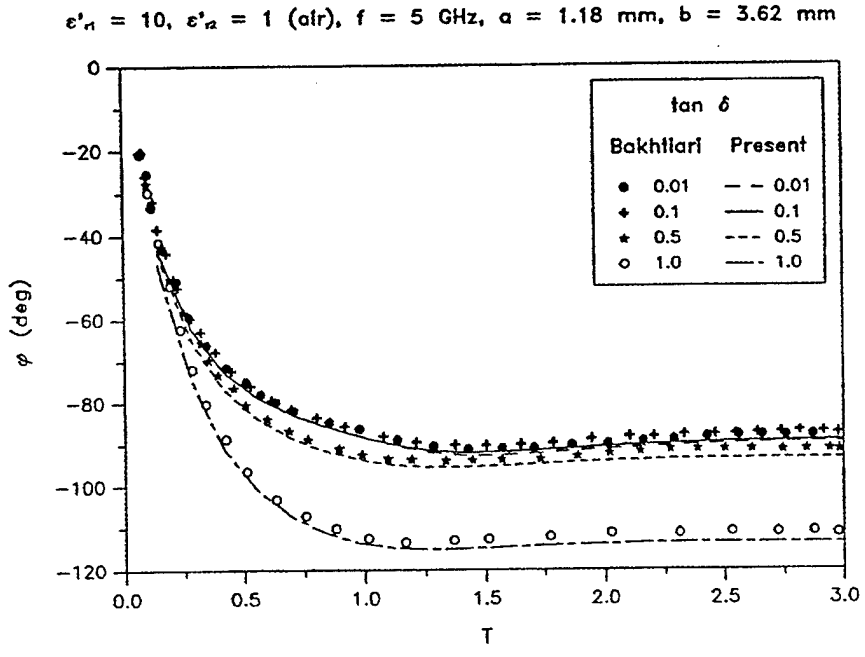

Figure F2. Phase Versus Normalized Slab Thickness for a Dielectric Layer Backed by Free-Space

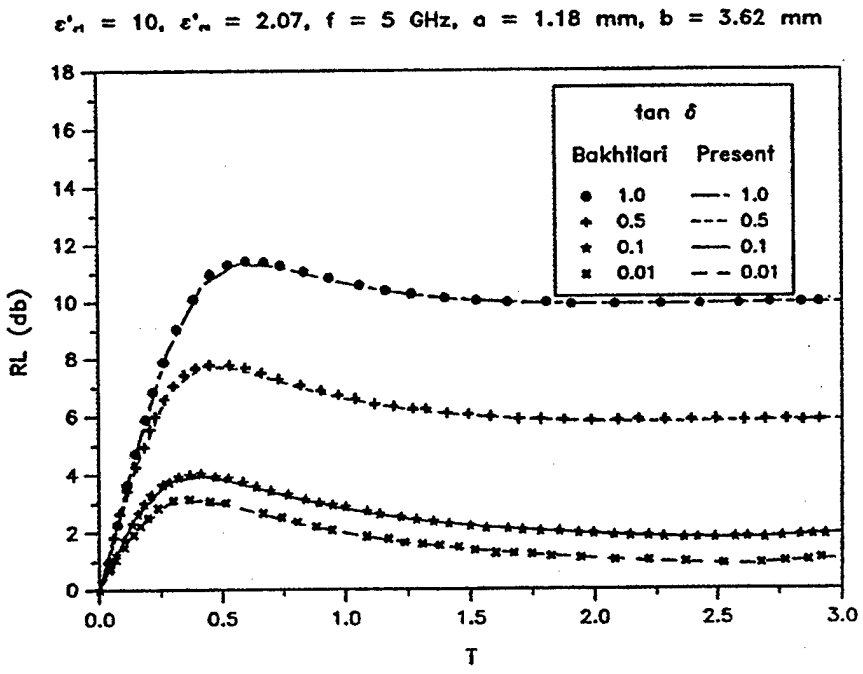

Figure F3. Return Loss Versus Normalized Slab Thickness for a Dielectric Layer Backed by a Conductor

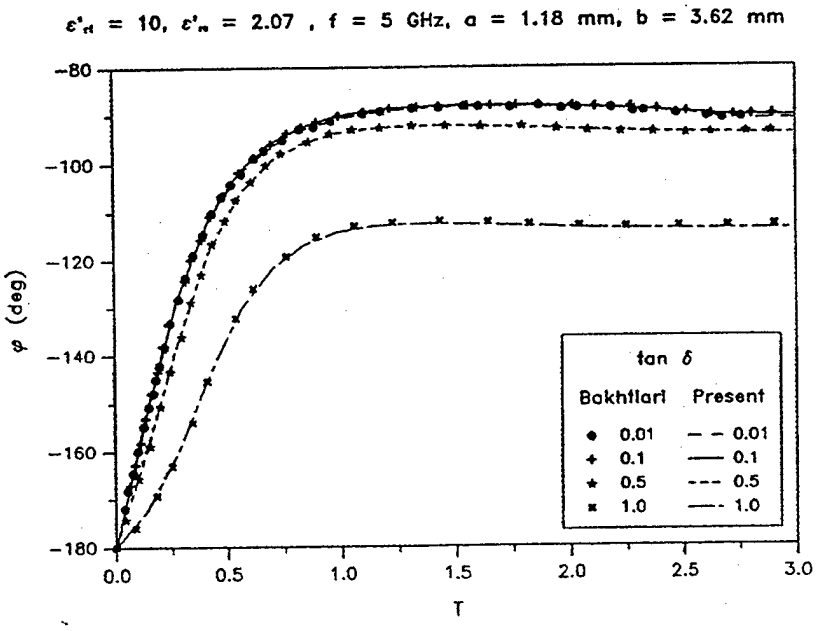

Figure F4. Phase Versus Normalized Slab Thickness for a Dielectric Layer Backed by a Conductor

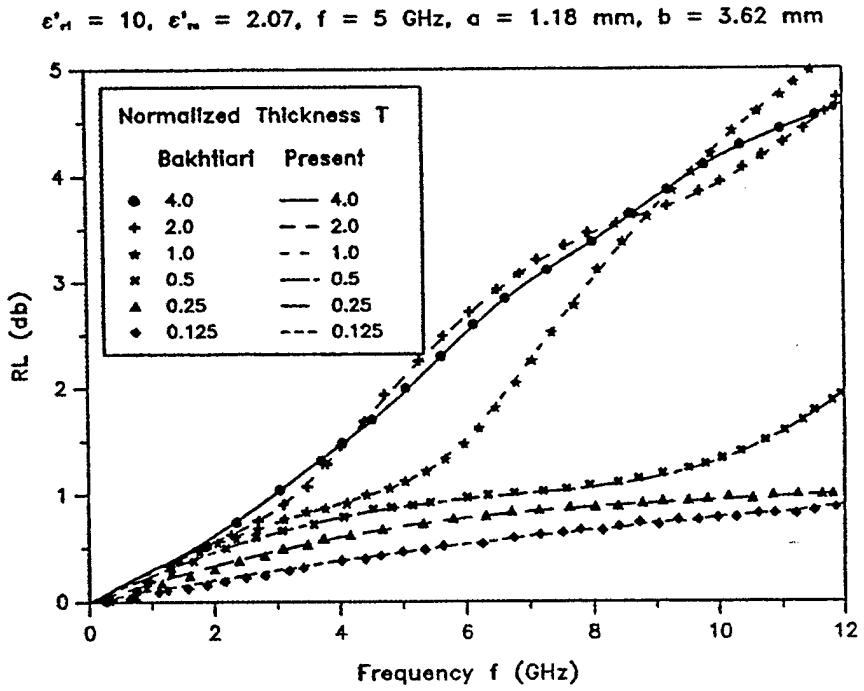

Figure F5. Return Loss Versus Frequency for a Dielectric Layer Backed by Free-Space

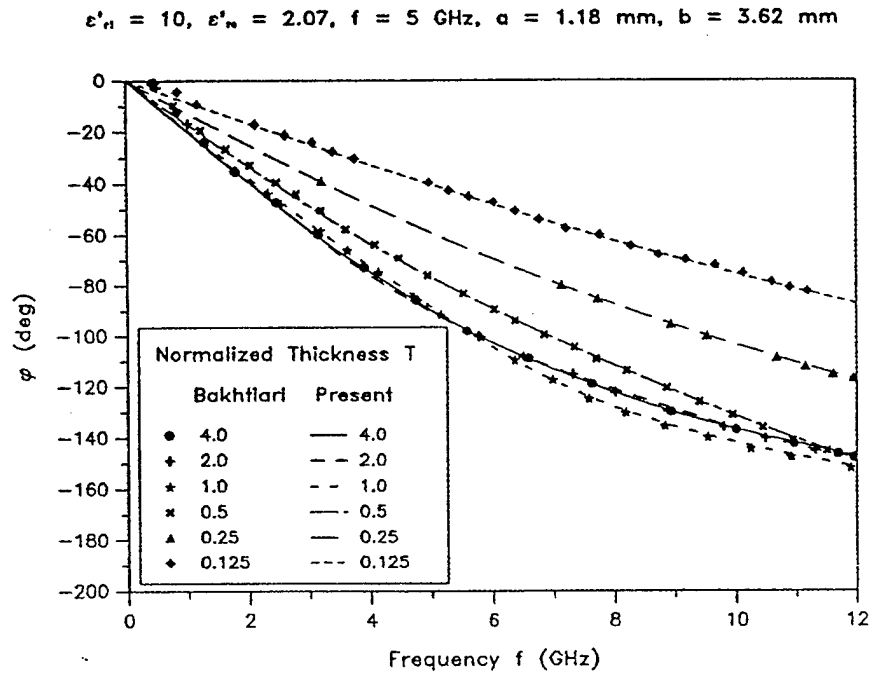

Figure F6. Phase Versus Frequency for a Dielectric Layer Backed by Free-Space

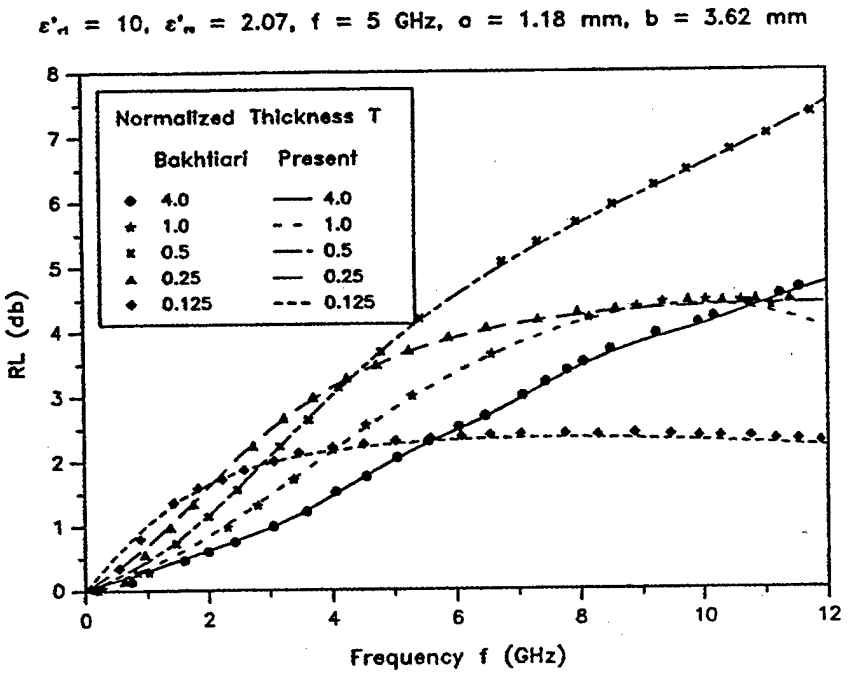

Figure F7. Return Loss Versus Frequency for a Dielectric Layer Backed by a Conductor

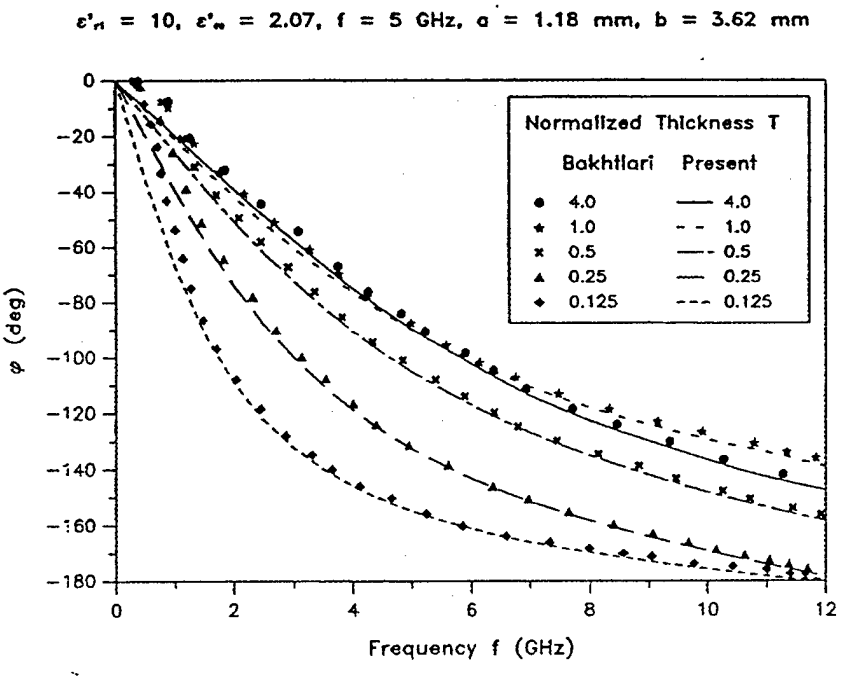

Figure F8. Phase Versus Frequency for a Dielectric Layer Backed by a Conductor

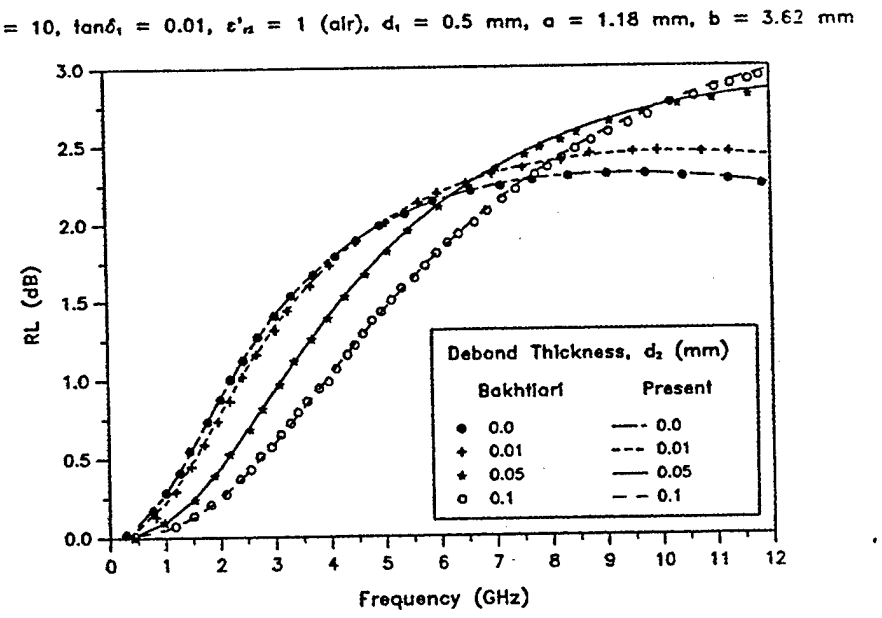

Figure F9. Return Loss Versus Frequency for Various Disbonds in a Two Layer Medium Backed by a Conducting Sheet

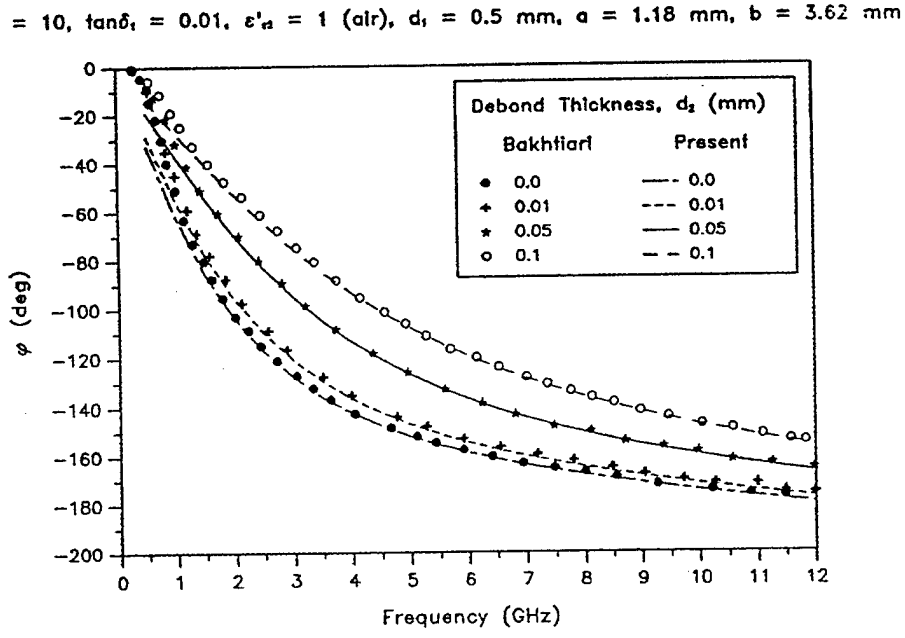

Figure F10. Phase Versus Frequency for Various Disbonds in a Two Layer Medium Backed by a Conducting Sheet

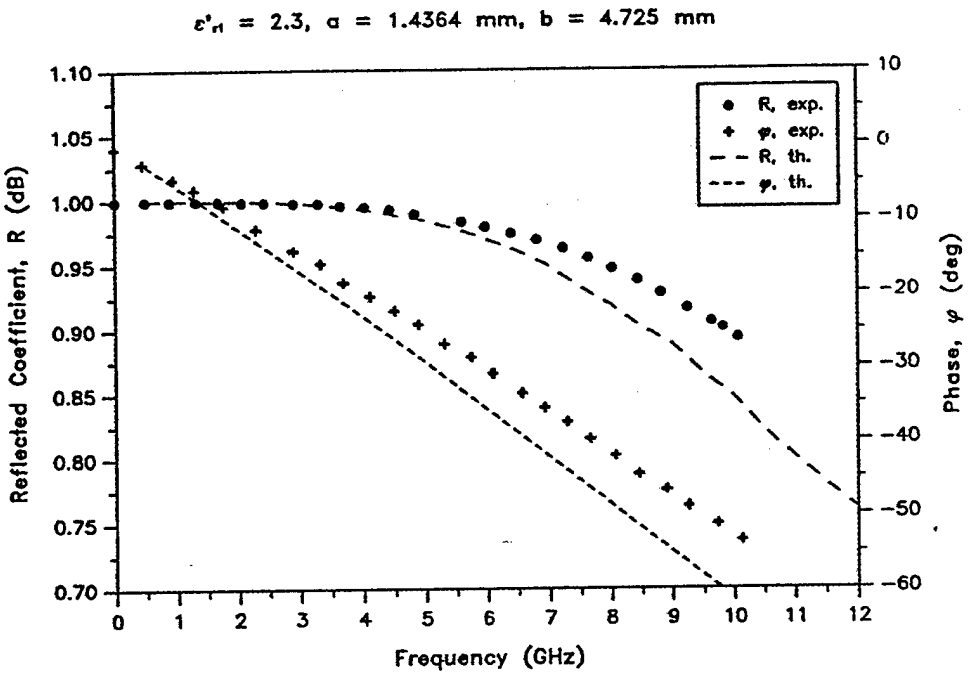

Figure F11. Reflection Coefficient and Phase of a Coaxial Probe Placed Against an Infinite Homogeneous Medium

APPENDIX G

CORRELATION OF EXPERIMENTAL RESULTS AND ANALYSES FOR A CO-AXIAL LINE SENSOR FOR MEASUREMENT OF DIELECTRIC PROPERTIES OF COMPOSITES

Suite 250, 500 Office Center Drive
Fort Washington, PA 19034
Tel: 215-542-8400 Fax: 215-542-8401

INTRODUCTION

In this appendix, results obtained by Liu ("Electrical Characterization of Fiber Reinforced Composites for Mast and Radome Applications, CARDIVNSWC-TR-95/208) were correlated with predictions from the code ADMIT for investigating the effects of the following factors on the measurement of dielectric constants using the co-axial line.

i. Effect of thickness of the dielectric layer
ii. Effect of surface roughness

For low frequencies the admittance Y of the probe can be expressed in terms of two constants C_0 and C_1 which depend on the dimensions of the probe. (See Misra, D., et al., IEEE Transactions on Microwave Theory and Techniques, Vol. 38, No. 1, January 1990.)

$$Y = C_0 + j\omega C_1(\varepsilon' - j\varepsilon'') \quad \text{(G1)}$$

$$\approx \omega C_1(\varepsilon'' + j\varepsilon') \quad \text{(G2)}$$

where ε' is the dielectric constant of the material being interrogated and $\varepsilon'' = \varepsilon' \tan\delta$, $\tan\delta$ being the loss tangent. Equation (G2) is often used in practice, since C_0 is usually small. The computer code was used to calculate the admittance Y for the following probe with Teflon as the core material (ε_c = 2.07) placed against semi-infinite media with varying dielectric constants.

a = inner radius = 0.5959 mm = 0.02323" (G3)

b = outer radius = 1.81 mm = 0.07126" (G4)

Results are given in Tables G1 and G2 for various frequencies and dielectric constant ε' of the medium. Two values of tanδ are considered (tanδ = 0.02 in Table G1 and 0.2 in Table G2). The results show that equation (G2) with C_1 = 2.062 can yield good estimates of the dielectric constant ε' (with 10% accuracy) for both values of tanδ and a wide frequency range. However, use of the same equation will not yield a reliable estimate of ε'', since the linear relationship with ω does not hold for higher values of ω especially when tanδ is small. Therefore, the calibration procedure for evaluation of tanδ is possibly more complicated. However, since the objective of this study is to evaluate the effect of the

thickness of medium and surface roughness on the dielectric constant ε', we use equation (G2) as a basis for comparison.

EFFECT OF LAYER THICKNESS

The loss tangents of the composites studied by Liu are small and the dielectric constant ε' are also not large (of the order of 2.6 to 5.1). The admittances Y were calculated for various layer thicknesses and the following chosen values of ε' and $\tan\delta$.

$$\varepsilon' = 4.7 \tag{G5}$$

$$\tan\delta = 0.02 \tag{G6}$$

The results are given in Table G3 and they show that variations of layer thicknesses considered (Liu used 1 to 3 layer plates, a single layer being 0.125" thick) will not yield any significant error in evaluation of the dielectric constant ε'. Estimates of $\tan\delta$ may, however, be erroneous for high frequencies ($\omega > 7$ GHz).

EFFECTS OF SURFACE ROUGHNESS

To investigate the effects of surface roughness, the admittance was calculated for air gap thicknesses of 0 to 0.0024" between the probe and the dielectric layer of thickness 0.125". The properties of the layer were chosen to be the same as in equations (G5) and (G6). Results are shown in Table G4. The value of Y_1, reduces by about 12.5% (for ω between 1 and 11 GHz) as an air gap of thickness 0.0008" is introduced. The rate of the reduction gradually reduces as the air gap thickness increases and a total reduction of 28% occurs for an air gap of 0.0024". This change is in agreement with that reported by Liu for the material designated as 7781/510A. The difference between the measured values of ε' from polished and unpolished surfaces was found to be about 35%. The unpolished surface (examined by profilometry) show large undulations and smaller roughness features (ripples) with roughness values of the order of 45 and 20 microns. For an assumed sinusoidal variation, a RMS value of 20 microns corresponds to an air gap of 0.0024", the maximum value of the gap studied in Table G4. The effect on the real part of the admittance (and ε'' or $\tan\delta$) is more pronounced.

We also attempted to investigate the effect of an air gap between two layers in addition to an air gap of 0.0024" between the probe and the top layer. Y is affected marginally due to the second air gap.

Table G1. Calculated Values of C_1, for Various ω and ε', $\tan\delta = 0.02$

$$C_1 \approx 10^4 Y_I / (\varepsilon' \omega)$$

ω GHz	$\varepsilon' = 2$	$\varepsilon' = 4.7$	$\varepsilon' = 6.05$	$\varepsilon' = 20$	$\varepsilon' = 40$
1	2.061	2.063	2.063	2.070	2.079
3	2.067	2.078	2.084	2.136	2.205
5	2.083	2.112	2.126	2.253	2.381
7	2.102	2.157	2.182	2.376	2.485
9	2.130	2.212	2.248	2.466	2.423
11	2.161	2.272	2.318	2.484	2.159

$$C_1 \approx 10^4 Y_R / (\varepsilon'' \omega)$$

ω GHz	$\varepsilon' = 2$	$\varepsilon' = 4.7$	$\varepsilon' = 6.05$	$\varepsilon' = 20$	$\varepsilon' = 40$
1	2.064	2.070	2.076	2.124	2.225
3	2.114	2.237	2.312	3.411	5.633
5	2.285	2.802	3.117	7.695	16.378
7	2.634	3.971	4.784	16.003	35.000
9	3.225	5.921	7.540	28.361	58.220
11	4.109	8.781	11.525	43.770	80.420

Table G2. Calculated Values of C_1 for Various ω and ε', $\tan\delta = 0.2$

$$C_1 \approx 10^4 Y_I / (\varepsilon' \omega)$$

ω GHz	$\varepsilon' = 2$	$\varepsilon' = 4.7$	$\varepsilon' = 6.05$	$\varepsilon' = 20$	$\varepsilon' = 40$
1	2.061	2.062	2.063	2.069	2.077
3	2.067	2.077	2.081	2.123	2.172
5	2.081	2.104	2.116	2.202	2.260
7	2.097	2.138	2.156	2.257	2.236
9	2.118	2.176	2.198	2.260	2.052
11	2.142	2.212	2.235	2.185	1.719

$$C_1 \approx 10^4 Y_R / (\varepsilon'' \omega)$$

ω GHz	$\varepsilon' = 2$	$\varepsilon' = 4.7$	$\varepsilon' = 6.05$	$\varepsilon' = 20$	$\varepsilon' = 40$
1	2.062	2.065	2.067	2.083	2.108
3	2.079	2.111	2.127	2.324	2.647
5	2.123	2.223	2.278	2.916	3.908
7	2.191	2.410	2.529	3.861	5.704
9	2.294	2.686	2.895	5.100	7.593
11	2.432	3.049	3.373	6.456	9.090

Table G3. Calculated Values of C_1 for Varying Layer Thickness h

ε' , =4.7, tanδ = 0.02

$C_1 \approx 10^4 Y_I / (\varepsilon' \omega)$

ω GHz	h = 0.0625"	h = 0.125"	h = 0.25"	h=∞
1	1.980	2.048	2.099	2.063
3	1.988	2.060	2.075	2.078
5	2.009	2.090	2.114	2.112
7	2.038	2.137	2.165	2.157
9	2.082	2.213	2.217	2.212
11	2.139	2.309	2.267	2.272

$C_1 \approx 10^4 Y_R / (\varepsilon'' \omega)$

ω GHz	h = 0.0625"	h = 0.125"	h = 0.25"	h=∞
1	1.948	2.044	2.062	2.070
3	1.979	2.072	2.105	2.237
5	2.022	2.159	2.470	2.802
7	2.206	2.465	3.951	3.971
9	2.281	2.565	6.300	5.921
11	2.760	6.656	9.204	8.781

Table G4. Calculated Admittances ($Y_R + j\,Y_I$,) for Varying Air Gap, g and 0.125 " Thick Layer, $\varepsilon' = 4.7$, $\tan\delta = 0.02$

$$Y_I, (ohm)^{-1}$$

ω GHz	g=0	g = 0.0008	g = 0.0016	g=0.0024
1	0.962×10^{-3}	0.842×10^{-3}	0.754×10^{-3}	0.687×10^{-3}
3	0.291×10^{-2}	0.254×10^{-2}	0.228×10^{-2}	0.207×10^{-2}
5	0.491×10^{-2}	0.430×10^{-2}	0.385×10^{-2}	0.350×10^{-2}
7	0.703×10^{-2}	0.615×10^{-2}	0.552×10^{-2}	0.502×10^{-2}
9	0.936×10^{-2}	0.819×10^{-2}	0.734×10^{-2}	0.668×10^{-2}
11	0.119×10^{-1}	0.104×10^{-1}	0.935×10^{-2}	0.849×10^{-2}

$$Y_R, (ohm)^{-1}$$

ω GHz	g = 0	g = 0.0008"	g = 0.0016"	g = 0.0024"
1	0.192×10^{-4}	0.146×10^{-4}	0.116×10^{-4}	0.952×10^{-5}
3	0.584×10^{-4}	0.444×10^{-4}	0.354×10^{-4}	0.291×10^{-4}
5	0.102×10^{-3}	0.774×10^{-4}	0.621×10^{-4}	0.513×10^{-4}
7	0.162×10^{-3}	0.127×10^{-3}	0.105×10^{-3}	0.889×10^{-4}
9	0.302×10^{-3}	0.251×10^{-3}	0.217×10^{-3}	0.193×10^{-3}
11	0.688×10^{-3}	0.600×10^{-3}	0.536×10^{-3}	0.487×10^{-3}